Experimental Investigation of Carbon Black Properties Produced by the Thermal Decomposition of Methane in the Products of Premixed Flames

by

Mohammad Javad Afroughi

A thesis submitted in partial fulfillment of the requirements for the degree of

Master of Science

Department of Mechanical Engineering
University of Alberta

Abstract

The thermal decomposition of methane is a technique used to manufacture hydrogen gas and carbon black. The physical properties of carbon black produced by the thermal decomposition of methane (TDM) in the O_2-deficient gas products of two premixed flames (propane- or methane-air) were investigated under different flow rates of decomposing methane injection (0.5–5 SLPM). An inverted burner was designed to provide a fuel-rich, laminar premixed flame, to produce hot gas into which methane was injected to thermally decompose inside a reactor. Particles from TDM were extracted by a nitrogen dilution-sampling system at the immediate exit of the reaction chamber, where another branch of the exhaust was dried and directed to a gas chromatograph. The carbon black particles were characterized by size resolved number concentration, mass concentration, effective density, volatility, and internal mixing state using different arrangements of a differential mobility analyzer, catalytic denuder, centrifugal particle mass analyzer, and condensation particle counter, as well as by morphology and primary particle size using transmission electron microscopy. A bimodal number-size distribution was observed at all conditions with count median diameters (CMDs) less than 58 nm and 21 nm when using propane- or methane-air premixed flame as the heat source, respectively. Higher number concentrations and mass concentrations with larger CMDs were achieved under lower flow rates of decomposing methane injection. For a given flow rate of decomposition methane, mass concentration and CMD increased significantly when using propane as the fuel, compared to the methane fuel. The size segregated mass fraction of internally mixed volatile content in particles was similar for both heat sources, showing a roughly constant fraction of volatile materials in particles produced by the decomposition of 0.5 and 5 SLPM of methane (10%–30%) but a measurably larger fraction (55%–30%) with a decreasing trend as a function of particle size from the decomposition of 1 SLPM of methane. The effective density of denuded particles was

similar, but slightly higher, than the effective density of soot from a wide range of internal combustion engines. A higher denuded effective density was observed in the particles with higher volatile contents (particles from decomposition of 1 SLPM of methane), suggesting the restructuring of carbon black into more compact clusters due to the excessive volatile condensation. TEM analysis revealed some similarity between the produced carbon black and engine soot in terms of morphology and primary particle diameter (both below 40 nm). Beside the carbon black properties, the efficiency of TDM in this configuration was also investigated by evaluation of methane destruction efficiency, as well as carbon black and hydrogen production efficiencies, based on the product gas composition and the particle mass concentration. It was found that TDM with a lower flow rate of injection is more favorable for methane to thermally decompose and to convert to H_2 and carbon black, with maximum efficiencies of ~95%, ~80%, and ~1%, respectively. It was concluded that the significantly low efficiency of carbon black production is due to the high amount of CO formation, likely through the gasification process.

Preface

The research project, of which this thesis is a part, was led by Dr. Jason Olfert and Dr. Larry Kostiuk. Farjad Falahati assisted in developing the setup and gas chromatograph operation.

Parts of Chapter 2 and Chapter 3 of this thesis have been published as:

M. J. Afroughi, F. Falahati, L. W. Kostiuk, J. S. Olfert; Properties of carbon particles generated by methane decarbonization in oxygen deficient gas streams; *10th International Aerosol Conference (IAC)*, St. Louis, Missouri, USA, Sep 2-7, 2018.

M. J. Afroughi, F. Falahati, L. W. Kostiuk, J. S. Olfert; Nanoparticle emission characteristics during methane pyrolysis in a laminar premixed flame; *20th International Conference on Aerosol Science and Technology*, Lisbon, Portugal, April 16-17, 2018.

F. Falahati, M. J. Afroughi, J. S. Olfert, and L. W. Kostiuk; Preliminary experimental study of methane decarbonization using a laminar premixed flame; *Proceedings of Combustion Institute – Canadian Section, Spring Technical Meeting*, Montreal, Canada, May 15-18, 2017.

A similar version of this thesis was submitted to the *Journal of Aerosol Science* as:

M. J. Afroughi, F. Falahati, L. W. Kostiuk, J. S. Olfert; Properties of carbon black produced by the thermal decomposition of methane in the products of premixed flames.

I was responsible for conducting the experiments, designing the sampling system, data collection and analysis, as well as manuscript composition.

“The garden of the world has no limits, except in your mind.”

— Rumi

To d

Acknowledgements

I would like to express the deepest appreciation to my supervisors, Dr. Jason Olfert and Dr. Larry Kostiuk, whose wisdom, guidance and continuous support nurtured my knowledge and helped me throughout the research. Challenges in this piece of work could not be overcome without their patience, motivation, and technical advice.

Special thanks to my family and friends who encouraged and supported me during my graduate program.

Table of Contents

List of Tables

List of Figures

Chapter 1

Introduction

1.1 Fossil Fuels and Global Warming

A dramatic increase in greenhouse gas emissions has happened on a global scale due to recent human activities which led to a higher atmospheric temperature (Abbas & Wan Daud 2010). The main reason of these emissions is the dependency of energy to fossil fuels; the energy market is driven by fossil fuel as it holds 87% of the market share, while renewable energy's share is only 2% (Ashik et al. 2015). CO_2 accounts for 85%–95% of the total greenhouse gas emissions which are mainly produced by motor vehicles (Leduc et al. 2008). With the current rate of CO_2 emissions and since fossil fuels might be the main source of energy for the next 50 years (A Abánades et al. 2011), the atmospheric concentration of CO_2 has the potential to become twice by then, which might cause serious climate effects (A Abánades et al. 2011).

1.2 Hydrogen Economy

Hydrogen is the lightest and the most available element in the universe and can be a promising source of energy (Ashik et al. 2015). A mass basis analysis shows that the energy released by hydrogen combustion is more than twice the energy from combustion of some common fuels such as methane, ethane, propane, butane, kerosene, and diesel (Ashik et al. 2017). The main product of hydrogen combustion is water (Ashik et al. 2015). Due to its unique characteristics, hydrogen could become a substantial source of energy in near future (Ashik et al. 2017), however the present production of hydrogen is not enough to meet the global energy

demand — hydrogen production should reach approximately 3×10^{12} kg of hydrogen per year to replace fossil fuels as the main source of energy (Ashik et al. 2015).

Hydrogen is not available in nature and it should be produced from other sources such as coal, natural gas, biomass, methanol, and water (Valle et al. 2009). There are different methods available to produce hydrogen among which are steam methane reforming (SMR), coal gasification, biomass gasification, thermal decomposition of methane (TDM) (Abbas & Wan Daud 2010), and electrochemical/photochemical processes (Momirlan & Veziroglu 2002).

1.3 Thermal Decomposition of Methane (TDM)

Global statistics indicate that currently natural gas is the main source of hydrogen production with the share of 48% of the annual hydrogen production, while other sources such as petroleum, coal and water stand for 30%, 18% and 4% (Balat & Balat 2009). Abundance of natural gas resources made it the favorable source of hydrogen extraction (Konieczny et al. 2008); furthermore, methane (main content of natural gas) has the highest hydrogen-to-carbon ratio among all hydrocarbons which makes it a suitable candidate for hydrogen production (Ashik et al. 2017). Steam reforming method as one of the common ways of hydrogen production releases about 13.7 kg of CO_2 per kg of produced hydrogen (Rodat, Stéphane Abanades, et al. 2009). TDM can be used for hydrogen production with no CO_2 emissions, where natural gas decomposes into hydrogen and carbon black in the absence of oxygen and at high temperatures (Abbas & Wan Daud 2010). Furthermore, produced carbon black in TDM is easier to capture and store comparing to CO_2 in SMR (Abbas & Wan Daud 2010). CO_2 capture and storage in SMR will cause up to 40% energy lost in the entire process (Steinberg 1999).

TDM is considered to be the most economical method for hydrogen production (Ashik et al. 2015). This method is a single step mechanism with reduced GHG emissions (Ashik et al. 2017). Moreover, produced carbon black in TDM is a valuable industrial material with various applications. About 70% of carbon black is used in tire industry, rubber products stand for 20% and the rest is in non-rubber products (WHO 1984). Annual world carbon black production is roughly 9 Mt (Adams 2007). By decomposing half of the available natural gas in the US to hydrogen and carbon black, 40 Mt of carbon would be produced (Muradov & Veziroä 2005); however, currently furnace process is in charge of 90% of carbon production (Gautier et al. 2016), which is based on an incomplete combustion of a hydrocarbon where CO_2 is produced in the process (Fulcheri & Schwob 1995). Figure 1.1. shows the furnace process.

TDM is still in laboratory levels, and much more studies are needed for topics such as conversion rate of methane and characteristics of carbon black. Many experimental and numerical studies have investigated the conversion rate of methane into hydrogen while focusing on residence time and temperature. Abánades, Ruiz, & Ferruelo (2011) reached 10% hydrogen for residence time of 16 s and 40% yield for 96 s at a temperature of 1000 °C in their heated furnace. Paxman, Trottier, Flynn, Kostiuk, & Secanell (2017) used a perfectly mixed reactor where at 1100 °C methane conversion reached to 60%. Rodat, Abanades, Sans, & Flamant (2009) observed conversion rate of 98% and hydrogen yield of 90% at 1497 °C with their graphite tubular reactors. Using various tube materials such as quartz, graphite and silicon carbide had the same methane conversion rate (A Abánades et al. 2011). At temperatures over 1350 °C full conversion of methane would occur and residence time effects would become negligible (A Abánades et al. 2011).

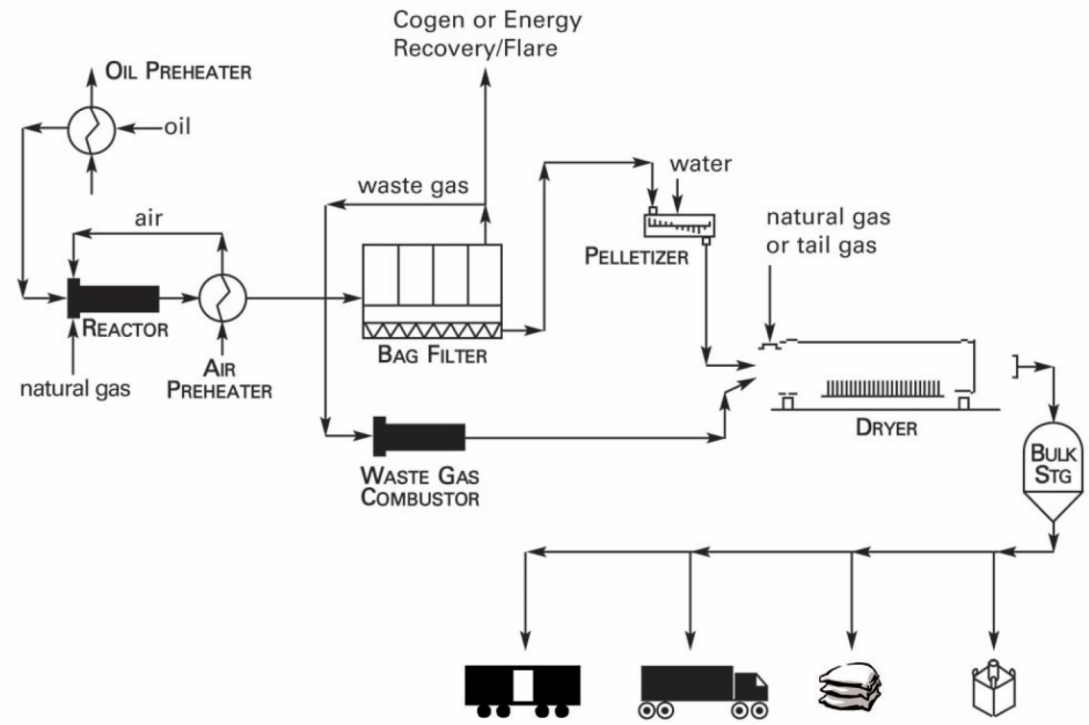

Figure 1.1. Typical furnace black production process.
(Picture is taken from International Carbon Black Association (2016).)

1.4 Carbon Black

TDM is the process where heat is added to methane to chemically decompose the gas at high temperatures into hydrogen gas (H_2) and solid elemental carbon. When TDM is used industrially to produce elemental carbon, the carbon is called carbon black. Carbon black consists of fractal-like aggregates made up of primary particles and typically contains more than 97% elemental carbon with minimal quantities of oxygen, hydrogen and nitrogen (Long et al. 2013). Carbon black is widely used as reinforcement and performance additive in rubber products (approximately 90% of carbon black production), and sometimes used as pigment, UV

absorbing, and/or conducting agents in the coating, plastics, polymers, and printing industries (International Carbon Black Association 2006).

The commercial process of TDM is cyclic; using natural gas, consisting predominantly of methane, as the feedstock in a tandem arrangement of two furnaces that alternate every 5 min between preheating and carbon black production, also known as the heat cycle and make cycle. In the make cycle, natural gas is injected into the hot refractory-lined furnace (at about 1300 ℃) and undergoes thermal decomposition. The product stream is later cooled with water sprays in a quench tower and sent to a bag house where carbon black is filtered. The off-gas, which is ~90% hydrogen, is subsequently dehumidified in a water scrubber and burned in a near stoichiometric mixture with air in the heat cycle (Wang et al. 2011). The carbon black made in this process is often referred as thermal black, and is regularly used in rubber and plastic products. Thermal black is among the most expensive types of carbon black, and is characterized by having the largest primary particles (120–500 nm) with a low degree of aggregation (aggregate diameters of 400–600 nm), and the smallest surface area (6–15 $m^2 g^{-1}$) (Black et al. 2010). The thermal black process is shown in Figure 1.2.

Other than the thermal black process, there are several well-established manufacturing processes of carbon black production using either partial combustion of oil and coal tar (furnace black, Degussa gas black, and lamp black), or thermal decomposition of acetylene (acetylene black process). Depending on the manufacturing process and the reaction conditions within the process, different grades of carbon black can be achieved. The properties of each grade is characterized by its chemical composition (*e.g.*, volatile content, ash content, and pH), micro-structure (*e.g.*, degree of graphitization), morphology (primary particle size, aggregate size,

aggregate structure, and surface area), and surface activity (*e.g.*, surface energy) (Wang et al. 2011).

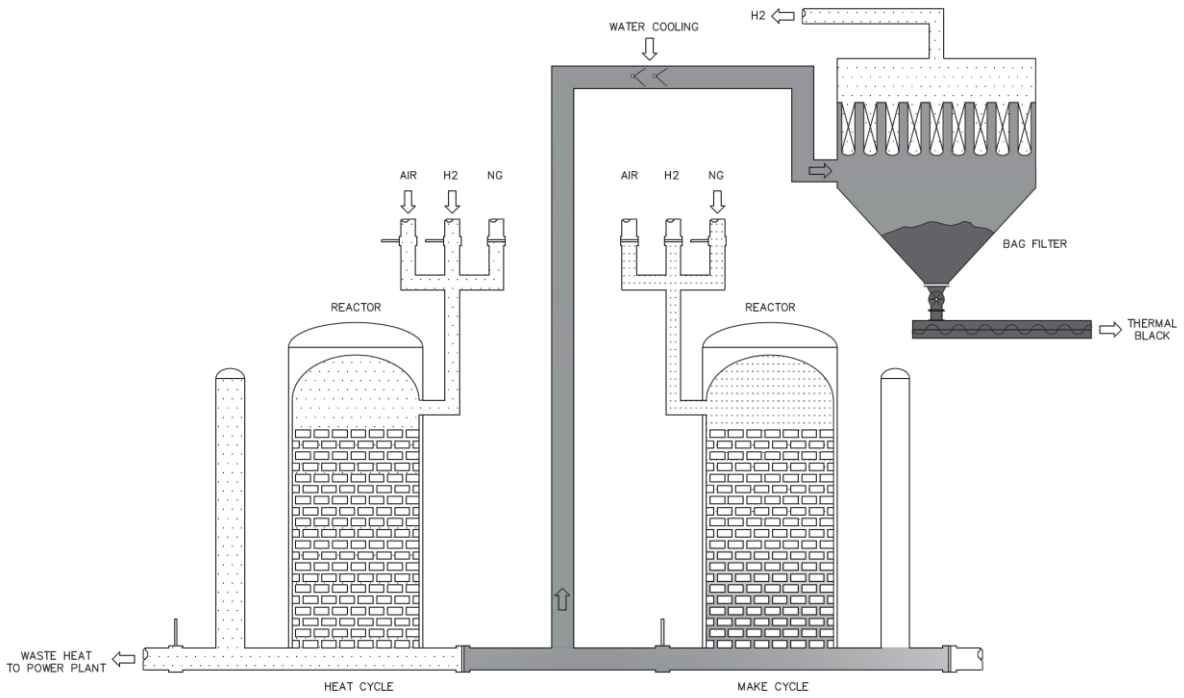

Figure 1.2. Typical thermal black production process.
(Picture is taken from International Carbon Black Association (2016).)

TDM is also viewed as a cost-effective green technology to produce H_2 without CO_2 emissions (Weger et al. 2017). The commercial process for this purpose is still a challenge but many laboratory-scale studies have investigated H_2 production over a wide range of metal catalyzed reactions, carbon catalyzed reactions, and non-catalytic TDM. TDM on metal catalysts is more favorable in temperatures below 800 ℃ and tend to produce filamentous carbon, while carbon catalyzed and non-catalytic TDM mainly produce graphite-like carbon or carbon black in suitable reaction temperatures of 800–1100 ℃, and above 1100 ℃, respectively (Keipi et al. 2016). Accordingly, based on the reaction conditions (temperature and pressure), kinetic

parameters, and residence time required by the catalytic or direct thermal decomposition of methane, a variety of reactor configurations (fixed bed reactor, rotary bed reactor, multilayer reactor, continuous flow reactor, fluidized bed reactor, molten-metal reactor) with different heat sources (electrical furnace, microwave, concentrated solar energy, plasma) has been designed and tested (Ashik et al. 2017; Ashik et al. 2015; Abbas & Wan Daud 2010; Keipi et al. 2016; D. Paxman et al. 2017; Ahmed et al. 2009; Parkinson et al. 2018).

1.5 Thesis Objectives

This piece of work studies carbon black production by direct thermal cracking of methane in O_2-deficient gas products of premixed flames in a continuous flow reaction chamber. Providing the heat needed for TDM by a flame would be less expensive and thereby increasing the probability it could be commercialized. The direct mixing of methane with the off-gas of flames gives further advantages in the TDM process, such as better mixing, rapid and higher heat transfer, and eliminates the pressure drop caused by the carbon accumulation. Furthermore, the produced carbon black in this process can be separated from the product mix and collected in a cyclone, while the remaining gas can be burned as an additional heat source or stored for other uses if dehumidified. The drawback of this method is that carbon black and H_2 are mixed with the gas stream of combustion products containing water vapor and CO_2, which makes it possible for the reaction to shift toward gasification and produce CO. As such, carbon black production efficiency would decrease, however, a mixture of CO, H_2, and CO_2 (known collectively as syngas) seems to be a suitable feed for the Fischer-Tropsch process in downstream petrochemical units, or for electricity generation.

In this context, the present work is focused on the following objectives through different reaction conditions of TDM in the products of premixed flames:

I. the physical properties of the produced carbon black including aggregate size distribution, density and mass of aggregates, aggregate volatile content and structure, and the size of primary particles;
II. the conversion efficiency of the process in terms of methane destruction efficiency, and carbon black and H_2 yields.

1.6 Thesis Outline

Chapter 2, Materials and Methods, highlights the Experimental Setup designed for this project along with the Theory and Data Analysis of test results including Methane Destruction Efficiency, Hydrogen Production Efficiency, Carbon Black Number-size Distribution, Carbon Black Effective Density, Carbon Black Mass-size Distribution, Carbon Black Volatile Mass Fraction, Carbon Black Production Efficiency, and Carbon Black TEM Image Analysis.

Chapter 3, Results and Discussion, explains the outcomes of this project in terms of Reaction Conditions, Methane Destruction Efficiency, Hydrogen and Carbon Black Production, and Carbon Black Characteristics, which include Number-size Distribution, Mass-size Distribution, Volatility and Internal Mixing State, Denuded Effective Density and Mass-mobility Exponent, and Morphology and Primary Particle Diameter, as well as carbon black production to energy consumption ratio.

Chapter 4, Conclusions and Future Work, highlights a summary of the project and conclusions, as well as recommendations for future works.

Appendix A, Uncertainty Analysis, describes the error calculations with respect to test results and data analysis.

Appendix B, TEM Images, shows all the carbon black images taken by transmission electron microscopy.

Appendix C, Temperature Correction, describes the analysis for correcting the thermocouple temperature measurements.

Chapter 2

Materials and Methods

2.1 Experimental Setup

A schematic of the experimental setup is shown in Figure 2.1. In this work, the gaseous emission concentration and physical properties of carbon black were measured following thermal decomposition of methane in hot products of two different premixed flames. An inverted burner was designed to provide a rich, laminar, premixed flame of propane- or methane-air, with a total constant flow rate of 36.5 SLPM and equivalence ratio of 1.05. The premixed inverted burner has an inner diameter of 26.9 mm and a concentric tube (6.4 mm in diameter) is located centrally in the burner to inject a co-flow of methane which will thermally decompose in the products of the premixed flame. The exit of the burner enters a reaction chamber, 40 mm in diameter and 680 mm in length, which is insulated with ceramic blocks enclosed within a sealed quartz tube (200 mm in diameter). A detailed description of the burner and the reaction chamber are presented elsewhere (Falahati 2018). The temperature of the products of the premixed flames was measured by a K-type exposed-junction thermocouple in the axial direction in the reaction chamber.

In order to quantify the composition of the products, two sampling branches were taken from the exhaust. To measure gaseous concentrations (CH_4, C_2H_6, C_3H_8, CO_2, CO, O_2, N_2, and H_2), a branch of products was dried by a custom-built condensation heat exchanger and sent to a gas chromatograph (GC; Agilent 7890B), while the other branch sampled particles with a nitrogen dilution system. The dilution system was placed at the immediate exit of the chamber to reduce particle losses. Particle samples were extracted through a 1.6 mm ID tube which was

connected to the throat of an aluminum venturi with inlet and throat diameters of 10 and 5 mm, respectively. By flowing constant rates of particle-free dry nitrogen into the inlet of the venturi tube, samples were extracted and diluted with nitrogen with dilution factors on the order of 155 to 200.

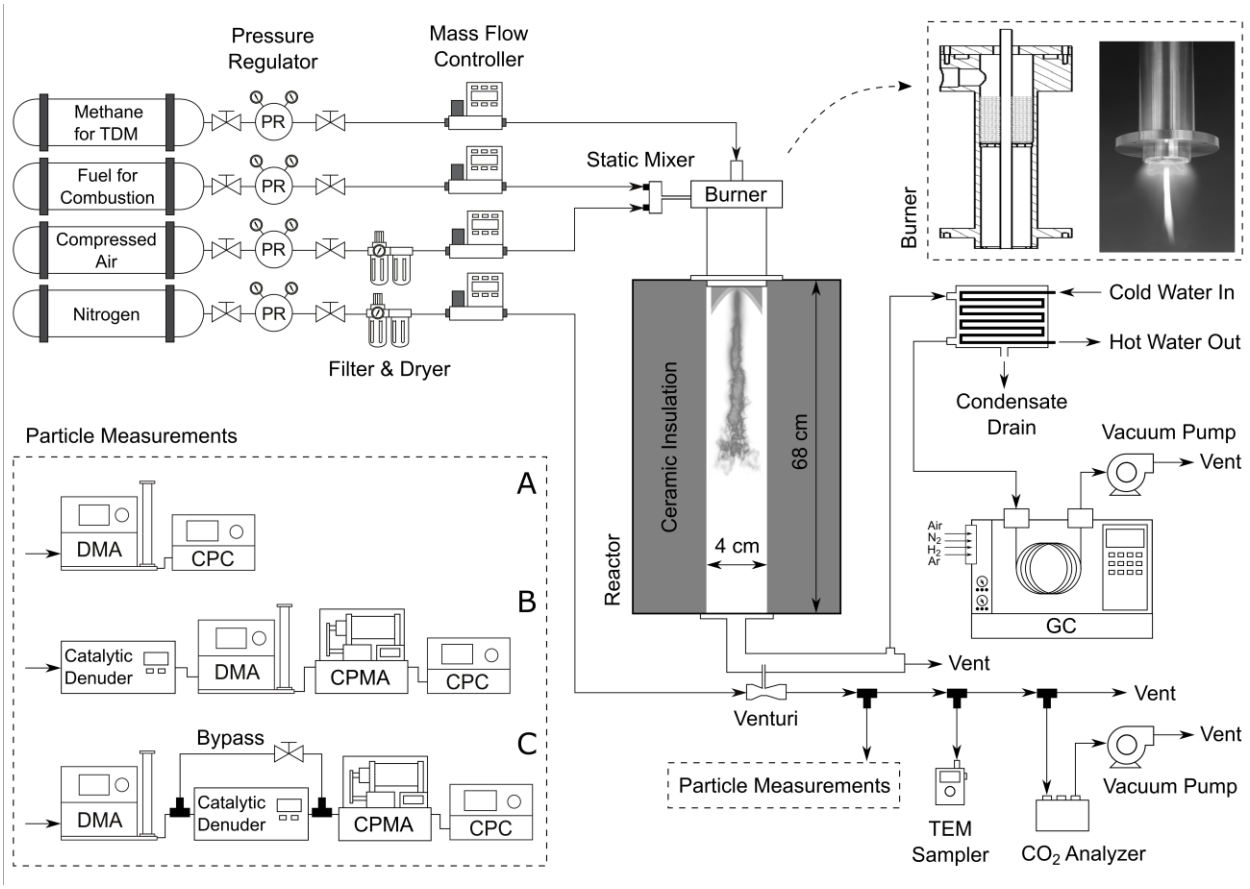

Figure 2.1. Experimental setup.

The diluted sample was later split into three branches for: i) particle size and mass measurement, ii) transmission electron microscopy (TEM) grid collection, and iii) CO_2 concentration measurement. Number-size distribution, effective density and volatile mass fraction of particles were obtained with particle measurements utilizing different arrangements of

a differential mobility analyzer (DMA; TSI Inc., Model 3081), catalytic denuder (Catalytic Instruments, Model CS015), centrifugal particle mass analyzer (CPMA; Cambustion), and condensation particle counter (CPC; TSI Inc., Model 3776). To further investigate carbon black morphology, an electrostatic precipitator (ESPnano, Model 100) was used to collect carbon black particles on TEM grids from the second branch of diluted samples. For each experimental condition, sampling time was adjusted based on the recommendations from the manual to ensure enough particles were sampled on the grid without it being saturated. The TEM grids were ultrathin carbon film (less than 3 nm thick) lying across a carbon lacey film supported by a 400 mesh copper grid (Ted Pella Inc., Product No. 01824). The last branch of diluted samples was used for CO_2 concentration measurements using a non-dispersive infrared CO_2 analyzer (LI-COR, Model LI-840A). The CO_2 concentration in diluted samples was used to calculate the dilution ratio.

2.2 Theory and Data Analysis

2.2.1 Methane Destruction Efficiency

Methane destruction efficiency indicates how effective the injected methane was decomposed in hot products of the premixed flame. Regardless of the type of fuel, methane destruction efficiency is defined as

$$\eta_{\mathrm{CH_4,\,des}} = 1 - \frac{\dot{m}_{\mathrm{CH_4,out}}}{\dot{m}_{\mathrm{CH_4,in}}}, \tag{2.1}$$

where $\dot{m}_{\mathrm{CH_4,in}}$ and $\dot{m}_{\mathrm{CH_4,out}}$ are the mass flow rates of injected methane (excluding methane for the premixed-burner if that fuel was being used) and of undecomposed methane in the exhaust, respectively. $\dot{m}_{\mathrm{CH_4,in}}$ was calculated by

$$\dot{m}_{\mathrm{CH_4,in}} = \dot{V}_{\mathrm{CH_4,in}}\,\rho_{\mathrm{CH_4}}, \tag{2.2}$$

where $\dot{V}_{\mathrm{CH_4,in}}$ is the standard flow rate of injected methane set by a mass flow controller and $\rho_{\mathrm{CH_4}}$ is the density of methane in the standard conditions (0 ℃ and 1 atm). To obtain $\dot{m}_{\mathrm{CH_4,out}}$, or mass flow rate of any other component in the exhaust, the following calculations and assumptions were made.

The combustion of the fuel with air and the addition of decomposition methane is assumed to result in the following reaction:

$$n_1\mathrm{C_xH_y(fuel)} + n_2(\mathrm{O_2} + 3.76\mathrm{N_2}) + n_3\mathrm{CH_4} \rightarrow n_4\mathrm{CO_2} + n_5\mathrm{CO} + n_6\mathrm{H_2O} + n_7\mathrm{N_2} + n_8\mathrm{HC} + n_9\mathrm{H_2} + n_{10}\mathrm{C_{(S)}}, \tag{2.3}$$

where C_xH_y is either methane or propane depending on which fuel was used for combustion, and CH_4, C_2H_6 and C_3H_8 are unburnt hydrocarbons (HC) observed by the GC in the products, while n_i are coefficients determined either by inflow mass flow controllers or GC measurements of the products. It was assumed that nitrogen (N_2) was an inert gas and is the only product with nitrogen atoms. This was concluded based on observing low concentration of NO_x during decomposition (below 200 ppm for different methane flow rates), measured by an exhaust gas analyzer (Vetronix, Model PXA-1100).

Knowing that mass flow rate of N_2 is conserved, molar flow rate of N_2 would be the same before and after entering the reaction chamber ($\dot{n}_{\mathrm{N_2,in}} = \dot{n}_{\mathrm{N_2,out}}$). The molar flow rate of N_2 in the inlet ($\dot{n}_{\mathrm{N_2,in}}$) was calculated from

$$\dot{n}_{\mathrm{N_2,in}} = 0.78\,\dot{n}_{air,\mathrm{in}} = 0.78\,(\frac{\dot{V}_{\mathrm{air,in}}\,\rho_{\mathrm{air}}}{\mathcal{M}_{\mathrm{air}}}), \tag{2.4}$$

Where 0.78 is the mole fraction of N_2 (O_2 at 21% and Ar at 1%), $\dot{V}_{\mathrm{air,in}}$ is the standard flow rate of air mixed with the fuel and set by a mass flow controller, ρ_{air} is the density of air at standard conditions, and $\mathcal{M}_{\mathrm{air}}$ is the molar mass of air. $\dot{n}_{\mathrm{N_2,out}}$ was found by

$$\dot{n}_{\mathrm{N_2,out}} = \dot{n}_{\mathrm{N_2,in}} = y_{\mathrm{N_2,GC}}\,\dot{n}_{\mathrm{total,out}}, \tag{2.5}$$

where $y_{\mathrm{N_2,GC}}$ is the mole fraction of N_2 in the products measured by the GC, and $\dot{n}_{\mathrm{total,out}}$ is the total molar rate of gaseous components (excluding water vapor) and is unknown. Combining equations (2.4) and (2.5), $\dot{n}_{\mathrm{total,out}}$ was calculated from the equation below and used for finding molar rate of gaseous products in the exhaust:

$$\dot{n}_{\mathrm{total,out}} = \frac{0.78}{y_{\mathrm{N_2,GC}}}\,(\frac{\dot{V}_{\mathrm{air,in}}\,\rho_{\mathrm{air}}}{\mathcal{M}_{\mathrm{air}}}). \tag{2.6}$$

The molar flow rate of decomposition product *i* is the product of molar fraction of *i* measured by the GC ($y_{i,\mathrm{GC}}$) and $\dot{n}_{\mathrm{total,out}}$;

$$\dot{n}_{i,\mathrm{out}} = y_{i,\mathrm{GC}}\,\dot{n}_{\mathrm{total,out}}. \tag{2.7}$$

Thus, the mass flow rate of gaseous component of *i* (or undecomposed methane if *i*=CH_4) in the exhaust can be obtained from

$$\dot{m}_{i,\mathrm{out}} = \dot{n}_{i,\mathrm{out}}\,\mathcal{M}_i = y_{i,\mathrm{GC}}\,\dot{n}_{\mathrm{total,out}}\,\mathcal{M}_i, \tag{2.8}$$

where $\mathcal{M}_i$ is the molar mass of i.

2.2.2 Hydrogen Production Efficiency

Hydrogen production efficiency is defined as the fractional amount of hydrogen atoms that were part of the methane and released in form of H_2 through decomposition process, and was evaluated as

$$\eta_{H_2} = \frac{\dot{m}_{H_2,out}}{\dot{m}_{H,in}}, \tag{2.9}$$

where $\dot{m}_{H_2,out}$ is the mass flow rate of H_2 yielded by the decomposition and $\dot{m}_{H,in}$ is the mass flow rate of hydrogen atoms in the decomposition methane introduced to the reaction chamber. $\dot{m}_{H_2,out}$ can be obtained using equation (2.8) and (2.6), while $\dot{m}_{H,in}$ can be obtained from

$$\dot{m}_{H,in} = \dot{m}_{CH_4,in} \frac{4\,\mathcal{M}_H}{\mathcal{M}_{CH_4}}, \tag{2.10}$$

where $\dot{m}_{CH_4,in}$ is the mass flow rate of injected methane that can be calculated by equation (2.2), $\mathcal{M}_H$ and $\mathcal{M}_{CH_4}$ are the molar mass of atomic hydrogen and methane, respectively.

2.2.3 Carbon Black Number-size Distribution

The number-size distribution of carbon black in diluted samples of products was measured by a sequential arrangement of the DMA and CPC (also known as a scanning mobility particle sizer; SMPS) for the particle size range of 15 to 700 nm as shown arrangement A in Figure 2.1. This distribution was later corrected with a dilution factor to obtain undiluted number-size distribution of particles.

Dilution ratio was calculated based on the simultaneously measurement of CO_2 in undiluted samples of exhaust (measured by the GC) and nitrogen diluted samples (measured by the CO_2 analyzer) using

$$DR = \frac{[CO_2]_{\text{undiluted}}}{[CO_2]_{\text{diluted}}}. \tag{2.11}$$

2.2.4 Carbon Black Effective Density

Undenuded and denuded effective density of carbon black particles were measured by either bypassing or sampling through the catalytic denuder (heated to 400 ℃), respectively, before sending to a sequential conjunction of DMA, CPMA and CPC shown as arrangements B and C in Figure 2.1. In each case, effective density of carbon black (ρ_{eff}) was measured for five particle diameters between 15 and 85 nm using

$$\rho_{\text{eff}}(d_{\text{m}}) = \frac{m(d_{\text{m}})}{\frac{\pi}{6} {d_{\text{m}}}^3}, \tag{2.12}$$

where $m(d_{\text{m}})$ is the median mass of particles (measured by CPMA) with mobility diameter of d_{m} (set by DMA).

Since the mass of a particle has a power-law relationship with the particle mobility diameter,

$$m(d_{\text{m}}) = C\, {d_{\text{m}}}^{D_{\text{m}}}, \tag{2.13}$$

effective density and mobility diameter of the particle was correlated as

$$\rho_{\text{eff}}(d_{\text{m}}) = k\, {d_{\text{m}}}^{D_{\text{m}}-3}, \tag{2.14}$$

where k (the prefactor) and D_{m} (the mass-mobility exponent) was determined by fitting a power-law relation to data points.

2.2.5 Carbon Black Mass-size Distribution

Mass of a carbon black particle ($m(d_{\text{m}})$) with mobility diameter of d_{m} is defined as

$$m(d_{\text{m}}) = \frac{\pi}{6}\, \rho_{\text{eff,undenuded}}(d_{\text{m}})\ {d_{\text{m}}}^{3}, \tag{2.15}$$

where $\rho_{\text{eff,undenuded}}(d_{\text{m}})$ is the undenuded effective density and can be estimated using equation (2.14) with the corresponding prefactor and mass-mobility exponent. Calculating $m(d_{\text{m}})$ for each size of j between 15 and 700 nm, the undiluted mass-size distribution can be estimated by using

$$\left(\frac{\text{d}M}{\text{dlog}(d_{\text{m}})}\right)_{j,\text{undiluted}} = m(d_m)_j \left(\frac{\text{d}N}{\text{dlog}(d_{\text{m}})}\right)_{j,\text{undiluted}}, \tag{2.16}$$

where $\left(\frac{\text{d}N}{\text{dlog}(d_{\text{m}})}\right)_{j,\text{undiluted}}$ is obtained from the undiluted number-size distribution. Consequently, the total mass concentration of undenuded particles in the size range of 15 to 700 nm was determined from

$$M_{\text{total,undiluted}} = \sum_i \left[\left(\frac{\text{d}M}{\text{dlog}(d_{\text{m}})}\right)_{j,\text{undiluted}} \text{dlog}(d_{\text{m}})_j\right]. \tag{2.17}$$

2.2.6 Carbon Black Volatile Mass Fraction

Volatile mass fraction is a measure of morphological mixing state and defined as mass of volatile materials coated on a particle divided by the total mass of the particle. This value can be obtained by two sets of measurements that determine mass of denuded and undenuded carbon black particles with the same undenuded mobility diameter. For this purpose, after passing through the long DMA, diluted samples proceeded through either the catalytic denuder (heated to 400 ℃) or its bypass, then followed to a sequential arrangement of CPMA and CPC to obtain median mass of denuded and undenuded particles ($m_{\mathrm{D}}(d_{\mathrm{m}})$ and $m_{\mathrm{U}}(d_{\mathrm{m}})$, respectively) as shown in arrangement C in Figure 2.1. Volatile mass fraction of carbon black ($f_{\mathrm{vm}}(d_{\mathrm{m}})$) was calculated for five equally distanced particle sizes between 15 and 85 nm using

$$f_{\mathrm{vm}}(d_{\mathrm{m}}) = 1 - \frac{m_{\mathrm{D}}(d_{\mathrm{m}})}{m_{\mathrm{U}}(d_{\mathrm{m}})}, \tag{2.18}$$

where d_{m} is the undenuded mobility diameter.

2.2.7 Carbon Black Production Efficiency

Carbon black production efficiency is the efficiency of releasing carbon atoms of the decomposition methane in form of solid carbon particles (carbon black, CB), which can be determined by

$$\eta_{\mathrm{CB}} = \frac{\dot{m}_{\mathrm{CB,out}}}{\dot{m}_{\mathrm{C,in}}}, \tag{2.19}$$

where $\dot{m}_{\mathrm{CB,out}}$ is the mass flow rate of carbon black formed by methane decomposition and $\dot{m}_{C,in}$ is the mass flow rate of carbon atoms in the decomposition methane introduced to the reaction chamber.

In order to obtain $\dot{m}_{\mathrm{CB,out}}$, the total mass concentration of undiluted carbon black ($M_{\mathrm{total,undiluted}}$) was estimated from equation (2.17) and used in

$$\dot{m}_{\mathrm{CB,out}} = M_{\mathrm{total,undiluted}}\, \dot{V}_{\mathrm{total,out}}, \tag{2.20}$$

where $\dot{V}_{\mathrm{total,out}}$ is the total flow rate of products in the exhaust, and calculated from the equation below at the static pressure and temperature of CPC (P=101 kPa and T=294.25 K), at which $M_{\mathrm{total,undiluted}}$ was measured:

$$\dot{V}_{\mathrm{total,out}} = \frac{\dot{n}_{\mathrm{total,out}}\, \bar{R}\, T}{P}, \tag{2.21}$$

where $\dot{n}_{\mathrm{total,out}}$ is the total molar rate of gaseous products (excluding water vapor) in the exhaust that was determined from equation (2.6), and $\bar{R}$ is the universal gas constant.

Furthermore, $\dot{m}_{\mathrm{C},in}$ was calculated by

$$\dot{m}_{C,in} = \dot{m}_{CH_4,in} \frac{\mathcal{M}_{\mathrm{C}}}{\mathcal{M}_{\mathrm{CH_4}}}, \tag{2.22}$$

where $\dot{m}_{\mathrm{CH_4,in}}$ is the mass flow rate of decomposition methane that was obtained from equation (2.2), $\mathcal{M}_{\mathrm{C}}$ and $\mathcal{M}_{\mathrm{CH_4}}$ are the molar mass of atomic carbon and methane, respectively.

2.2.8 Carbon Black TEM Image Analysis

TEM imaging of collected samples was performed by a transmission electron microscope (JEOL, Model JEM 2100) at 200 kV to study carbon black structures. On average, 40 images per condition were taken at the center and four other locations around the grid, with an optimum focus, magnification (up to 200,000), and electron beam intensity. Image processing was

conducted using the method of Dastanpour, Boone, & Rogak (2016) to extract morphological parameters of carbon black, including area equivalent diameter of aggregates and average primary particle diameters in individual aggregates.

2.3 Equipment Description

2.3.1 Differential Mobility Analyzer (DMA)

Differential mobility analyzer (DMA) is an electrostatic classifier which separates particles based on their electrical mobility. This parameter is inversely proportional to the particle size and proportional to the number of chargers on the particle. The schematic diagram of the Long DMA (used in this study) is shown in Figure 2.2.

Before entering the DMA, polydisperse particles pass through a neutralizer, a radioactive bipolar charger, and receive either positive, negative, or zero charge(s). Consecutively, the charged aerosol sample enter the classifier from the top and flow in axial direction between the two narrow concentric cylinders of the classifier and smoothly merge with the laminar sheath-air flow, also introduced from the top. There is a voltage potential between the two cylinders of the classifier that induces a radial electrostatic force on charged particles. Charged particles also experience a drag force in the opposite direction of the electrostatic force. The balance between electrostatic and drag forces defines the trajectory of particles as they move downward. Therefore, only positively charged particles with a narrow range of electrical mobility reach circumferential slit in the center electrode and exit the DMA as Monodisperse Flow. Particles with negative charge(s) will stick to the outer electrode, while non-charged (neutral) particles will be carried out of DMA with sheath flow.

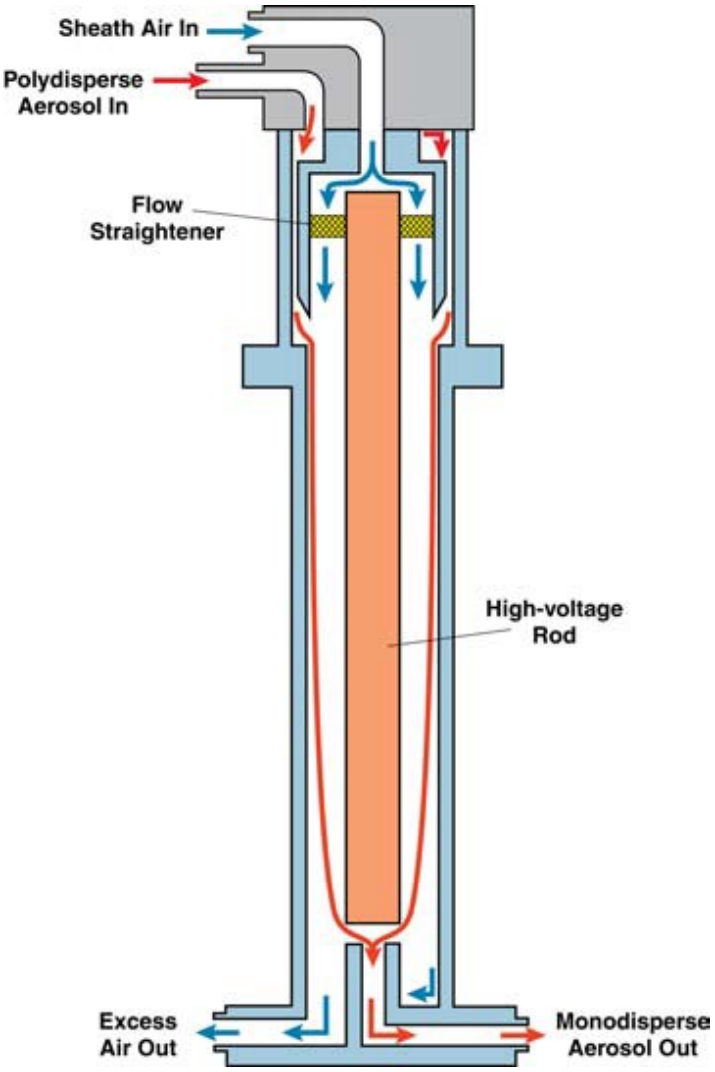

Figure 2.2. Schematic diagram of the Long DMA (from DMA manual).

2.3.2 Centrifugal Particle Mass Analyzer (CPMA)

Centrifugal particle mass analyzer (CPMA) is an aerosol classifier that separates particles based on their mass-to-charge ratio. The schematic diagram of the CPMA is shown in Figure 2.3.

CPMA consist of two concentric rotating cylinders with a voltage potential between them. Charged particles (by a neutralizer for example) enter in the axial direction between the two cylinders and undergo two opposing forces of electrostatic and centrifugal. The balance between these forces is driven by the particle mass-to-charge ratio. Only positively charged

particles which have the selected mass-to-charge ratio follow the trajectory through the classifier. As such, neutral particles and particles with negative charge(s) will impact and stick to the outer cylinder.

It should be noted that the CPMA's inner cylinder spin with slightly higher rotational speed than the outer cylinder. As a result, a stable centrifugal/electric field is created across the classification region which allows a particle with the correct mass-to-charge ratio transit the classifier if it enters at any point along the annular radius.

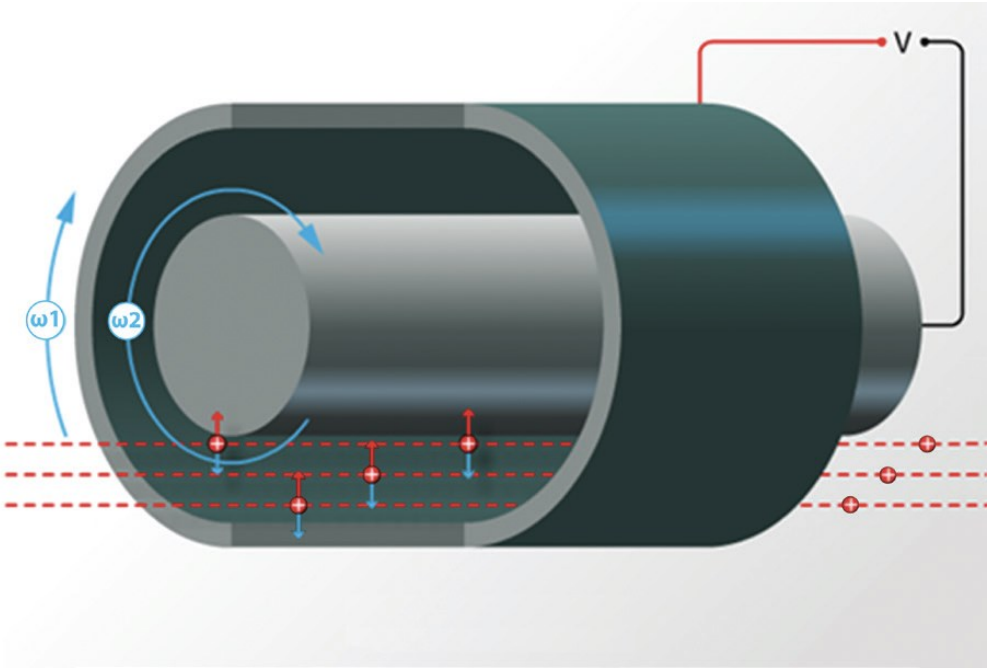

Figure 2.3. Schematic diagram of the CPMA (from CPMA manual).

2.3.3 Condensation Particle Counter (CPC)

Condensation particle counter (CPC) measures particle number concentration by condensing butanol on the particles to grow their size to the point they can be counted by an optical detector. The schematic diagram of the CPC is shown in Figure 2.4.

Upon entering the instrument, the aerosol is split into the aerosol sample flow and sheath flow. The sheath flow is cleaned by a HEPA filter and drown through a heated, liquid-soaked, porous tube where it becomes saturated with butanol vapor. The aerosol sample flow passes through a capillary tube and rejoins with the vapor-saturated sheath flow before entering the condenser where the combined sheath and aerosol flows are cooled using a thermoelectric device (TED). The supersaturated vapor condenses on the particles (condensation nuclei) and forms larger droplets in the condenser. The droplets later pass through a nozzle into the optical detector where particles are counted by continuous particle light scattering detection.

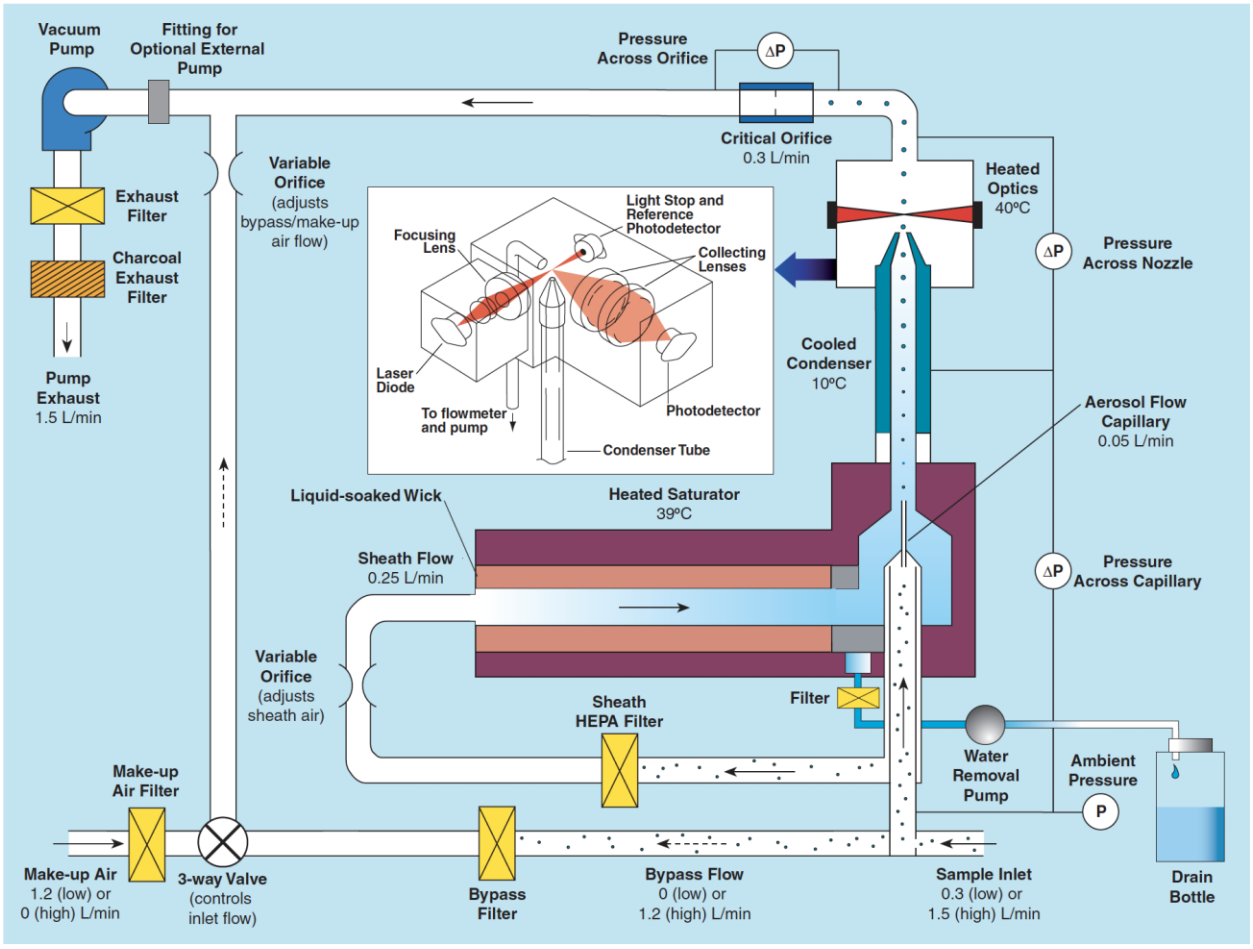

Figure 2.4. Schematic diagram of the CPC (from CPC manual).

2.3.4 Catalytic Denuder (Stripper)

The catalytic denuder (catalytic stripper) is a heated catalytic element that removes the semi-volatile fraction of aerosol particles. The schematic diagram of the catalytic stripper is shown in Figure 2.5.

The catalytic denuder consists of a heated oxidation catalyst and a heat exchanger that heat up the aerosol sample to 300–400 ℃ to remove semi-volatile components (typically organic carbon) from the raw or diluted aerosol samples.

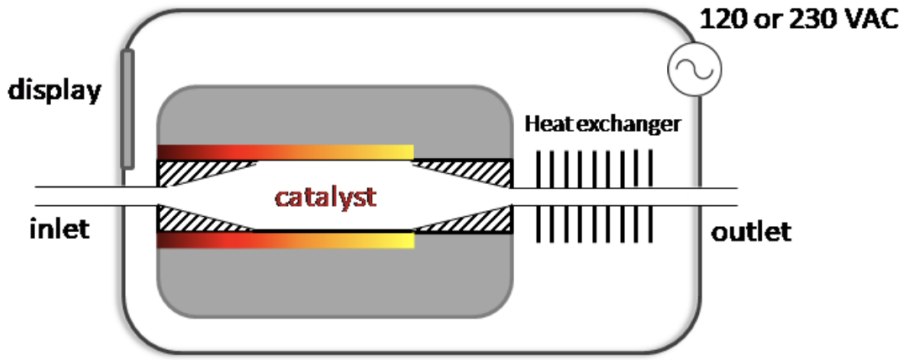

Figure 2.5. Schematic diagram of the catalytic stripper (from Catalytic Instruments website).

2.3.5 TEM Sampler (ESPnano)

The TEM sampler (ESPnano) is an electrostatic precipitator particle sampler that simultaneously charge and collect particles onto a sampling substrate for EM analysis. The schematic diagram of ESPnano presented in Figure 2.6.

ESPnano is a “point to plane” electrostatic precipitator that creates a very high voltage electric field using a sharp needle as the anode and a flat surface as the cathode. As aerosol sample flow enters the very intense electric field, particles become charged by ions generated

during the corona discharge at the anode needle. The charged particles subsequently drift quickly toward the cathode plate onto which a sampling substrate, such as TEM grid, has been mounted.

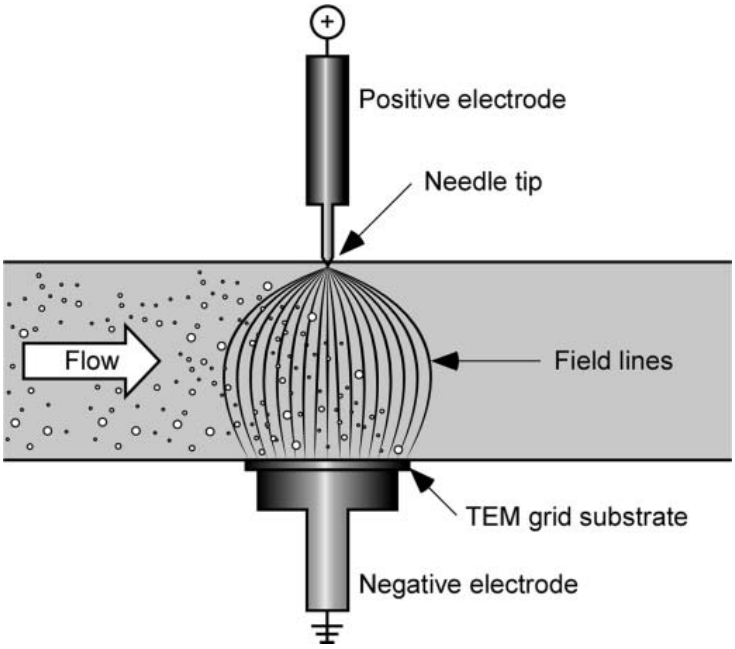

Figure 2.6. Schematic diagram of the ESPnano (from Miller et al. (2010)).

Chapter 3

Results and Discussion

3.1 Reaction Conditions

The product gas composition and properties of produced carbon black in the thermal decomposition of methane are highly influenced by reaction conditions such as temperature, pressure and residence time (Gautier et al. 2016; A. Abánades et al. 2011). Reaction conditions in the present study were mainly controlled by two parameters:

I. the fuel used, either propane or methane, in the premixed flame to create a steady-state, O_2-deficient, hot stream in the reaction chamber;
II. the flow rate of methane injected into the reaction chamber to decompose, which was varied between 0.5 and 5 SLPM.

The steady-state pressure in the reaction chamber was slightly above atmospheric pressure regardless of the fuel type ($1 < P < 1.1$ atm), while the steady-state temperature in the centerline of the reaction chamber was fuel dependent and decreases with distance from the premixed flame front. Figure 3.1 shows the temperature distribution along the centerline of the reaction chamber as a function of distance from the tip of the premixed flame for propane and methane fuels when no methane was added for thermal decomposition. As a general trend, the temperature reached 1150 ± 20 ℃ close to the flame front, and linearly decreased to 900 ± 20 ℃ within a quarter of the chamber length ($z = 14.5$ cm). Depending on the premixed flame, the temperature then decreased to below 400 ℃ approximately halfway down the reaction chamber. Further analysis for correcting the thermocouple temperature measurements are shown

in Appendix C. It was concluded that thermocouple measurements of premixed flame products were sufficiently accurate in this study and radiation correction only accounted for ~15 ℃ in the ideal case.

Residence time in the thermal decomposition of methane is inversely proportional to the total volumetric flow rate, relative to the time set by the flow of just the hot products from the premixed flame. Since the measurements were conducted at steady-state conditions, variation in the flow rate of injected methane not only affects the residence time by the total number of moles, but also the temperature of premixed flame products, resulting in an increased effect on the thermal decomposition process. Therefore, in this study, results are presented based on decomposition methane flow rate for each premixed flame used as the heat source.

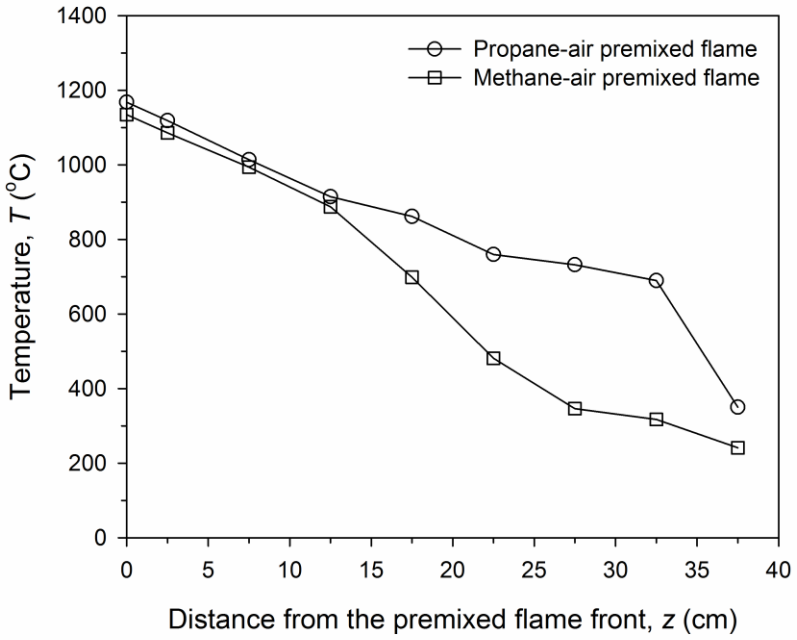

Figure 3.1. Steady-state temperature distribution along the centerline of reaction chamber, where $z = 0$ is the flame front and $z = -2.5$ cm is the top of reaction chamber.

3.2 Methane Destruction Efficiency

Figure 3.2 shows the destruction efficiency of methane in the hot products of propane- or methane-air premixed flames, as a function of decomposition methane flow rate. Error bars in Figure 3.2, or any other figure in this study, represent uncertainties with 95% confidence interval. The detailed calculation of uncertainties can be found in Appendix A. As shown in the figure, a maximum destruction efficiency of 96% and 92% was achieved under the lowest injected methane flow rate (0.5 SLPM) when using propane or methane as fuel, respectively. This result is comparable with modern non-catalytic methane cracking technologies using heat sources such as concentrated solar energy and plasma where the conversion efficiency exceeds 90% (Abbas & Wan Daud 2010).

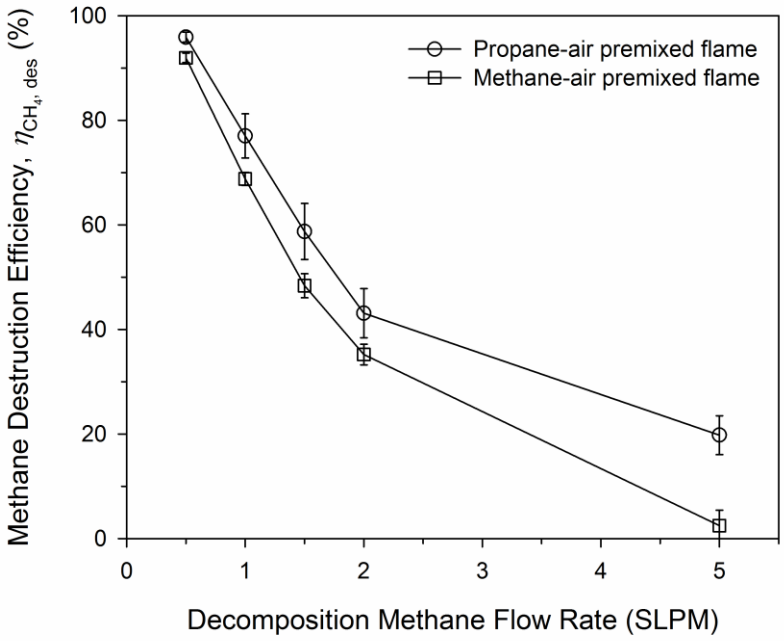

Figure 3.2. Destruction efficiency of methane with different flow rates of injection. Error bars represent 95% confidence interval.

Furthermore, Figure 3.2 indicates the combined effect of temperature and residence time on thermal decomposition of methane. As expected, the higher the decomposition methane flow rate, the lower the methane destruction efficiency. The difference in temperatures in the reaction chamber likely resulted in reduced methane destruction efficiencies, especially for higher flow rates of decomposition methane, when switching from propane to methane as the premixed flame feed.

3.3 Hydrogen and Carbon Black Production

The efficiency of hydrogen and carbon black production from decomposition of different flow rates of methane is presented in Figure 3.3. As expected, the highest production efficiencies correspond to the lowest decomposition methane flow rate (0.5 SLPM). For the propane-air or methane-air flames, the highest production efficiencies for hydrogen were 70% and 79%, respectively, and for carbon black is 0.84% and 0.08%, respectively. Both efficiencies decreased with an exponential decay function as the decomposition methane flow rate increased. The efficiency trend for carbon black production was clearly stratified by the type of premixed flame with the propane flame being more efficient, however hydrogen production efficiency seemed to be fuel independent, falling into one general trend for both premixed flames.

The very low production efficiency of carbon black was likely due to the increase in the formation of other species, mostly carbon monoxide (CO), through unfavorable processes, such as gasification, where most of carbon was consumed. A confirmation to this effect was the increased mole fractions of CO in the decomposition products.

(a)

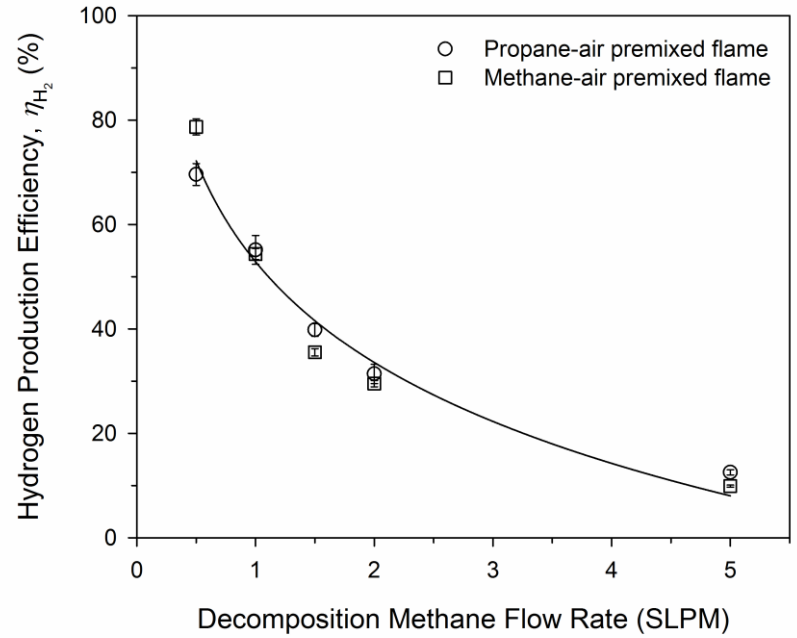

(b)

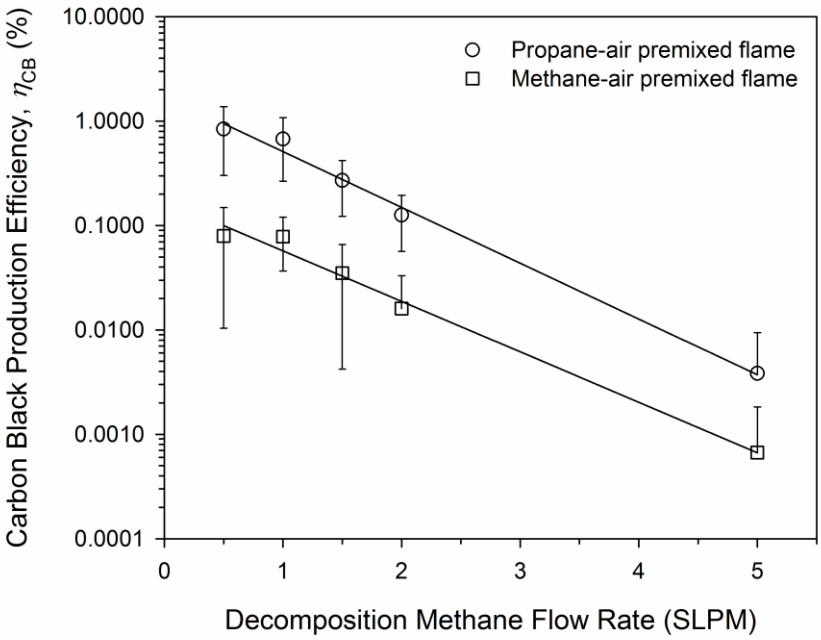

Figure 3.3. Production efficiency of (a) hydrogen and (b) carbon black from different flow rates of methane injection. Error bars represent 95% confidence interval.

3.4 Carbon Black Characteristics

3.4.1 Number-size Distribution

The number-size distribution of particles generated in each reaction condition can be seen in Figure 3.4 and the total number concentration and count median diameter (CMD) of particles in the SMPS size range of 15–700 nm are presented in Table 3.1. Depending on the fuel type used in the premixed flame, a similar pattern in size distributions was observed for decomposition methane flow rates of 2 SLPM or less. The number-size distributions appear to be bimodal in all cases with two distinguishable modes: one with a geometric mean diameter (GMD) between 10 and 25 nm, and another mode with a GMD of ~85 nm. In relation to the decomposition methane flow rate, trends of these modes were fuel independent whereby the GMD of the first mode shifted towards smaller particles and the second mode shrinks in number with the increase in decomposition methane flow rate. Changing the fuel in the premixed flame also seemed to affect size distribution modes. For a given decomposition methane flow rate, the GMD of the first mode and number concentration of the second mode were larger when using the propane-air premixed flame compared to those when methane was used as fuel.

At decomposition methane flow rates of 5 SLPM, the concentration of particles decreases significantly for both fuels. This is likely due to reduced residence time and reactor temperature at the higher flow rate.

(a)

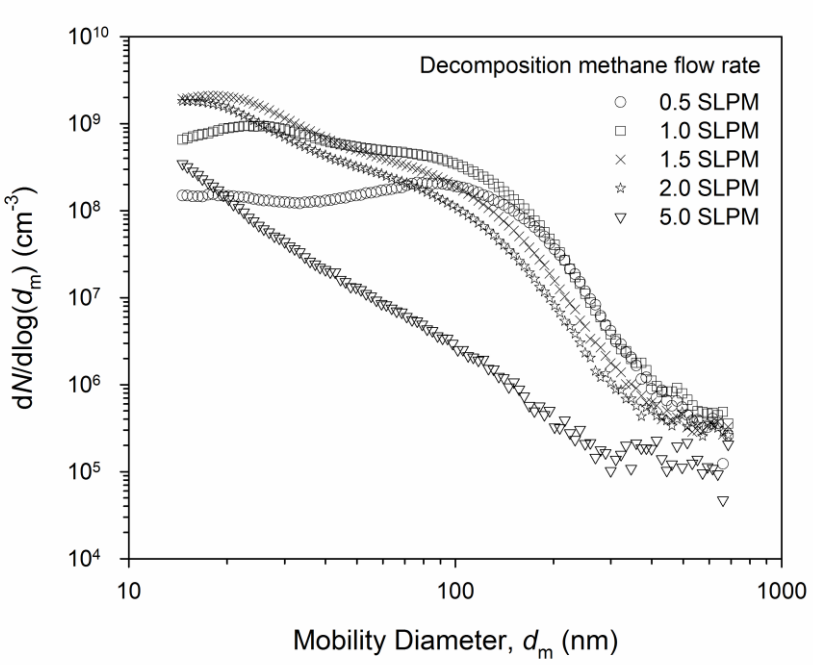

(b)

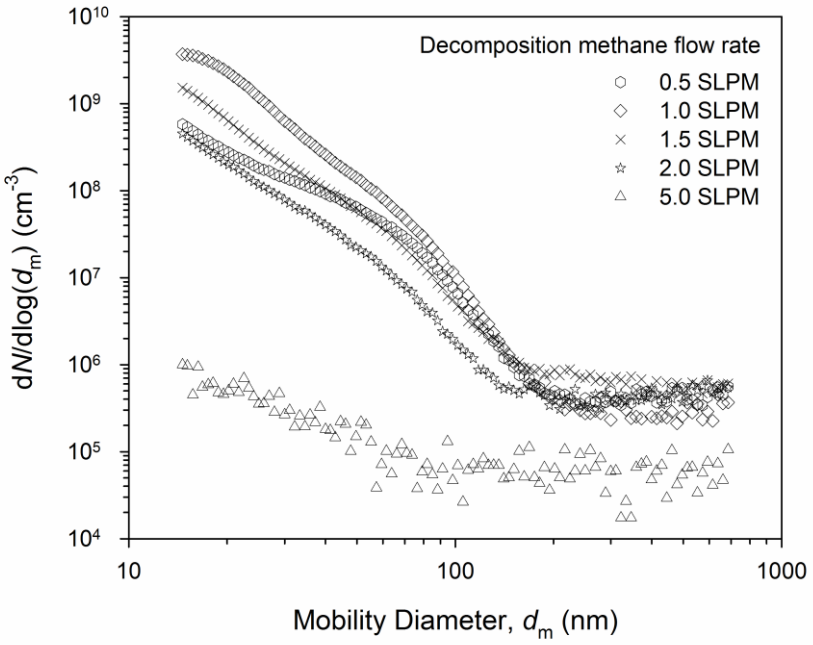

Figure 3.4. Number-size distribution of carbon black from different flow rates of methane injection in hot products of (a) propane-air and (b) methane-air premixed flame. Distributions are corrected by respective dilution factors.

Table 3.1. Summary of carbon black characteristics in the size range of 15–700 nm for all reaction conditions.

Heat source	Decomposition methane flow rate (SLPM)	Total number concentration of particles (cm^{-3})	Count median mobility diameter of particles (nm)	Total mass concentration of particles ($mg\ m^{-3}$)
Propane-air premixed flame	0.0	<10000	-	-
	0.5	$1.69\times10^{8} \pm 11\%$	$58 \pm 10\%$	$55.2 \pm 64\%$
	1.0	$6.18\times10^{8} \pm 17\%$	$33 \pm 4\%$	$88.1 \pm 60\%$
	1.5	$8.82\times10^{8} \pm 13\%$	$24 \pm 3\%$	$52.4 \pm 55\%$
	2.0	$6.26\times10^{8} \pm 11\%$	$22 \pm 3\%$	$31.8 \pm 55\%$
	5.0	$5.64\times10^{7} \pm 19\%$	$18 \pm 3\%$	$2.2 \pm 97\%$
Methane-air premixed flame	0.0	<10000	-	-
	0.5	$1.27\times10^{8} \pm 11\%$	$21 \pm 3\%$	$5.6 \pm 87\%$
	1.0	$7.89\times10^{8} \pm 12\%$	$19 \pm 3\%$	$10.7 \pm 53\%$
	1.5	$2.58\times10^{8} \pm 10\%$	$18 \pm 3\%$	$7.1 \pm 88\%$
	2.0	$8.26\times10^{7} \pm 11\%$	$19 \pm 3\%$	$4.2 \pm 106\%$
	5.0	$3.04\times10^{5} \pm 64\%$	-	$0.4 \pm 175\%$

3.4.2 Mass-size Distribution

Figure 3.5 compares mass-size distribution of particles from thermal decomposition of different methane flow rates. Plots of the undenuded effective density versus undenuded mobility diameter data, and the power-law fits with prefactor and mass-mobility exponent used for the calculation of mass concentrations in each setting are presented in Figure 3.6. As shown in the Figure 3.5, mass distributions were highly influenced by the variation of decomposition methane flow rate and the fuel type in the premixed flame. It also can be seen how the peaks in mass-size distributions are shifted toward larger particles compared to the number-size distributions in Figure 3.4. This result is because the majority of the mass is in larger particles.

(a)

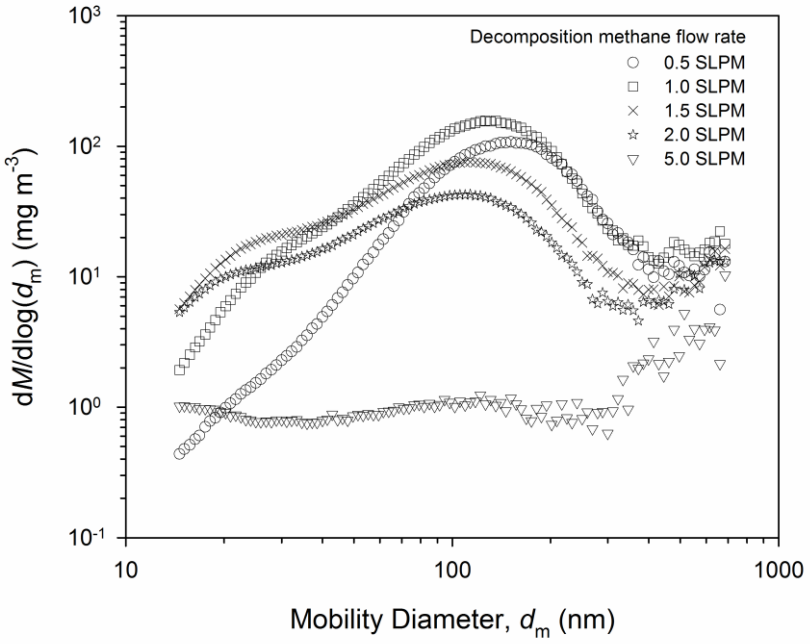

(b)

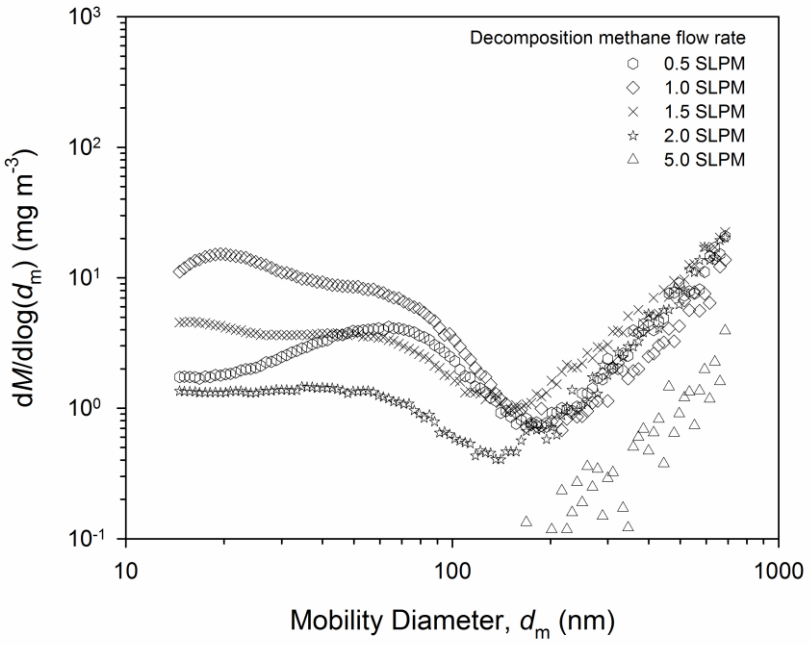

Figure 3.5. Mass-size distribution of carbon black from different flow rates of methane injection in hot products of (a) propane-air and (b) methane-air premixed flame. Distributions are based on undiluted mass concentration of undenuded particles.

(a)

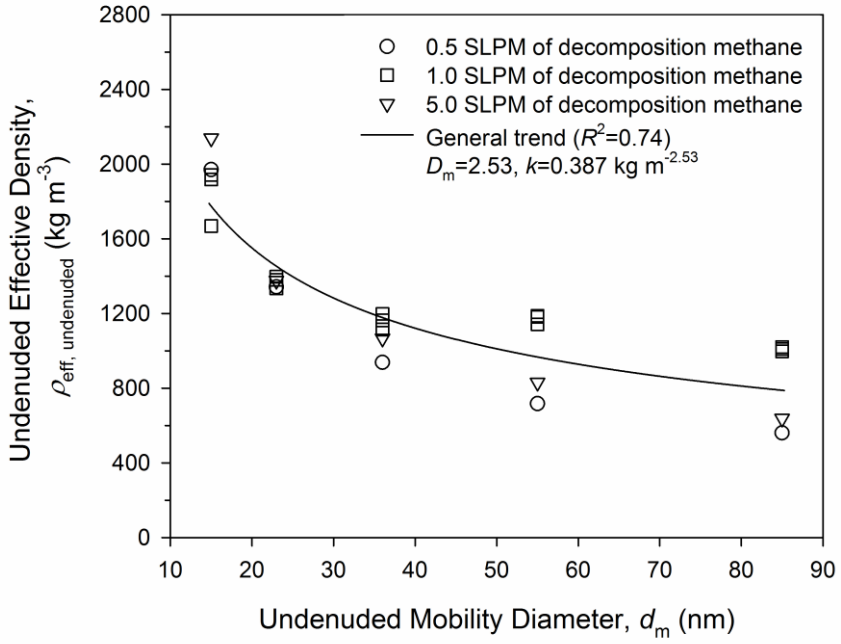

(b)

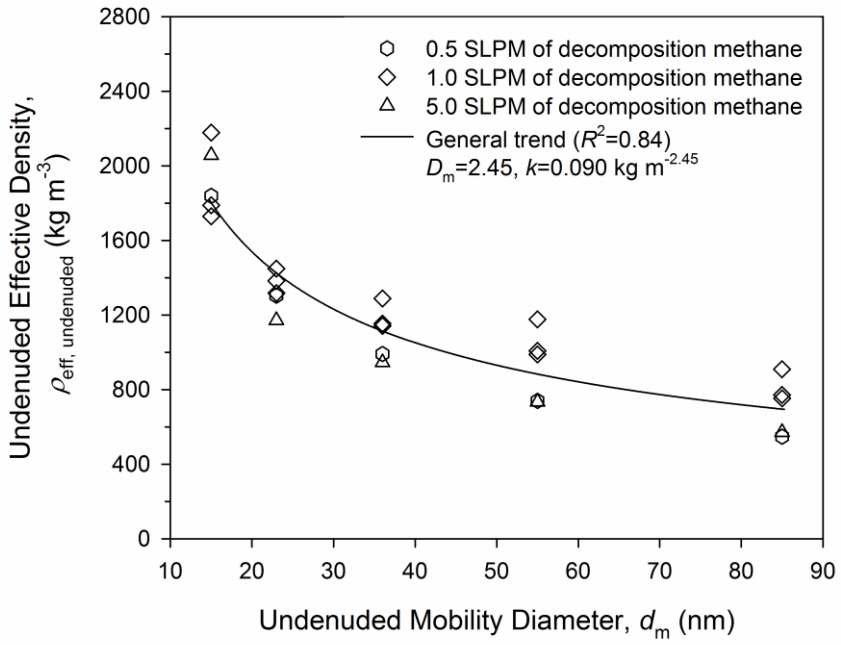

Figure 3.6. General trend of undenuded effective density as a function of undenuded mobility diameter, combining data from reaction conditions of different decomposition methane flow rates when using (a) propane-air or (b) methane-air premixed flame as the heat source.

Compared to the methane-air premixed flame, mass concentrations using propane-air premixed flame were generally higher by one order of magnitude. Table 3.1 highlights the total mass concentration differences in each reaction condition. The total mass concentration increased to its maximum (88.1 ± 60% and 10.7 ± 53% mg m^{-3} at 1 SLPM of decomposition methane using propane- and methane-air premixed flame, respectively), then followed a continuous decreasing trend with the increasing methane flow rate.

3.4.3 Volatility and Internal Mixing State

The size-segregated internal mixing state of carbon black from the thermal decomposition of methane can be seen from Figure 3.7 which plots the volatile mass fraction as a function of mobility diameter of particles. Generally, volatile mass fractions for a given decomposition methane flow rate were few percentages higher when using propane as the premixed flame feed, compared to those of methane feed. It is important to note that the relatively large confidence intervals in some results were attributed to the low repeatability of the volatility, rather than inaccuracies in the instruments. This day-to-day variability is attributed to subtle changes in burner flows or the variation within the dilution system, resulting in different particle composition. The uncertainty analysis for all measurements is shown in Appendix A.

Particles from the decomposition of 0.5 and 5 SLPM of methane had relatively similar volatile mass fractions, falling between 10% and 30%, with little dependency on particle size or fuel. On the other hand, particles from the decomposition of 1 SLPM of methane had relatively large amounts of internally mixed volatile material. At this condition, the volatile mass fraction was ~55% for small particle sizes, and with increasing size, decreased gradually to about 40% or 30% depending on the fuel type used in the premixed flame (propane or methane, respectively).

This increased level of volatility was consistent with observations on undenuded effective densities in the same size range of 15–85 nm, where particles from decomposition of 1 SLPM of methane were much denser compared to those of 0.5 or 5 SLPM of decomposition methane. The reason is that the condensation of volatile materials, even though these components have lower densities than carbon black, tend to increase the undenuded effective density of the particles by filling the voids. As such, the volatile material in the voids of the particle do not significantly change the mobility diameter of a particle, it rather increases the particle's mass and hence its effective density (Ghazi et al. 2013).

The decreasing trend in volatile mass fraction as a function of mobility diameter has also been observed for particles emitted from diesel engines (Sakurai et al. 2003; Ristimäki et al. 2007), gasoline direct injection engines (Momenimovahed & Olfert 2015), a compression-ignition natural-gas direct-injection engine (Graves, Olfert, Patychuk, Dastanpour, & Rogak, 2015), a helicopter gas turbine engine (Olfert et al., 2017), as well as premixed flames (Ghazi et al., 2013) and diffusion flames (Dickau et al. 2016).

(a)

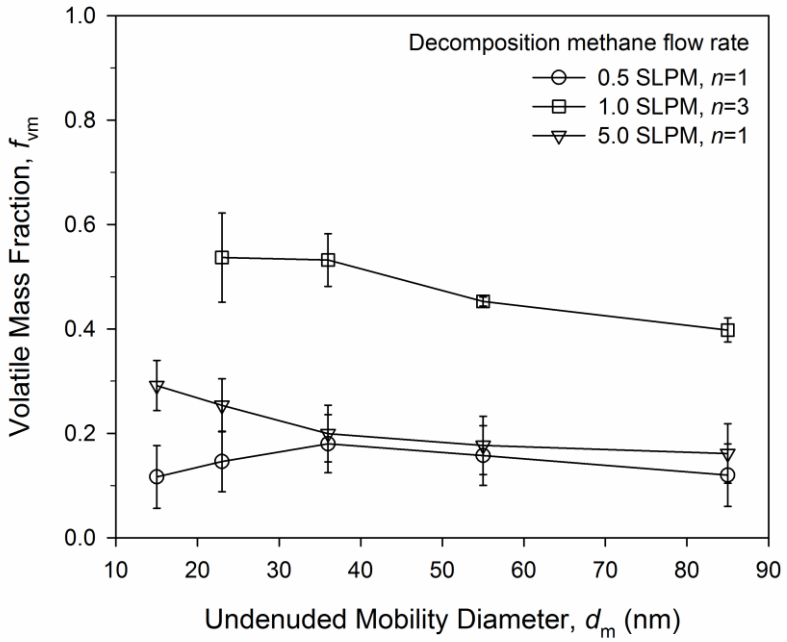

(b)

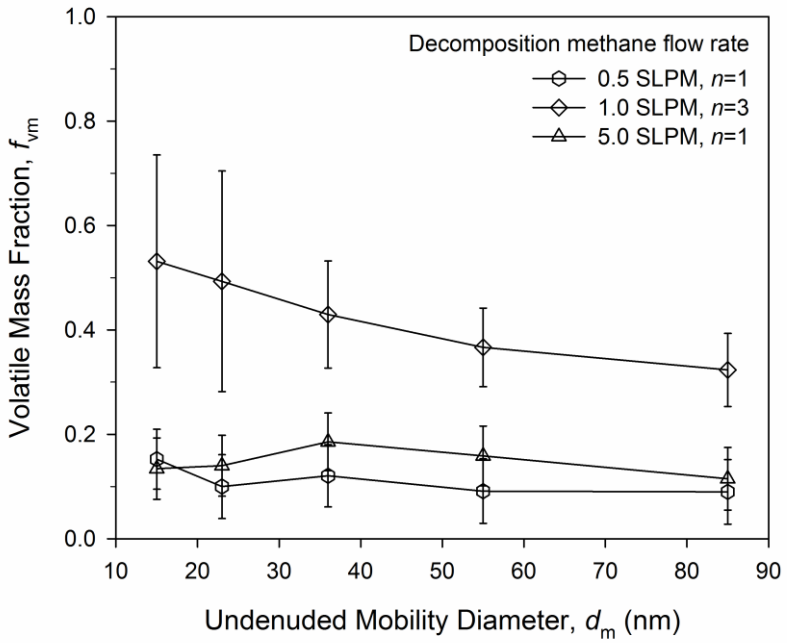

Figure 3.7. Volatile mass fraction of carbon black as a function of undenuded mobility diameter for different flow rates of methane injection in hot products of (a) propane-air and (b) methane-air premixed flame. Error bars represent 95% confidence interval. Decomposition methane flow rates of 0.5, 1 and 5 were tested n=1, 3 and 1 times at each setting of heat source.

3.4.4 Denuded Effective Density and Mass-mobility Exponent

Denuded effective density data from thermal decomposition of 0.5, 1 and 5 SLPM of methane at the two settings of heat source are plotted in Figure 3.8, provides more information on the aggregate structure of carbon black since the volatile materials are removed. As shown in Figure 3.8, the denuded effective density decreased with increasing mobility diameter for all conditions. This change was expected because larger aggregates incorporate relatively more open space between their primary particles, hence, the effective density drops as the aggregate size increases. Although there were systematic differences between denuded effective density of different conditions, for example particles from decomposition of 1 SLPM of methane were typically denser irrespective of fuel type used in the premixed flame, these data were still somewhat grouped and could be represented by a general power-law fit. The solid line in Figure 3.8 represent the fit, with the prefactor and mass-mobility exponent shown in the legend. Almost all the data (more than 90%) collapse within $\pm$20% of the fit throughout the given size range (15–85 nm) as shown by the shaded region. From this, it can be perceived that denuded effective density of carbon black remains quite similar despite the differences in number- or mass-size distribution that particles have in different reaction conditions.

Graves (2015) proposed a combined mass-mobility exponent of 2.49 for denuded effective density of soot from a wide range of internal combustion engines, where $\pm$27% of the fit with $k = 0.131$ kg $m^{-2.49}$ could enclose 90% of the densities measured with non or low volatility from several sources including diesel engines (Park et al. 2003; Maricq & Xu 2004; Olfert et al. 2007), gasoline direct injection engines (Momenimovahed & Olfert 2015; Quiros et al. 2015; Graves et al. 2017), a port injected gasoline engine (Quiros et al. 2015), and a compression-ignition natural-gas direct-injection engine (Graves et al. 2015). The dashed line in

Figure 3.8 shows this combined trend. In comparison to soot from internal combustion engines, the current denuded effective density of carbon black is higher at small particle sizes and reaches approximately same value for large particles. The similarity in denuded effective densities of engine soot and carbon black perhaps can be explained by the similarity in size and number of primary particles within their aggregates of the same mobility diameter. This similarity is quite interesting as the engine soot and carbon black are formed in substantially different environments.

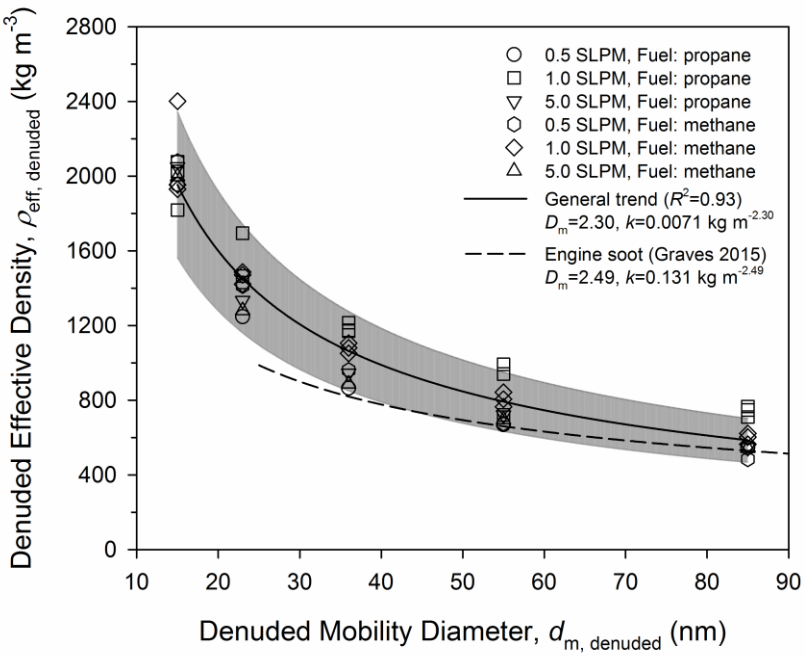

Figure 3.8. General trend of denuded effective density as a function of denuded mobility diameter, combining data from reaction conditions of different decomposition methane flow rates (SLPM) and fuel types (propane or methane) used in the premixed flame. Shaded region encloses ±20% of the fit which contains 92% of data points. Dashed line represents the combined trend of denuded effective density of soot from various internal combustion engines.

3.4.5 Morphology and Primary Particle Diameter

TEM imaging has been widely used for qualitative interpretation and quantitative analysis of nanostructure and morphological properties of carbon black (Palotás et al. 1996; Gaddam et al. 2016). TEM observations on the structure of aggregates are often linked to the bulk properties of carbon black such as oil absorption, nitrogen surface area, and thermal and electrical conductivity. The aggregate shape and the size of primary particles are considered as the key parameters to specify this relationship; aggregates with highly branched structure tend to increase the liquid absorption capacity of carbon black and are suitable for developing intra-porosity, whereas aggregates with reduced branched structure and concentric graphene layers generally increase the percolation properties and electrical conductivity of blacks used as filler in composites. Moreover, the surface area, another important factor in the absorption properties and grade classification of carbon black, is inversely proportional to the size and fractal dimension of aggregates, and further to the size of primary particles (Kim, Seo, Nam, Ju, & Hong, 2005; Serrano, Botas, & Guil-Lopez, 2009; Fulcheri, Probst, Flamant, Fabry, Grivei, & Bourrat, 2002).

Herein, the size of aggregates, d_a, and the average size of primary particles in individual aggregates, d_p, were investigated through TEM image analysis. More than 350 TEM images (over 400 aggregates) were analyzed for all the reaction conditions. Figure 3.9 shows a typical morphology of produced carbon black composed of several primary particles (all the TEM images can be found in Appendix B).

Figure 3.10 shows the relationship between average primary particle diameter and the projected area diameter of individual particles. It has been shown that the projected area diameter is approximately equal to the mobility diameter of aggregates (Rogak et al. 1993). The figure shows that d_p appears to increase with increasing d_a, a correlation that can be best presented by a

power-law fit, $d_{\mathrm{p}} = k_{\mathrm{TEM}}\, {d_{\mathrm{a}}}^{n}$, where $k_{\mathrm{TEM}} = 1.92$ (1.36, 2.70) and $n = 0.47$ (0.39, 0.54) when diameters are used in nanometers (values in parenthesis are 95% confidence intervals). An increasing trend of d_{p} as a function of d_{a} has been also observed for soot particles from many combustion sources as shown in the work of Dastanpour & Rogak (2014) that included soot samples from a gasoline direct injection engine, a high pressure direct injection natural gas engine, an aviation gas turbine, and a laminar diffusion flame. Similar to soot from combustion processes, the average d_{p} in individual aggregates of carbon black increases from ~5 nm to 40 nm with increasing area equivalent diameter of aggregates from 10 nm to 350 nm. The comparison can be elaborated upon by obtaining the combined trend of d_{p} versus d_{a} for soot aggregates, as shown with the dashed line in Figure 3.10, using the following equation that was suggested by Eggersdorfer, Gröhn, Sorensen, McMurry, & Pratsinis (2012) for calculation of Sauter mean diameter of primary particles (d_{va}) based on mobility diameter and mass of the particles:

$$d_{\mathrm{va}} = \left(\frac{\pi k_{\mathrm{a}} \rho}{6m} (d_{\mathrm{m}})^{2D_\alpha}\right)^{\frac{1}{2D_\alpha - 3}}. \tag{3.1}$$

Assuming $d_{\mathrm{va}} = d_{\mathrm{p}}$ and knowing that mass of an aggregate is equal to $\frac{\pi}{6} k {d_{\mathrm{m}}}^{D_{\mathrm{m}}}$ (a combination of equations (2.12) and (2.14)), the equation above can be expressed as

$$d_{\mathrm{p}} = \left(\frac{k_{\mathrm{a}} \rho}{k}\right)^{\frac{1}{2D_\alpha - 3}} (d_{\mathrm{m}})^{\frac{2D_\alpha - D_{\mathrm{m}}}{2D_\alpha - 3}}, \tag{3.2}$$

where in the case of soot from combustion sources, k_{a} and D_α are optimized by Dastanpour, Rogak, et al. (2016) and are equal to 1.13 and 1.1, respectively. The density (ρ) is assumed to be 1800 kg m^{-3}, and the prefactor (k) and mass-mobility exponent (D_{m}) are equal to 0.131 kg m$^{-2.49}$

and 2.49, respectively, based on the work of Graves (2015). Assuming $d_{\mathrm{m}} = d_{\mathrm{a}}$ and substituting those values, this equation was simplified as

$$d_{\mathrm{p}} = 3.15\, {d_{\mathrm{a}}}^{0.3625}, \tag{3.3}$$

when the diameters are expressed in nanometers. It can be seen the trend lines of d_{p} versus d_{a} for soot and carbon black (dashed line and solid line in Figure 3.10, respectively) are in good agreement, confirming a similar structure in their aggregates which was previously suggested by their relatively close denuded effective density in Figure 3.8.

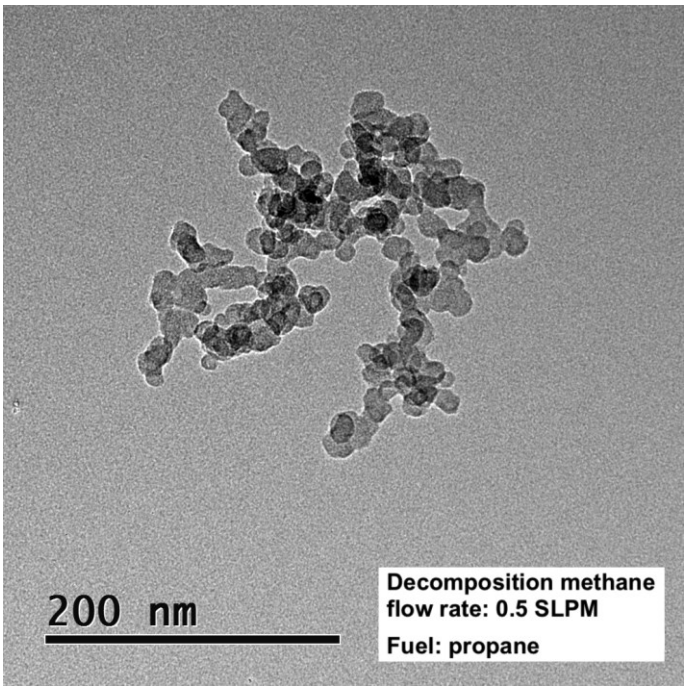

Figure 3.9. TEM image of the typical morphology of carbon black from thermal decomposition of methane in products of premixed flames.

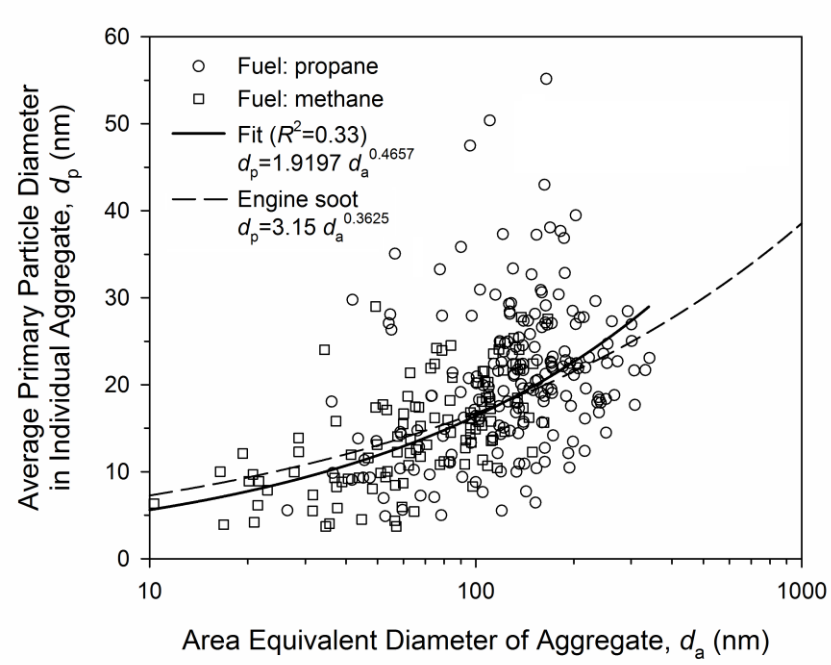

Figure 3.10. General trend of primary particle diameter as a function of aggregate size, combining data from thermal decomposition of methane with different types of fuel (propane or methane) used in the premixed flame. Dashed line represents the combined trend of average primary particle diameter in soot aggregates from various internal combustion engines.

An important ramification of the scaling between primary particle size and aggregate size is that the average primary particle size can be controlled by changing the median diameter of the aggregates. For example, it was shown in Figure 3.4 that the median mobility diameter of the aggregates can be changed by the fuel type or the flow rate of decomposition methane. This is confirmed in Figure 3.11, which presents the relation between d_p and d_a with respect to different flow rates of decomposition methane for the two fuels. The 95% confidence intervals in the average size of aggregates and primary particles suggests a wide variation of carbon black morphology at each condition; however, the d_p to d_a relationship seems to be well stratified based on the fuel type by following two distinct power-law trends. (With the exception of the 5 SLPM

cases, which had a relatively low sample size and where the image analysis was potentially biased to larger aggregates). Thus, if this carbon black manufacturing method was used industrially, the average primary particle size could be controlled by changing the fuel type or the flow rate of decomposition methane.

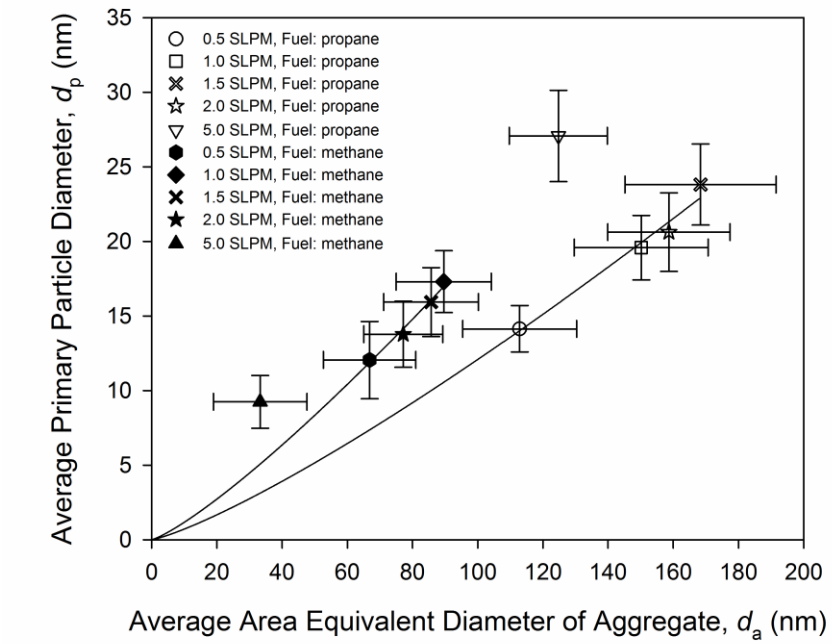

Figure 3.11. Average primary particle diameter as a function of average aggregate size from reaction conditions of different decomposition methane flow rates (SLPM) and fuel types (propane or methane) used in the premixed flame. Error bars represent 95% confidence interval.

A morphological comparison between the carbon black produced by the present method and the commercial processes of carbon black production revealed that the primary particle diameter and aggregate size of carbon black from TDM in the products of premixed flames were more similar to those of furnace black rather than thermal black (see Table 3.2.). The average primary particle diameter and average aggregate diameter of carbon black from TDM in products of premixed flames were in the range of 10–25 nm and 30–170 nm and relatively closer to

rubber-grade furnace black in groups 1 and 2 of ASTM designation (see Table 3.3.). Table 3.4 shows the primary particle size, aggregate size, Stokes diameter and surface area of different grades of carbon black as for reference.

Table 3.2. Morphological properties of different types of carbon black.

Carbon black	Surface area (m^2/g)	Approximate diameter of primary particle size (nm)	Diameter of aggregate (nm)	Size of agglomerate
Furnace black	12–240	10–400	50–400	Large (<2 mm)
Thermal black	6–15	120–500	400–600	Large (<2 mm)
Channel black	-	10–30	50–200	Large (<2 mm)
Lamp black	15–25	60–200	300–600	Large (<2 mm)
Acetylene black	15–70	30–50	350–400	Palletizes poorly

From Black et al. (2010)

Table 3.3. Particle size and surface characteristics of different groups of rubber-grade carbon black.

Group number	Typical average primary particle size (nm)	Average surface area (m^2/g)
0	0–10	>150
1	11–19	121–150
2	20–25	100–120
3	26–30	70–99
4	31–39	50–69
5	40–48	40–49
6	49–60	33–39
7	61–100	21–32
8	101–200	11–20
9	201–500	0–10

From Auchter (2005)

Table 3.4. Summary of carbon black morphology for different ASTM grades.

ASTM designation	Primary particle size[a], D_{wm}[b] (nm)	Aggregate size[a], D_{wm}[b] (nm)	D_{st}[c] (nm)	Surface area[a] (m^2/g)
N10	27	93	76–111	143
N220	32	103	95–117	117
N234	31	109	74–96	120
N326	41	108	98	94
N330	46	146	116–145	80
N339	39	122	96–125	96
N351	50	159	127	75
N375	36	106	91	105
N550	93	240	220–242	41
N660	109	252	227–283	34
N774	124	265	261	30
N990	403	593	436	9

From Wang et al. (2011)

[a]Measured by TEM

[b]D_{wm} = weight mean diameter = $\sum nd^4 / \sum nd^3$

[c]Stokes diameter by centrifugal sedimentation from various sources

3.5 Carbon Black Production to Energy Consumption Ratio

Knowing the mass flow rate of carbon black formed by the methane decomposition from equation (2.20), the carbon black production to energy consumption ratio was obtained from

$$\eta_{\text{CB to Energy}} = \frac{\dot{m}_{\text{CB,out}}}{\dot{V}_{\text{fuel}}\,\rho_{\text{fuel}}\,HHV_{\text{fuel}} + \dot{V}_{\text{methane}}\,\rho_{\text{methane}}\,HHV_{\text{methane}}}, \tag{3.4}$$

where $\dot{V}_{\text{fuel}}$ and $\dot{V}_{\text{methane}}$ are the standard mass flow rate of fuel (either propane or methane) and decomposition methane, respectively, ρ is density, and HHV_{fuel} and HHV_{methane} are the mass-based higher heating value of fuel and decomposition methane, respectively. Figure 3.12 shows

the trend of carbon black production to energy consumption ratio for different flow rates of decomposition methane at the two settings of heat source. Regardless of the type of fuel, this ratio reached to its maximum when the decomposition methane flow rate was at 1 SLPM and decreased exponentially for higher flow rates of decomposition methane. Furthermore, using propane as the fuel resulted in higher ratios of carbon black production to energy consumption ratio, compared to methane as fuel.

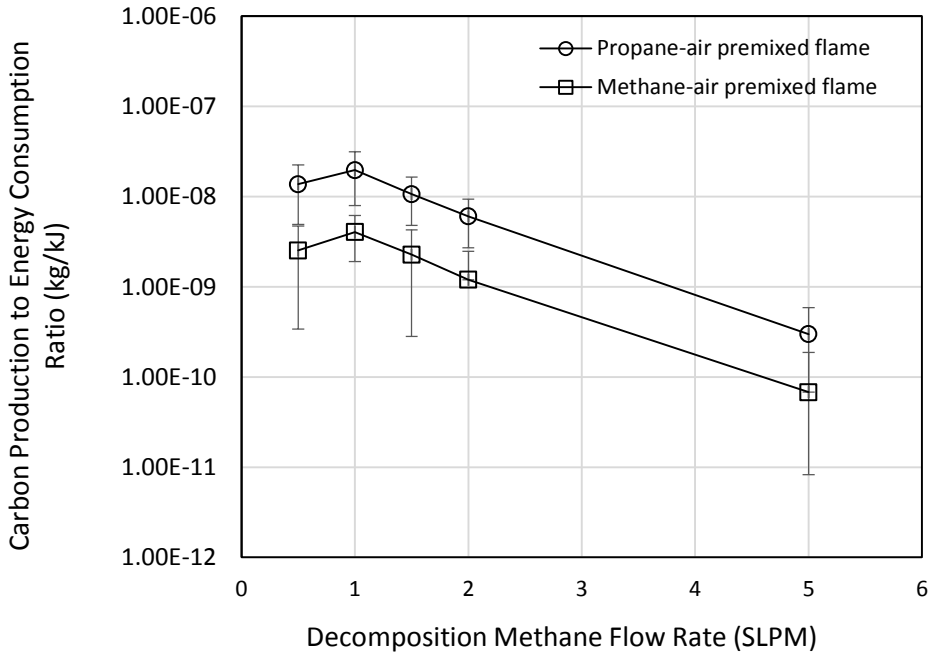

Figure 3.12. Carbon black production to energy consumption ratio for different flow rates of decomposition methane and heat sources. Error bars represent 95% confidence interval.

Chapter 4

Conclusions and Future Work

4.1 Conclusions

Direct thermal cracking of methane by injection into the products of premixed flames (propane- or methane-air) was tested in a medium-scale experimental setup. Methane thermally decomposed into H_2 and carbon black at a maximum temperature around 1150 °C, which was provided by the premixed flame. Efficiency of methane destruction and conversion to H_2 and carbon with a special attention to the carbon black properties were investigated under different flow rates of decomposing methane injection (0.5–5 SLPM). Carbon black particles were characterized by their size distribution, mass distribution, density, volatile content, morphology, and primary particle diameter.

Generally, TDM with lower flow rates of injection is more efficient in terms of methane destruction, H_2 and carbon black production. Properties of carbon black were more favorable in this configuration, for example, a wider range of aggregate size with larger CMD and higher concentration in number and mass can be obtained. Although denuded effective densities collapse to within ±20% of a general decreasing trend as a function of aggregate size, the size segregated volatile mass fractions seem to vary significantly between different flow rates of decomposing methane injection. Particles with higher fractions of volatile content appear to have relatively higher denuded effective density. This result was considered as the result of particle collapse (restructuring) into more dense structures due to excessive condensation of volatile materials on carbon black aggregates. Herein, TEM images confirmed the similarities between

the produced carbon black and the traditional engine soot such as the scaling of primary particle size with aggregate size.

TDM in products of premixed flames seems to be a relatively efficient method (and likely cost-effective) for H_2 production with a maximum efficiency of ~80%. However, the main drawback of this process is the poor efficiency of carbon black production (~1% in the best case) due to the high amount of CO formation by the gasification process, which consumes most of the solid carbon. This would ultimately make a mixture of H_2, CO, CO_2 (known as syngas) in TDM products, which is not suitable for H_2 extraction, but for use in the Fischer-Tropsch process or for use as an additional heat source.

4.2 Future Work

The results of TDM in the products of premixed flames are driven by three parameters (based on the present experimental setup): temperature gradient in the reactor, residence time, and mixing state of TDM products (H_2 and carbon black) with the combustion gas stream. It is assumed that variations in each parameter could result in different conversion efficiency of the process in terms of methane destruction efficiency, and H_2 and carbon black production efficiency, as well as different carbon black properties. In this regard, the following modifications/suggestions are recommended:

I. Modifying the reactor maintaining the current configuration

Residence time and temperature gradient in the current reactor are a function of reactor length and diameter, thermal conductivity of insulators, adiabatic flame temperature, total flow rate of combustion products, and decomposition methane flow rate. In order to

increase the process efficiency, a higher residence time with a gentle temperature gradient is required. This can be achieved through different modifications such as shortening the reactor length, decreasing the reactor diameter, using better insulators, changing the premixed fuel (*e.g.*, to acetylene) to get a higher flame temperature, using lower flow rates of decomposition methane, and changing the methane injection method (*e.g.*, to fuel spray injection) to get a higher mixing with combustion products.

II. Changing the reactor configuration

As discussed before, TDM while mixing the decomposition methane with the combustion products is the main reason of reduced carbon black production efficiency. As such, separating those flow streams prevents CO formation that consumes most of the produced carbon. For this purpose, methane can be directed through a highly conductive tube inside the reactor to decompose and the TDM products can be extracted directly without mixing with combustion products. Additional improvements can also be done to increase the residence time such as using helical tubes with different diameters.

Other than reactor modifications, particle measurement techniques can also be improved by adding high resolution TEM (HRTEM) to capture more features of the crystalline structure of carbon black, and Raman spectrometry to detect the carbonaceous structure and graphitization degree of carbon black.

Bibliography

Abánades, A., Ruiz, E. & Ferruelo, E.. . (2011). Experimental analysis of direct thermal methane cracking. *International Journal of Hydrogen Energy*, 36:12877–12886.

Abánades, A., Ruiz, E., Ferruelo, E.M., Hernández, F., Cabanillas, A., Martínez-Val, J.M., Rubio, J.A., López, C., Gavela, R., Barrera, G., Rubbia, C., Salmieri, D., Rodilla, E. & Gutiérrez, D. (2011). Experimental analysis of direct thermal methane cracking. *International Journal of Hydrogen Energy*, 36(20):12877–12886.

Abbas, H.F. & Wan Daud, W.M.A. (2010). Hydrogen production by methane decomposition: A review. *International Journal of Hydrogen Energy*, 35(3):1160–1190. Available at: http://dx.doi.org/10.1016/j.ijhydene.2009.11.036.

Adams, R. (2007). *Focus on Pigments*,

Ahmed, S., Aitani, A., Rahman, F., Al-Dawood, A. & Al-Muhaish, F. (2009). Decomposition of hydrocarbons to hydrogen and carbon. *Applied Catalysis A: General*, 359(1–2):1–24.

Ashik, U.P.M., Daud, W.M.A.W. & Abbas, H.F. (2015). Production of greenhouse gas free hydrogen by thermocatalytic decomposition of methane – A review. *Renewable and Sustainable Energy Reviews*, 44:221–256.

Ashik, U.P.M., Daud, W.M.A.W. & Hayashi, J. (2017). A review on methane transformation to hydrogen and nanocarbon : Relevance of catalyst characteristics and experimental parameters on yield. *Renewable and Sustainable Energy Reviews*, 76(January):743–767.

Auchter, J. (2005). *Chemical Economics Handbook: Carbon Black*,

Balat, M. & Balat, M. (2009). Political , economic and environmental impacts of biomass-based hydrogen. *International Journal of Hydrogen Energy*, 34(9):3589–3603.

Black, S.A., Pearls, B. & Spectra, R. (2010). *Carbon Black*,

Dastanpour, R., Boone, J.M. & Rogak, S.N. (2016). Automated primary particle sizing of nanoparticle aggregates by TEM image analysis. *Powder Technology*, 295:218–224. Available at: http://dx.doi.org/10.1016/j.powtec.2016.03.027.

Dastanpour, R. & Rogak, S.N. (2014). Observations of a correlation between primary particle and aggregate size for soot particles. *Aerosol Science and Technology*, 48(10):1043–1049.

Dastanpour, R., Rogak, S.N., Graves, B., Olfert, J., Eggersdorfer, M.L. & Boies, A.M. (2016). Improved sizing of soot primary particles using mass-mobility measurements. *Aerosol Science and Technology*, 50(2):101–109.

Dickau, M., Olfert, J., Stettler, M.E.J., Boies, A., Momenimovahed, A., Thomson, K., Smallwood, G. & Johnson, M. (2016). Methodology for quantifying the volatile mixing state of an aerosol. *Aerosol Science and Technology*, 50(8):759–772. Available at: http://dx.doi.org/10.1080/02786826.2016.1185509.

Eggersdorfer, M.L., Gröhn, A.J., Sorensen, C.M., McMurry, P.H. & Pratsinis, S.E. (2012). Mass-mobility characterization of flame-made ZrO 2 aerosols: Primary particle diameter and extent of aggregation. *Journal of Colloid and Interface Science*, 387(1):12–23. Available at: http://dx.doi.org/10.1016/j.jcis.2012.07.078.

Falahati, F. (2018). *Experimental study of methane decarbonization to produce hydrogen using a laminar premixed flame*.

Fulcheri, L. & Schwob, Y. (1995). From methane to hydrogen, carbon black and water. *International Journal of Hydrogen Energy*, 20:197–202.

Gaddam, C.K., Huang, C.H. & Vander Wal, R.L. (2016). Quantification of nano-scale carbon structure by HRTEM and lattice fringe analysis. *Pattern Recognition Letters*, 76:90–97.

Gautier, M., Rohani, V., Fulcheri, L. & Trelles, J.P. (2016). Influence of temperature and pressure on carbon black size distribution during allothermal cracking of methane. *Aerosol Science and Technology*, 50(1):26–40. Available at: http://dx.doi.org/10.1080/02786826.2015.1123214.

Ghazi, R., Tjong, H., Soewono, A., Rogak, S.N. & Olfert, J.S. (2013). Mass, mobility, volatility, and morphology of soot particles generated by a mckenna and inverted burner. *Aerosol Science and Technology*, 47(4):395–405.

Graves, B. (2015). *Characterization of Particulate Matter Morphology and Volatility for Two Direct-Injection Engines*.

Graves, B., Olfert, J., Patychuk, B., Dastanpour, R. & Rogak, S. (2015). Characterization of Particulate Matter Morphology and Volatility from a Compression-Ignition Natural-Gas Direct-Injection Engine. *Aerosol Science and Technology*, 49(8):589–598.

Graves, B.M., Koch, C.R. & Olfert, J.S. (2017). Morphology and volatility of particulate matter emitted from a gasoline direct injection engine fuelled on gasoline and ethanol blends. *Journal of Aerosol Science*, 105(February 2016):166–178.

Heitor, M. V. & Moreira, A.L.N. (1993). Thermocouples and sample probes for combustion studies. *Progress in Energy and Combustion Science*, 19(3):259–278.

International Carbon Black Association (2016). Carbon Black User ' s Guide. *Carbon Black User's Guide*:36. Available at: http://www.carbon-black.org/images/docs/2016-ICBA-Carbon-Black-User-Guide.pdf.

International Carbon Black Association (2006). What is Carbon Black? *Www.Carbonblack.Org*. Available at: http://www.carbonblack.jp/en/cb/index.html%5Cnhttp://www.carbon-black.org/what_is.html.

Kasper, M., Sattler, K., Siegmann, K., Matter, U. & Siegmann, H.C. (1999). The influence of fuel addititive on the formation of carbon during combustion. *Journal of Aerosol Science*, 30(2):217–225.

Keipi, T., Tolvanen, K.E.S., Tolvanen, H. & Konttinen, J. (2016). Thermo-catalytic

decomposition of methane: The effect of reaction parameters on process design and the utilization possibilities of the produced carbon. *Energy Conversion and Management*, 126:923–934. Available at: http://dx.doi.org/10.1016/j.enconman.2016.08.060.

Kim, K.S., Seo, J.H., Nam, J.S., Ju, W.T. & Hong, S.H. (2005). Production of hydrogen and carbon black by methane decomposition using DC-RF hybrid thermal plasmas. *IEEE Transactions on Plasma Science*, 33(2 II):813–823.

Konieczny, A., Mondal, K., Wiltowski, T. & Dydo, P. (2008). Catalyst development for thermocatalytic decomposition of methane to hydrogen. *International Journal of Hydrogen Energy*, 33:264–272.

Leduc, P., Dubar, B., Ranini, A. & Monnier, G. (2008). Downsizing of Gasoline Engine : an Efficient Way to Reduce CO 2 Emissions. *Oil and Gas Science and Technology*, 58(1):115–127.

Long, C.M., Nascarella, M.A. & Valberg, P.A. (2013). Carbon black vs. black carbon and other airborne materials containing elemental carbon: Physical and chemical distinctions. *Environmental Pollution*, 181:271–286. Available at: http://dx.doi.org/10.1016/j.envpol.2013.06.009.

Maricq, M.M. & Xu, N. (2004). The effective density and fractal dimension of soot particles from premixed flames and motor vehicle exhaust. *Journal of Aerosol Science*, 35(10):1251–1274.

Miller, A., Frey, G., King, G. & Sunderman, C. (2010). A handheld electrostatic precipitator for sampling airborne particles and nanoparticles. *Aerosol Science and Technology*, 44(6):417–427.

Momenimovahed, A. & Olfert, J.S. (2015). Effective Density and Volatility of Particles Emitted from Gasoline Direct Injection Vehicles and Implications for Particle Mass Measurement. *Aerosol Science and Technology*, 49(11):1051–1062.

Momirlan, M. & Veziroglu, T.N. (2002). Current status of hydrogen energy. *Renewable and Sustainable Energy Reviews*, 6:141–179.

Muradov, N.Z. & Veziroä, T.N. (2005). From hydrocarbon to hydrogen – carbon to hydrogen economy. *International Journal of Hydrogen Energy*, 30:225–237.

Olfert, J.S., Dickau, M., Momenimovahed, A., Saffaripour, M., Thomson, K., Smallwood, G., Stettler, M.E.J., Boies, A., Sevcenco, Y., Crayford, A. & Johnson, M. (2017). Effective density and volatility of particles sampled from a helicopter gas turbine engine. *Aerosol Science and Technology*, 51(6):704–714.

Olfert, J.S., Symonds, J.P.R. & Collings, N. (2007). The effective density and fractal dimension of particles emitted from a light-duty diesel vehicle with a diesel oxidation catalyst. *Journal of Aerosol Science*, 38(1):69–82.

Palotás, a B., Rainey, L.C., Feldermann, C.J., Sarofim, a F. & Vander Sande, J.B. (1996). Soot morphology: an application of image analysis in high-resolution transmission electron

microscopy. *Microscopy research and technique*, 33(3):266–278.

Park, K., Cao, F., Kittelson, D.B. & McMurry, P.H. (2003). Relationship between particle mass and mobility for diesel exhaust particles. *Environmental Science and Technology*, 37(3):577–583.

Parkinson, B., Tabatabaei, M., Upham, D.C., Ballinger, B., Greig, C., Smart, S. & McFarland, E. (2018). Hydrogen production using methane: Techno-economics of decarbonizing fuels and chemicals. *International Journal of Hydrogen Energy*, 43(5):2540–2555. Available at: https://doi.org/10.1016/j.ijhydene.2017.12.081.

Paxman, D., Trottier, S., Flynn, M.R., Kostiuk, L. & Secanell, M. (2017). Experimental and numerical analysis of a methane thermal decomposition reactor. *International Journal of Hydrogen Energy*, 42:25166–25184.

Paxman, D., Trottier, S., Flynn, M.R., Kostiuk, L. & Secanell, M. (2017). Experimental and numerical analysis of a methane thermal decomposition reactor. *International Journal of Hydrogen Energy*, 42(40):25166–25184. Available at: https://doi.org/10.1016/j.ijhydene.2017.08.134.

Quiros, D.C., Hu, S., Hu, S., Lee, E.S., Sardar, S., Wang, X., Olfert, J.S., Jung, H.S., Zhu, Y. & Huai, T. (2015). Particle effective density and mass during steady-state operation of GDI, PFI, and diesel passenger cars. *Journal of Aerosol Science*, 83:39–54. Available at: http://dx.doi.org/10.1016/j.jaerosci.2014.12.004.

Ristimäki, J., Vaaraslahti, K., Lappi, M. & Keskinen, J. (2007). Hydrocarbon condensation in heavy-duty diesel exhaust. *Environmental Science and Technology*, 41(18):6397–6402.

Rodat, S., Abanades, S., Coulié, J. & Flamant, G. (2009). Kinetic modelling of methane decomposition in a tubular solar reactor. *Chemical Engineering Journal*, 146(1):120–127.

Rodat, S., Abanades, S., Sans, J. & Flamant, G. (2009). Hydrogen production from solar thermal dissociation of natural gas: development of a 10 kW solar chemical reactor prototype. *Solar Energy*, 83:1599–1610.

Rogak, S.N., Flagan, R.C. & Nguyen, H. V (1993). The Mobility and Structure of Aerosol Agglomerates. *Aerosol Science and Technology*, 18(1):25–47.

Sakurai, H., Park, K., McMurry, P.H., Zarling, D.D., Kittelson, D.B. & Ziemann, P.J. (2003). Size-Dependent Mixing Characteristics of Volatile and Nonvolatile Components in Diesel Exhaust Aerosols. *Environmental Science and Technology*, 37(24):5487–5495.

Serrano, D.P., Botas, J.A. & Guil-Lopez, R. (2009). H2production from methane pyrolysis over commercial carbon catalysts: Kinetic and deactivation study. *International Journal of Hydrogen Energy*, 34(10):4488–4494. Available at: http://dx.doi.org/10.1016/j.ijhydene.2008.07.079.

Shaddix, C.R. (1999). Correcting thermocouple measurements for radiation loss: a critical review. In *Proceedings of the 33rd National Heat Transfer Conference*. Albuquerque, NM.

Steinberg, M. (1999). Fossil fuel decarbonization technology for mitigating global warming. *International Journal of Hydrogen Energy*, 24:771–777.

Valle, F., Fierro, J.L.G., Navarro, R.M. & Sa, M.C. (2009). Hydrogen production from renewable sources : biomass and photocatalytic opportunities. *Energy and Environmental Science*, 2:35–54.

Wang, M.-J., Gray, C.A., Reznek, S.A., Mahmud, K. & Kutsovsky, Y. (2011). Carbon Black. *SpringerReference*, 4:761–803. Available at: http://www.springerreference.com/index/doi/10.1007/SpringerReference_208034.

Weger, L., Abánades, A. & Butler, T. (2017). Methane cracking as a bridge technology to the hydrogen economy. *International Journal of Hydrogen Energy*, 42(1):720–731.

Whitaker, S. (1972). Forced convection heat transfer correlations for flow in pipes, past flat plates, single cylinders, single spheres, and for flow in packed beds and tube bundles. *AIChE Journal*, 18(2):361–371. Available at: https://doi.org/10.1002/aic.690180219.

WHO (1984). Carbon Black, Titanium Dioxide, and Talc. *IARC Monographs on the Evaluation of Carcinogenic Risks to Humans*, 93:43–190.

Appendix A Uncertainty Analysis

In this section, the uncertainty analysis of number-size distribution, count median diameter, mass-size distribution, total number and mass concentrations, size segregated volatile mass fraction, aggregate area equivalent diameter, average primary particle diameter in individual aggregates, methane destruction efficiency, and hydrogen and carbon black production efficiencies are presented in detail.

Generally, errors in experimental measurements can be divided into two types:

I. Bias or Systematic error (B_x) — The offset error that cannot be evaluated from the data and remains with repeated measurements. This type of error can be estimated by manufacturers' specifications, independent calibration or other sources.

II. Precision, Random or Stochastic error (P_x) — The error in recording repeatable data that can be estimated by probability and statistics concepts.

Using Student *t*-distribution and with confidence interval of *C*%, the precision error can be estimated as

$$P_x = t_{\alpha/2,\nu} \frac{S_x}{\sqrt{n}}, \tag{A.1}$$

where n is the sample size (or number of measurements taken), α is equal to one minus the confidence interval $(1 - C)$, ν is the degrees of freedom $(n - 1)$, and S_x is the standard deviation of measurements and can be calculated from the following equation:

$$S_x = \sqrt{\frac{\sum(x_i - \bar{x})^2}{n-1}} \tag{A.2}$$

For very small sample sizes that only one or two measurements are possible ($n < 3$), the precision error for 95% confidence interval is often estimated as

$$P_x = 2\sigma, \tag{A.3}$$

where σ is the standard deviation of many repeated measurements at some other time.

The combined uncertainty of bias and precision errors at the same confidence interval (usually 95%) is the total uncertainty (U_x) of measurement, and can be calculated as

$$U_x = \Delta x = \sqrt{\Sigma B_x^2 + P_x^2}. \tag{A.4}$$

If y is a quantity determined by measurement of N independent variables with the same confidence interval (*i.e.*, $y = f(x_1, x_2, \dots, x_i, \dots, x_N)$), the uncertainty of calculating y can be approximated by the Gaussian error propagation rule,

$$\Delta x_y = \sqrt{(\frac{\partial f}{\partial x_1}\Delta x_1)^2 + (\frac{\partial f}{\partial x_2}\Delta x_2)^2 + \cdots + (\frac{\partial f}{\partial x_i}\Delta x_i)^2 + \cdots + (\frac{\partial f}{\partial x_N}\Delta x_N)^2} \qquad 1 \le i \le N, \tag{A.5}$$

where Δx_i is the total uncertainty of variable i.

A.1 Uncertainty in Number-size Distribution and Total Number Concentration

Based on the Gaussian error propagation rule, the uncertainty in $\frac{\mathrm{d}N}{\mathrm{dlog}(d_\mathrm{m})}$ for the size bin of j in the undiluted number-size distribution can be estimated by

$$\frac{\Delta N_{j,\mathrm{undiluted}}}{N_{j,\mathrm{undiluted}}} = \sqrt{(\frac{\Delta DR}{DR})^2 + (\frac{\Delta N_{j,\mathrm{diluted}}}{N_{j,\mathrm{diluted}}})^2}, \tag{A.6}$$

where N represents $\frac{\mathrm{d}N}{\mathrm{dlog}(d\mathrm{m})}$ and DR is the dilution ratio. Equation (A.6) can be also used to obtain the uncertainty in undiluted total number concentration of particles when j represents the full range of particle sizes (15–700 nm) and N being the actual total number concentration.

The dilution ratio is calculated by

$$DR = \frac{[\mathrm{CO_2}]_\mathrm{undiluted}}{[\mathrm{CO_2}]_\mathrm{diluted}}, \tag{A.7}$$

so the uncertainty in DR will be

$$\frac{\Delta DR}{DR} = \sqrt{(\frac{\Delta[\mathrm{CO_2}]_\mathrm{undiluted}}{[\mathrm{CO_2}]_\mathrm{undiluted}})^2 + (\frac{\Delta[\mathrm{CO_2}]_\mathrm{diluted}}{[\mathrm{CO_2}]_\mathrm{diluted}})^2}. \tag{A.8}$$

The uncertainty in $[\mathrm{CO_2}]_\mathrm{undiluted}$ or $[\mathrm{CO_2}]_\mathrm{diluted}$ can be determined by

$$\frac{\Delta[\mathrm{CO_2}]}{[\mathrm{CO_2}]} = \sqrt{(\frac{B_{[\mathrm{CO_2}]}}{[\mathrm{CO_2}]})^2 + (\frac{P_{[\mathrm{CO_2}]}}{[\mathrm{CO_2}]})^2}, \tag{A.9}$$

where $B_{[\mathrm{CO_2}]_\mathrm{undiluted}}$ and $\frac{B_{[\mathrm{CO_2}]_\mathrm{diluted}}}{[\mathrm{CO_2}]_\mathrm{diluted}}$ are 0.01 mole% based on the gas chromatograph (GC) calibration table and 1% based on the CO_2 analyzer specification, respectively. Moreover,

$P_{[CO_2]_{undiluted}}$ or $P_{[CO_2]_{diluted}}$ can be estimated by equations (A.1) and (A.2) for repeated measurements of CO_2 concentration in undiluted and diluted conditions, respectively.

Furthermore, in each size bin of particle size distribution (j) or in the full-size range of particles (j=total), the uncertainty in $N_{j,\text{diluted}}$ can be estimated as

$$\frac{\Delta N_{j,\text{diluted}}}{N_{j,\text{diluted}}} = \sqrt{\left(\frac{B_{N_{i,\text{diluted}}}}{N_{i,\text{diluted}}}\right)^2 + \left(\frac{P_{N_{i,\text{diluted}}}}{N_{i,\text{diluted}}}\right)^2}, \quad \text{(A.10)}$$

where $\frac{B_{N_{j,\text{diluted}}}}{N_{j,\text{diluted}}}$ is 10% based on the instrument specification (CPC; TSI Inc., Model 3776), and $P_{N_{j,\text{diluted}}}$ can be estimated using equations (A.1) and (A.2) for repeated measurements of particle size distribution.

Tables A.1 and A.2 demonstrate the average value and total uncertainty in $N_{\text{total,undiluted}}$ estimated for decomposition of different flow rates of methane in products of propane-air or methane-air premixed flame, respectively. The uncertainty in undiluted number-size distribution of particles from different reaction conditions are shown in Figures A.1 and A.2.

Table A.1. Average value and uncertainty in total number concentration of undiluted particles using propane-air premixed flame as the heat source.

Decomposition methane flow rate (SLPM)	Mean total number concentration (cm^{-3})	Number of measurements	Average uncertainty in dilution ratio	Average uncertainty in diluted number concentration	Average total uncertainty
0.5	1.69×10^{8}	5	2%	11%	11%
1.0	6.18×10^{8}	5	2%	16%	17%
1.5	8.82×10^{8}	5	2%	13%	13%
2.0	6.26×10^{8}	5	4%	11%	11%
5.0	5.64×10^{7}	5	3%	18%	19%

Table A.2. Average value and uncertainty in total number concentration of undiluted particles using methane-air premixed flame as the heat source.

Decomposition methane flow rate (SLPM)	Mean total number concentration (cm^{-3})	Number of measurements	Average uncertainty in dilution ratio	Average uncertainty in diluted number concentration	Average total uncertainty
0.5	1.27×10^{8}	5	2%	11%	11%
1.0	7.89×10^{8}	5	1%	12%	12%
1.5	2.58×10^{8}	5	2 %	10%	10%
2.0	8.26×10^{7}	5	3%	10%	11%
5.0	3.04×10^{5}	5	3%	64%	64%

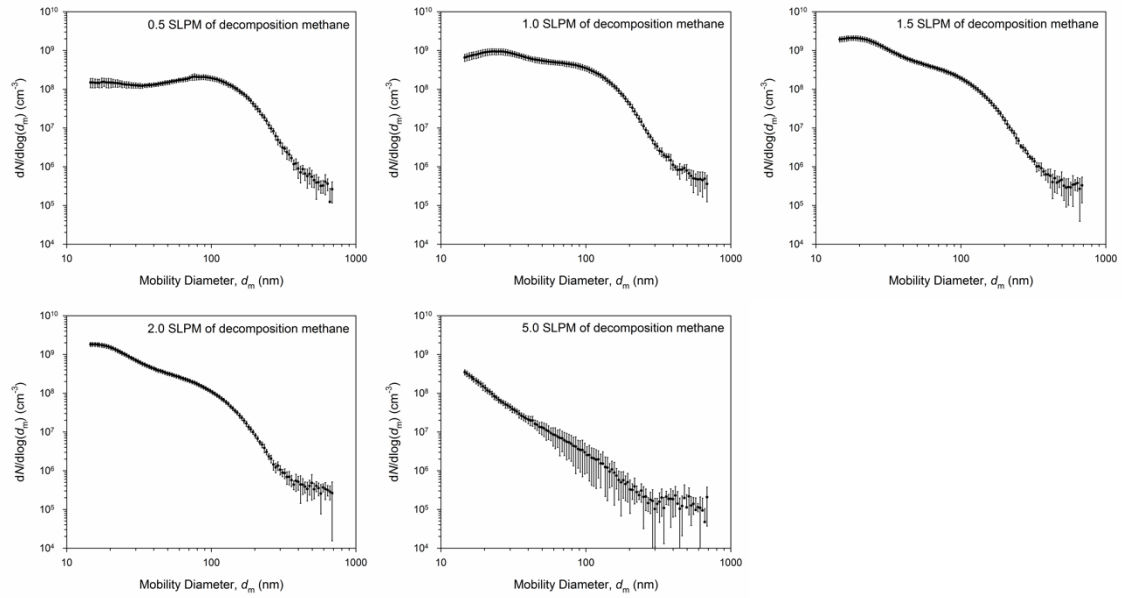

Figure A.1. Average value and uncertainty in undiluted number-size distribution of particles when using propane-air premixed flame as the heat source.

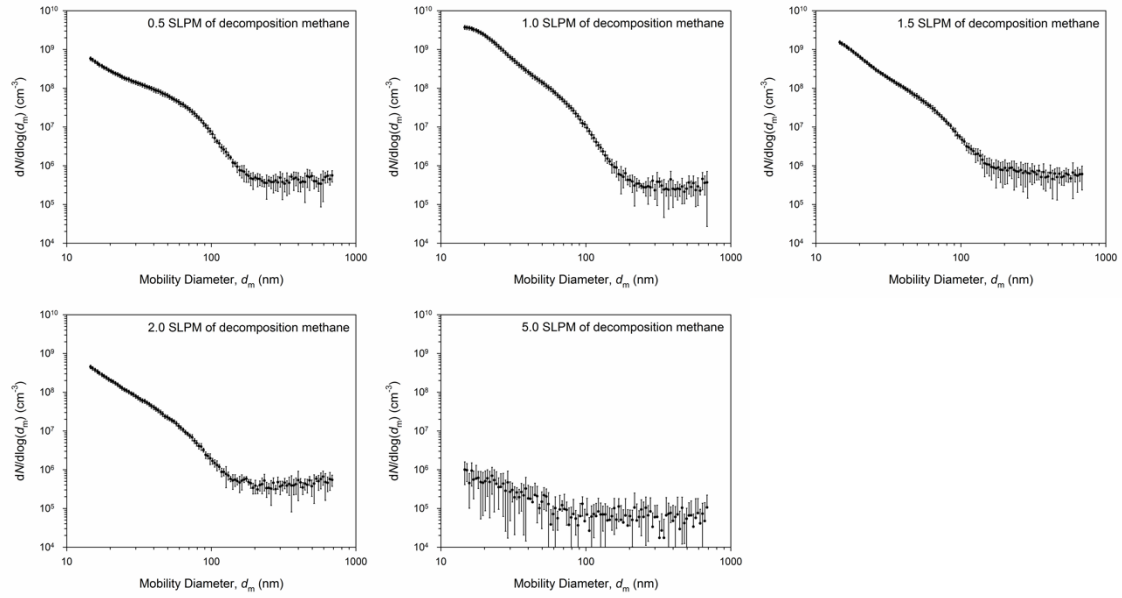

Figure A.2. Average value and uncertainty in undiluted number-size distribution of particles when using methane-air premixed flame as the heat source.

A.2 Uncertainty in Count Median Diameter

Total uncertainty in count median diameter (CMD) of the particle size distribution is a combination of bias uncertainty caused by the instrument (DMA; TSI Inc., Model 3080) and precision uncertainty from repeated measurements. Thus, the total uncertainty in CMD can be estimated as

$$\frac{\Delta \mathrm{CMD}}{\mathrm{CMD}} = \sqrt{\left(\frac{B_{\mathrm{CMD}}}{\mathrm{CMD}}\right)^2 + \left(\frac{P_{\mathrm{CMD}}}{\mathrm{CMD}}\right)^2}, \tag{A.11}$$

where $\frac{B_{\mathrm{CMD}}}{\mathrm{CMD}}$ is 3% for 95% confidence interval and P_{CMD} can be estimated by equations (A.1) and (A.2) for repeated measurements of particle size distribution.

Tables A.3 and A.4 demonstrate the average value and the total uncertainty in CMD, estimated for decomposition of different flow rates of methane in products of propane-air or methane-air premixed flame, respectively.

Table A.3. Average value and uncertainty in count median diameter when using propane-air premixed flame as the heat source.

Decomposition methane flow rate (SLPM)	Mean count median diameter (nm)	Number of measurements	Bias uncertainty	Precision uncertainty	Total uncertainty
0.5	58	5	3%	10%	10%
1.0	33	5	3%	2%	4%
1.5	24	5	3%	1%	3%
2.0	22	5	3%	1%	3%
5.0	18	5	3%	1%	3%

Table A.4. Average value and uncertainty in count median diameter when using methane-air premixed flame as the heat source.

Decomposition methane flow rate (SLPM)	Mean count median diameter (nm)	Number of measurements	Bias uncertainty	Precision uncertainty	Total uncertainty
0.5	21	5	3%	1%	3 %
1.0	19	5	3%	1%	3%
1.5	18	5	3%	<1%	3%
2.0	19	5	3%	<1%	3%
5.0*	-	5	-	-	-

* Values for this flow rate are not realistic due to instability of the corresponding particles size distribution and hence are not reported.

A.3 Uncertainty in Mass-size Distribution and Total Mass Concentration

As shown previously, each size bin of the mass distribution is obtained from

$$M_{j,\text{undiluted}} = \frac{\pi}{6} \left(\rho_{\text{eff,undenuded}}\right)_j \, {d_{\text{m},j}}^3 \, N_{j,\text{undiluted}}, \tag{A.12}$$

where M represents $\frac{\mathrm{d}M}{\mathrm{dlog}(d\mathrm{m})}$, N represents $\frac{\mathrm{d}N}{\mathrm{dlog}(d\mathrm{m})}$, and $\left(\rho_{\text{eff,undenuded}}\right)_j$ is the undenuded effective density of particles with the mobility diameter of j and can be estimated by using the prefactor (k) and mass-mobility exponent (D_m) of the corresponding general trend in Figure 3.6, $\left(\rho_{\text{eff,undenuded}}\right)_j = k \, {d_{\text{m},j}}^{D_\mathrm{m}-3}$. The error propagation in the calculation of size bin of j in the mass distribution can be defined as

$$\frac{\Delta M_{j,\text{undiluted}}}{M_{j,\text{undiluted}}} = \sqrt{\left(\frac{\Delta\left(\rho_{\text{eff,undenuded}}\right)_j}{\left(\rho_{\text{eff,undenuded}}\right)_j}\right)^2 + 9\left(\frac{\Delta d_{\text{m},j}}{d_{\text{m},j}}\right)^2 + \left(\frac{\Delta N_{j,\text{diluted}}}{N_{j,\text{diluted}}}\right)^2}, \tag{A.13}$$

where $\frac{\Delta d_{\mathrm{m},j}}{d_{\mathrm{m},j}}$ is 3% based on the instrument specification (DMA; TSI Inc., Model 3081), $\frac{\Delta N_{j,\mathrm{diluted}}}{N_{j,\mathrm{diluted}}}$ can be obtained from the previous section, and $\frac{\Delta(\rho_{\mathrm{eff,undenuded}})_j}{(\rho_{\mathrm{eff,undenuded}})_j}$ is calculated for 95% confidence interval as following:

$$\frac{\Delta(\rho_{\mathrm{eff,undenuded}})_j}{(\rho_{\mathrm{eff,undenuded}})_j} = \frac{1.96\,\sigma_{est}}{\rho_{\mathrm{est},j}}, \tag{A.14}$$

with ρ_{est} being the estimated undenuded effective density for the mobility diameter of j by the general trend in Figure 3.6, and σ_{est} being the standard error of estimate for the fit,

$$\sigma_{est} = \sqrt{\frac{(\rho_j - \rho_{\mathrm{est},j})^2}{n-2}}, \tag{A.15}$$

where ρ_j is the real value of undenuded effective density for the mobility diameter of j.

Total mass concentration of particles is

$$M_{\mathrm{total,undiluted}} = \sum_j M_{j,\mathrm{undiluted}}\,\mathrm{dlog}(d_{\mathrm{m}})_j. \tag{A.16}$$

Hence the uncertainty in the total mass concentration is the sum of errors in each size bin of mass distribution;

$$\Delta M_{\mathrm{total,undiluted}} = \sum_j \Delta M_{j,\mathrm{undiluted}}\,\mathrm{dlog}(d_{\mathrm{m}})_j, \tag{A.17}$$

where

$$\mathrm{dlog}(d_{\mathrm{m}})_j = \log\left(\frac{(\mathrm{d_m})_{j+1}}{(\mathrm{d_m})_j}\right). \tag{A.18}$$

Tables A.5 and A.6 demonstrate the average value and total uncertainty in $M_{\text{total,undiluted}}$ estimated for decomposition of different flow rates of methane in products of propane-air or methane-air premixed flame, respectively. Total uncertainty in the undiluted mass-size distribution of particles from different reaction conditions are shown in Figures A.3 and A.4.

Table A.5. Average value and uncertainty in total mass concentration of undiluted particles when using propane-air premixed flame as the heat source.

Decomposition methane flow rate (SLPM)	Mean total mass concentration (mg m^{-3})	Standard error of estimate, σ_{est} (mg m^{-3})	Uncertainty in mobility diameter	Average total uncertainty
0.5	55.2	184	3%	64%
1.0	88.1	184	3%	60%
1.5	52.4	184	3%	55%
2.0	31.8	184	3%	55%
5.0	2.2	184	3%	97%

Table A.6. Average value and uncertainty in total mass concentration of undiluted particles when using methane-air premixed flame as the heat source.

Decomposition methane flow rate (SLPM)	Mean total mass concentration (mg m^{-3})	Standard error of estimate, σ_{est} (mg m^{-3})	Uncertainty in mobility diameter	Average total uncertainty
0.5	5.6	166	3%	87%
1.0	10.7	166	3%	53%
1.5	7.1	166	3%	88%
2.0	4.2	166	3%	106%
5.0	0.4	166	3%	175%

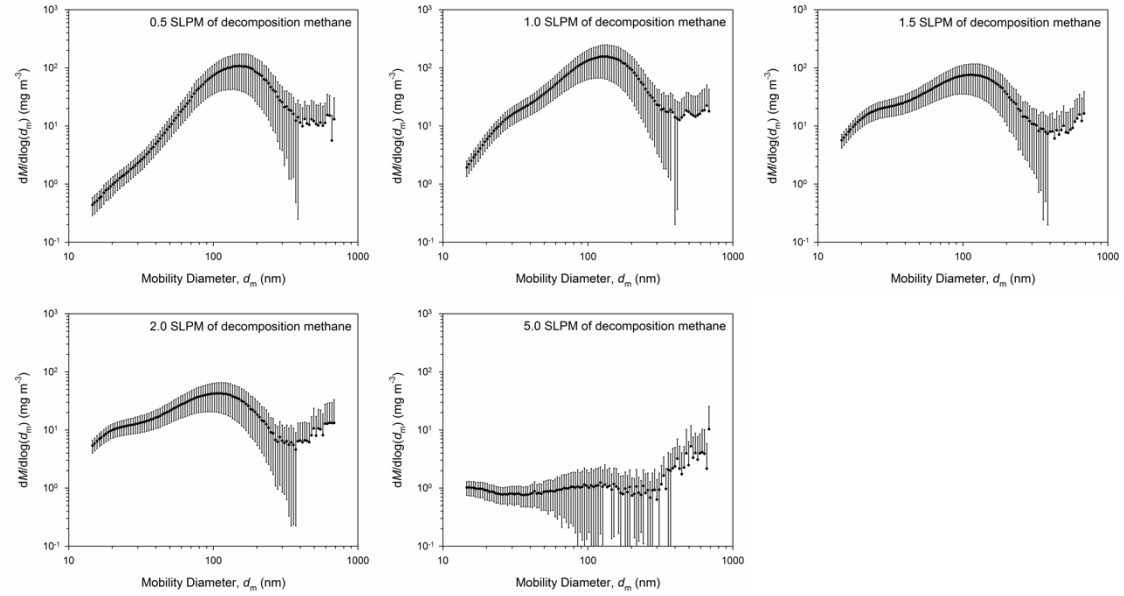

Figure A.3.. Average value and uncertainty in the undiluted mass-size distribution when using propane-air premixed flame as the heat source.

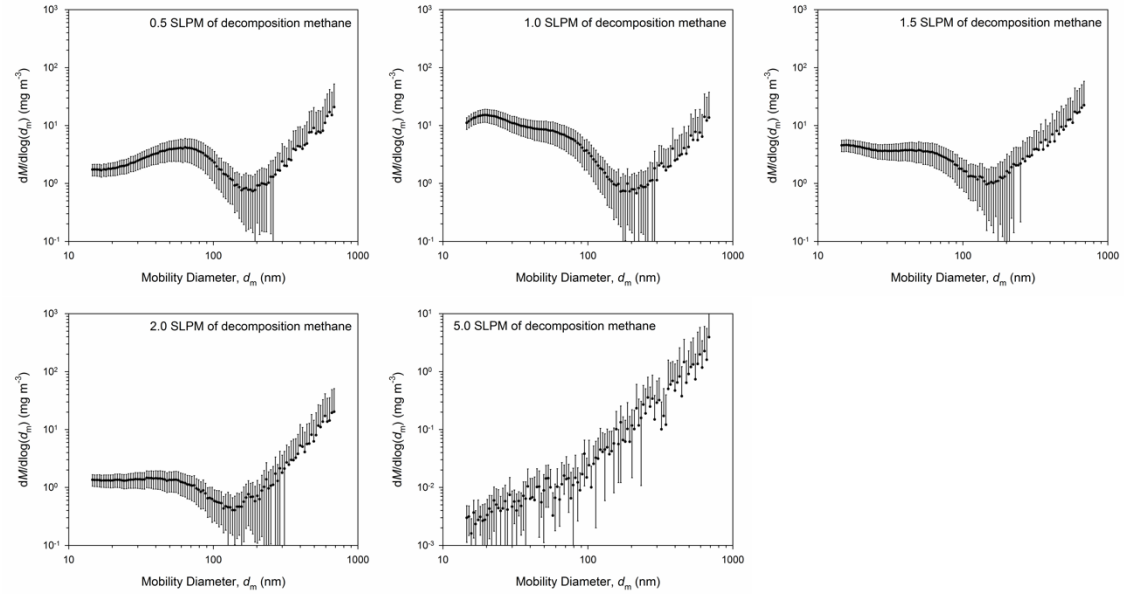

Figure A.4.. Average value and uncertainty in the undiluted mass-size distribution when using methane-air premixed flame as the heat source.

A.4 Uncertainty in Volatile Mass Fraction

The volatile mass fraction in a particle is calculated by

$$f_{\mathrm{vm}} = 1 - \frac{m_{\mathrm{D}}}{m_{\mathrm{U}}}, \tag{A.19}$$

where m_{D} and m_{U} are the mass of denuded and undenuded particle with the same undenuded mobility diameter of d_{m}, respectively. Since those masses are measured consecutively by the same instrument (CPMA; Cambustion), the bias uncertainty would be eliminated by taking the ratio of masses. Hence, only the precision error is contributing to the total uncertainty of volatile mass fraction. Depending on the number of measurements, two approaches were taken for calculation of the total uncertainty:

I. Using equations (A.1) and (A.2) to calculate the precision uncertainty in the average value of volatile mass fraction when having multiple measurements ($n > 1$),

II. Using the principle of error propagation when having only one measurement ($n = 1$).

In the latter case, the uncertainty of the volatile mass fraction is calculated by

$$\Delta f_{\mathrm{vm}} = (1 - f_{\mathrm{vm}})\sqrt{\left(\frac{P_{m_{\mathrm{D}}}}{m_{\mathrm{D}}}\right)^2 + \left(\frac{P_{m_{\mathrm{U}}}}{m_{\mathrm{U}}}\right)^2}, \tag{A.20}$$

where the precision uncertainty in the mass measurement of denuded or undenuded particles ($\frac{P_m}{m}$) can be calculated using equation (A.3) and 2.4% as the relative standard deviation ($\frac{\sigma}{m}$) for repeated measurements (*i.e.*, $\frac{P_m}{m} = 2\left(\frac{\sigma}{m}\right) = 0.048$).

Tables A.7 and A.8 show the average value and uncertainty in volatile mass fraction of particles from decomposition of different flow rates of methane in products of propane-air or methane-air premixed flame, respectively.

Table A.7. Average value and uncertainty in volatile mass fraction of particles when using propane-air premixed flame as the heat source.

Decomposition methane flow rate (SLPM)	Mobility Diameter (nm)	Mean volatile mass fraction	Number of measurements	Total uncertainty
0.5	15	0.12	1	0.06
	23	0.15	1	0.06
	36	0.18	1	0.06
	55	0.16	1	0.06
	85	0.12	1	0.06
1.0	15	1	3	0.00
	23	0.54	3	0.08
	36	0.53	3	0.05
	55	0.45	3	0.01
	85	0.40	3	0.02
5.0	15	0.29	1	0.05
	23	0.25	1	0.05
	36	0.20	1	0.05
	55	0.18	1	0.06
	85	0.16	1	0.06

Table A.8. Average value and uncertainty in volatile mass fraction of particles when using methane-air premixed flame as the heat source.

Decomposition methane flow rate (SLPM)	Mobility Diameter (nm)	Mean volatile mass fraction	Number of measurements	Total uncertainty
0.5	15	0.15	1	0.06
	23	0.10	1	0.06
	36	0.12	1	0.06
	55	0.09	1	0.06
	85	0.09	1	0.06
1.0	15	0.53	3	0.20
	23	0.49	3	0.21
	36	0.43	3	0.10
	55	0.37	3	0.07
	85	0.32	3	0.07
5.0	15	0.13	1	0.06
	23	0.14	1	0.06
	36	0.19	1	0.05
	55	0.16	1	0.06
	85	0.11	1	0.06

A.5 Uncertainty in TEM Results

Total uncertainty in the TEM results including aggregate area equivalent diameter and average size of primary particles in individual aggregates can be calculated based on the precision uncertainty, using equations (A.1) and (A.2). Tables A.9 and A.10 show the average value and uncertainty in the TEM results for decomposition of different flow rates of methane in products of propane-air or methane-air premixed flame, respectively.

Table A.9. Average value and uncertainty in aggregate projected area equivalent diameter and average size of primary particles in individual aggregates when using propane-air premixed flame as the heat source.

Decomposition methane flow rate (SLPM)	Number of TEM images	Mean aggregate area equivalent diameter (nm)	Total uncertainty in average aggregate size (nm)	Mean average diameter of primary particles in individual aggregates (nm)	Total uncertainty in average size of primary particles (nm)
0.5	56	113	17	14	2
1.0	46	150	21	20	2
1.5	40	168	23	24	3
2.0	48	159	19	21	3
5.0	32	125	15	27	3

Table A.10. Average value and uncertainty in aggregate projected area equivalent diameter and average size of primary particles in individual aggregates when using methane-air premixed flame as the heat source.

Decomposition methane flow rate (SLPM)	Number of TEM images	Mean aggregate area equivalent diameter (nm)	Total uncertainty in average aggregate size (nm)	Mean average diameter of primary particles in individual aggregates (nm)	Total uncertainty in average size of primary particles (nm)
0.5	32	67	14	12	3
1.0	32	90	15	17	2
1.5	32	86	15	16	2
2.0	32	77	12	14	2
5.0	16	33	14	9	2

A.6 Uncertainty in Methane Destruction Efficiency

As shown previously, the destruction efficiency of methane can be calculated from

$$\eta_{\mathrm{CH_4,\,des}} = 1 - \frac{\dot{m}_{\mathrm{CH_4,out}}}{\dot{m}_{\mathrm{CH_4,in}}}, \tag{A.21}$$

where $\dot{m}_{\mathrm{CH_4,in}}$ is the mass flow rate of decomposition methane and can be calculated by

$$\dot{m}_{\mathrm{CH_4,in}} = \dot{V}_{\mathrm{CH_4,in}}\,\rho_{\mathrm{CH_4}}, \tag{A.22}$$

and $\dot{m}_{\mathrm{CH_4,out}}$ is the mass flow rate of undecomposed methane in the exhaust and is determined by

$$\dot{m}_{\mathrm{CH_4,out}} = \dot{n}_{\mathrm{CH_4,out}}\,\mathcal{M}_{\mathrm{CH_4}} = y_{\mathrm{CH_4,GC}}\,\dot{n}_{\mathrm{total,out}}\,\mathcal{M}_{\mathrm{CH_4}} \tag{A.23}$$

$$= y_{\mathrm{CH_4,GC}}\,\frac{0.78}{y_{\mathrm{N_2,GC}}}\left(\frac{\dot{V}_{\mathrm{air,in}}\,\rho_{\mathrm{air}}}{\mathcal{M}_{\mathrm{air}}}\right)\mathcal{M}_{\mathrm{CH_4}}.$$

Based on the principle of error propagation, the uncertainty in methane destruction efficiency can be estimated by

$$\Delta\eta_{\mathrm{CH_4,\,des}} = \left(1 - \eta_{\mathrm{CH_4,\,des}}\right)\sqrt{\left(\frac{\Delta y_{\mathrm{CH_4,GC}}}{y_{\mathrm{CH_4,GC}}}\right)^2 + \left(\frac{\Delta y_{\mathrm{N_2,GC}}}{y_{\mathrm{N_2,GC}}}\right)^2}, \tag{A.24}$$

where the uncertainty in standard flow rate of air mixed with the fuel, $\dot{V}_{\mathrm{air,in}}$, and decomposition methane, $\dot{V}_{\mathrm{CH_4,in}}$, are neglected as they were small, and $\frac{\Delta y_{\mathrm{CH_4,GC}}}{y_{\mathrm{CH_4,GC}}}$ and $\frac{\Delta y_{\mathrm{N_2,GC}}}{y_{\mathrm{N_2,GC}}}$ are the uncertainty in molar fraction of methane and nitrogen in the product gas composition, respectively, and can be calculated based on the precision error of repeated measurements using equations (A.1) and (A.2), and the bias uncertainty in the GC ($B_{y_{i,\mathrm{GC}}} = 0.01$ mole%).

Tables A.11 and A.12 highlight the average value and total uncertainty in the destruction efficiency of different flow rates of methane in products of propane-air or methane-air premixed flame, respectively.

Table A.11. Average value and uncertainty in methane destruction efficiency when using propane-air premixed flame as the heat source.

Decomposition methane flow rate (SLPM)	Number of Measurements	Mean methane destruction efficiency	Average uncertainty in molar fraction of methane	Average uncertainty in molar fraction of nitrogen	Average total uncertainty
0.5	5	0.96	24%	2%	0.01
1.0	25	0.77	18%	1%	0.04
1.5	5	0.59	13%	2%	0.05
2.0	5	0.43	8%	2%	0.05
5.0	5	0.20	3%	4%	0.04

Table A.12. Average value and uncertainty in methane destruction efficiency when using methane-air premixed flame as the heat source.

Decomposition methane flow rate (SLPM)	Number of Measurements	Mean methane destruction efficiency	Average uncertainty in molar fraction of methane	Average uncertainty in molar fraction of nitrogen	Average total uncertainty
0.5	5	0.92	11%	1%	0.01
1.0	25	0.69	4%	1%	0.01
1.5	5	0.48	4%	1%	0.02
2.0	5	0.35	3%	1%	0.02
5.0	5	0.02	3%	1%	0.03

A.7 Uncertainty in Hydrogen Production Efficiency

Hydrogen production efficiency is defined as

$$\eta_{H_2} = \frac{\dot{m}_{H_2,out}}{4\,\dot{m}_{H,in}}, \tag{A.25}$$

where $\dot{m}_{H_2,out}$ is the mass flow rate of H_2 yield by the thermal decomposition of methane and can be calculated by

$$\dot{m}_{H_2,out} = \dot{n}_{H_2,out}\,\mathcal{M}_{H_2} = y_{H_2,GC}\,\dot{n}_{total,out}\,\mathcal{M}_{H_2} = y_{H_2,GC}\,\frac{0.78}{y_{N_2,GC}}\left(\frac{\dot{V}_{air,in}\,\rho_{air}}{\mathcal{M}_{air}}\right)\mathcal{M}_{H_2}, \tag{A.26}$$

and $\dot{m}_{H,in}$ is the mass flow rate of hydrogen atoms in the decomposition methane and is determined by

$$\dot{m}_{H,in} = \dot{m}_{CH_4,in}\,\frac{\mathcal{M}_H}{\mathcal{M}_{CH_4}} = \dot{V}_{CH_4,in}\,\rho_{CH_4}\,\frac{\mathcal{M}_H}{\mathcal{M}_{CH_4}}. \tag{A.27}$$

Using a terminology similar to the previous section, the total uncertainty in hydrogen production efficiency is estimated by

$$\frac{\Delta\eta_{H_2}}{\eta_{H_2}} = \sqrt{\left(\frac{\Delta y_{H_2,GC}}{y_{H_2,GC}}\right)^2 + \left(\frac{\Delta y_{N_2,GC}}{y_{N_2,GC}}\right)^2}, \tag{A.28}$$

where the total uncertainty in molar fraction of H_2 $\left(\frac{\Delta y_{H_2,GC}}{y_{H_2,GC}}\right)$ and molar fraction of N_2 $\left(\frac{\Delta y_{N_2,GC}}{y_{N_2,GC}}\right)$ are a combination of precision and bias errors, and can be similarly estimated by using equations (A.1) and (A.2) for the precision uncertainty of repeated measurements and using 0.01 mole% as the absolute bias uncertainty of GC;

$$\frac{\Delta y_{i,\mathrm{GC}}}{y_{i,\mathrm{GC}}} = \sqrt{\left(\frac{B_{y_{i,\mathrm{GC}}}}{y_{i,\mathrm{GC}}}\right)^2 + \left(\frac{P_{y_{i,\mathrm{GC}}}}{y_{i,\mathrm{GC}}}\right)^2}. \quad \text{(A.29)}$$

Tables A.13 and A.14 show the average value and total uncertainty in the hydrogen production efficiency by thermal decomposition of different flow rates of methane in products of propane-air or methane-air premixed flame, respectively.

Table A.13. Average value and uncertainty in hydrogen production efficiency when using propane-air premixed flame as the heat source.

Decomposition methane flow rate (SLPM)	Number of Measurements	Mean hydrogen production efficiency	Average uncertainty in molar fraction of hydrogen	Average uncertainty in molar fraction of nitrogen	Average total uncertainty
0.5	5	0.70	2%	2%	3%
1.0	25	0.55	4%	1%	5%
1.5	5	0.40	4%	2%	3%
2.0	5	0.31	6%	2%	6%
5.0	5	0.13	1%	4%	4%

Table A.14. Average value and uncertainty in hydrogen production efficiency when using methane-air premixed flame as the heat source.

Decomposition methane flow rate (SLPM)	Number of Measurements	Mean hydrogen production efficiency	Average uncertainty in molar fraction of hydrogen	Average uncertainty in molar fraction of nitrogen	Average total uncertainty
0.5	5	0.79	2%	1%	2%
1.0	25	0.54	2%	1%	2%
1.5	5	0.36	2%	1%	2%
2.0	5	0.30	2%	1%	2%
5.0	5	0.10	2%	1%	2%

A.8 Uncertainty in Carbon Black Production Efficiency

As discussed previously, carbon black production efficiency is determined by

$$\eta_{\mathrm{CB}} = \frac{\dot{m}_{\mathrm{CB,out}}}{\dot{m}_{\mathrm{C,in}}}, \tag{A.30}$$

where $\dot{m}_{\mathrm{CB,out}}$ and $\dot{m}_{\mathrm{C},in}$ is the mass flow rate of carbon black from thermal decomposition of methane and the mass flow rate of carbon atoms in the decomposition methane, respectively. $\dot{m}_{\mathrm{CB,out}}$ can be calculated by the following equation and knowing the temperature and pressure of CPC where total mass concentration of carbon black ($M_{\mathrm{total,undiluted}}$) is estimated:

$$\dot{m}_{\mathrm{CB,out}} = M_{\mathrm{total,undiluted}}\,\dot{V}_{\mathrm{total,out}} = M_{\mathrm{total,undiluted}}\,\frac{\dot{n}_{\mathrm{total,out}}\,\bar{\mathrm{R}}\,T}{P} = M_{\mathrm{total,undiluted}}\,\frac{0.78}{y_{\mathrm{N_2,GC}}}\left(\frac{\dot{V}_{\mathrm{air,in}}\,\rho_{\mathrm{air}}}{\mathcal{M}_{\mathrm{air}}}\right)\frac{\bar{\mathrm{R}}\,T}{P}. \tag{A.31}$$

Furthermore, $\dot{m}_{\mathrm{C},in}$ can be calculated by

$$\dot{m}_{C,in} = \dot{m}_{CH_4,in}\,\frac{\mathcal{M}_C}{\mathcal{M}_{CH_4}} = \dot{V}_{\mathrm{CH_4,in}}\,\rho_{\mathrm{CH_4}}\,\frac{\mathcal{M}_C}{\mathcal{M}_{CH_4}}. \tag{A.32}$$

Using the Gaussian error propagation rule, the total uncertainty in carbon black production efficiency is estimated by

$$\frac{\Delta\eta_{\mathrm{CB}}}{\eta_{\mathrm{CB}}} = \sqrt{\left(\frac{\Delta M_{\mathrm{total,undiluted}}}{M_{\mathrm{total,undiluted}}}\right)^2 + \left(\frac{\Delta y_{\mathrm{N_2,GC}}}{y_{\mathrm{N_2,GC}}}\right)^2}, \tag{A.33}$$

where the uncertainty in standard flow rate of air mixed with the fuel, $\dot{V}_{\mathrm{air,in}}$, and decomposition methane, $\dot{V}_{\mathrm{CH_4,in}}$, as well as the uncertainty in CPC temperature, *T*, and pressure, *P*, are neglected as they expected to be small and $\frac{\Delta M_{\mathrm{total,undiluted}}}{M_{\mathrm{total,undiluted}}}$ can be obtained from Tables A.5 and A.6, and $\frac{\Delta y_{\mathrm{N_2,GC}}}{y_{\mathrm{N_2,GC}}}$ can be estimated from equation (A.29).

Tables A.15 and A.16 show the average value and total uncertainty in the carbon black production efficiency by thermal decomposition of different flow rates of methane in products of propane-air or methane-air premixed flame, respectively.

Table A.15. Average value and uncertainty in carbon black production efficiency when using propane-air premixed flame as the heat source.

Decomposition methane flow rate (SLPM)	Number of Measurements	Mean carbon black production efficiency	Average uncertainty in total mass concentration of carbon black	Average uncertainty in molar fraction of nitrogen	Average total uncertainty
0.5	5	0.0084	64%	2%	64%
1.0	5	0.0068	60%	1%	60%
1.5	5	0.0027	55%	2%	55%
2.0	5	0.0013	55%	2%	55%
5.0	5	<0.0001	97%	4%	97%

Table A.16. Average value and uncertainty in carbon black production efficiency when using methane-air premixed flame as the heat source.

Decomposition methane flow rate (SLPM)	Number of Measurements	Mean carbon black production efficiency	Average uncertainty in total mass concentration of carbon black	Average uncertainty in molar fraction of nitrogen	Average total uncertainty
0.5	5	0.0008	87%	1%	87%
1.0	5	0.0008	53%	1%	53%
1.5	5	0.0003	88%	1%	88%
2.0	5	0.0002	106%	1%	106%
5.0	5	<0.0001	175%	1%	175%

Appendix B TEM Images

In this section, all the TEM images analyzed for different conditions of TDM are presented in tables below.

Label of an image in a table referrers to the TEM grid and image number in the specific condition of TDM mentioned in the table caption (*i.e.* A5-1 referrers to image 1 of grid A5 collected for TDM with 0.5 SLPM of decomposition methane and propane-air premixed flame).

Table B.1. TEM images of carbon particulates with 0.5 SLPM of decomposition methane and propane-air premixed flame (part 1).

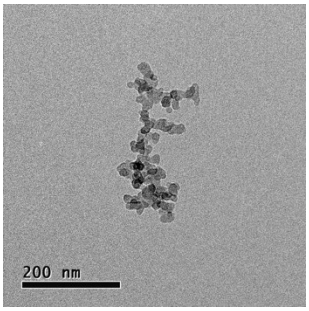

A5-1

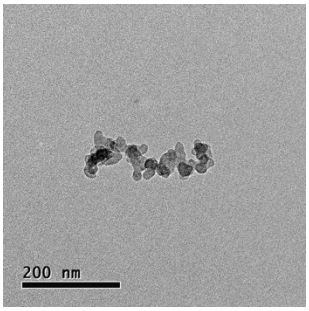

A5-2

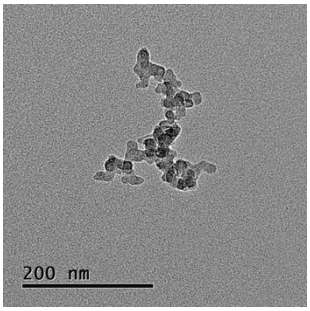

A5-3

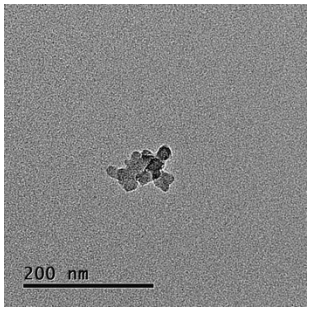

A5-4

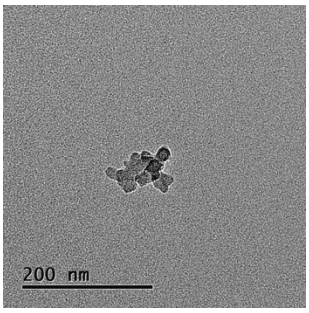

A5-5

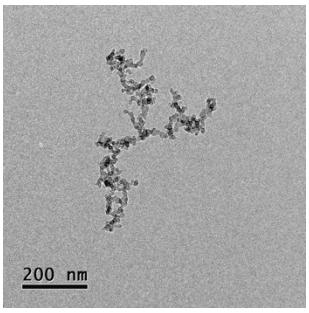

A5-6

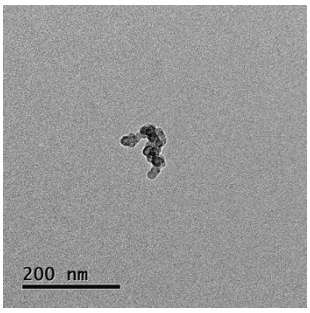

A5-7

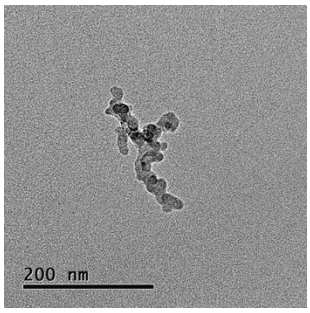

A5-8

Table B.2. TEM images of carbon particulates with 0.5 SLPM of decomposition methane and propane-air premixed flame (part 2).

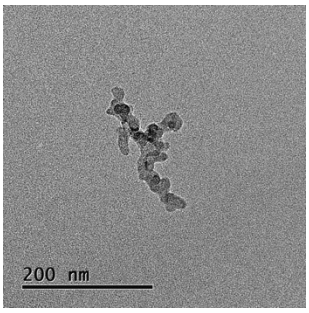

A5-9

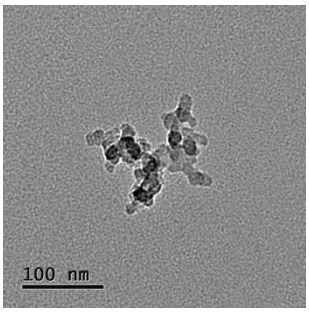

A5-10

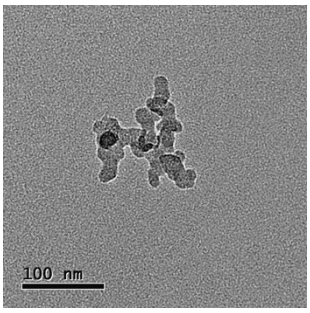

A5-11

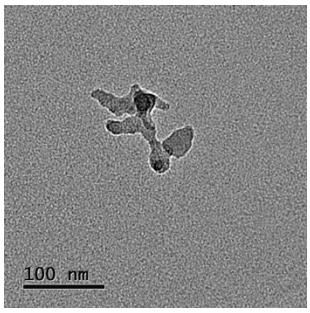

A5-12

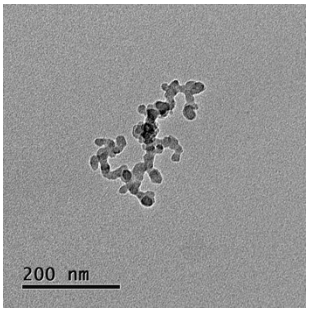

A5-13

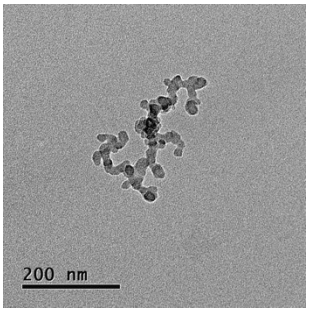

A5-14

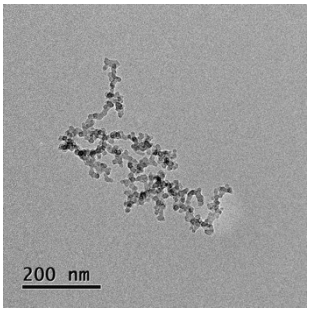

A5-15

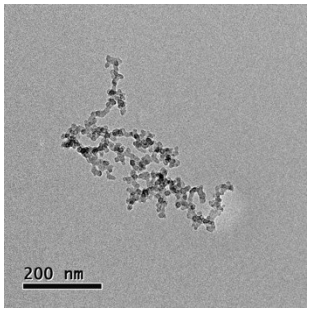

A5-16

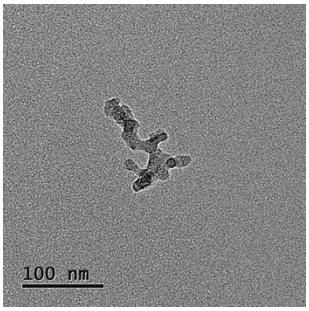

A5-17

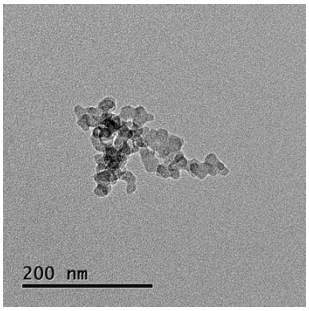

A5-18

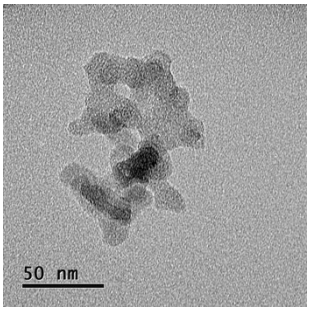

B5-1

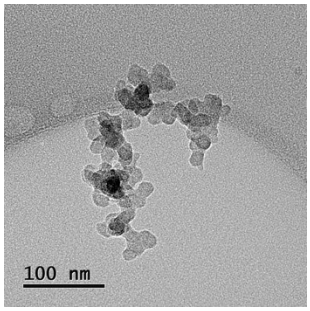

B5-2

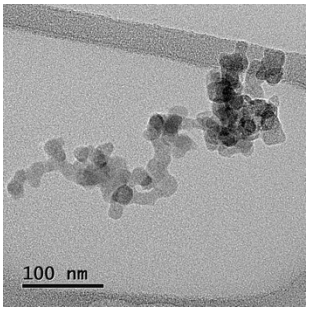

B5-3

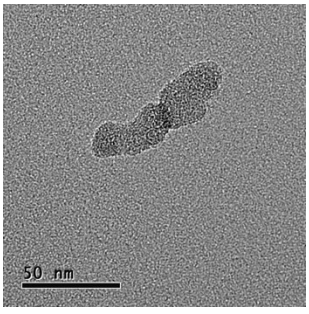

B5-4

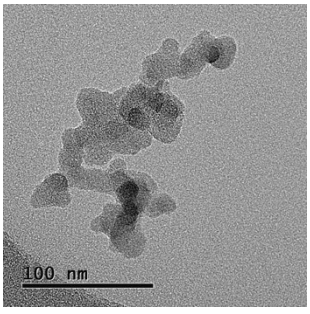

B5-5

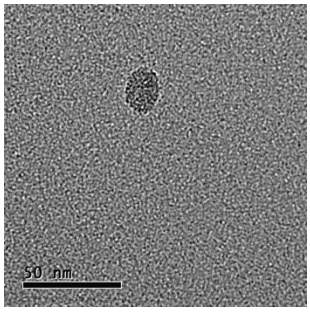

B5-6

Table B.3. TEM images of carbon particulates with 0.5 SLPM of decomposition methane and propane-air premixed flame (part 3).

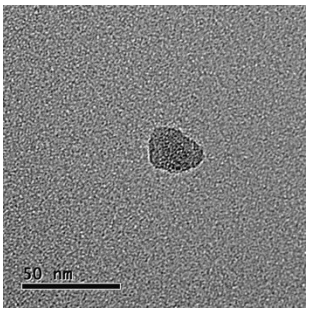

B5-7

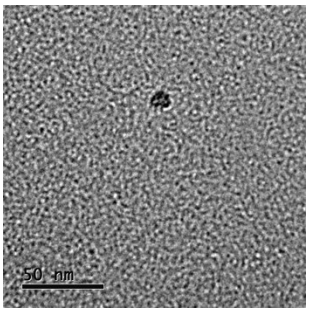

B5-8

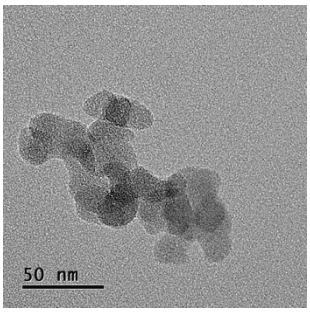

B5-9

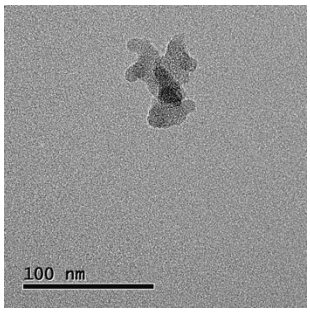

B5-10

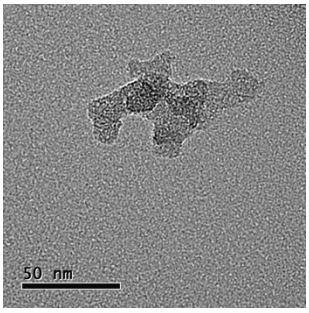

B5-11

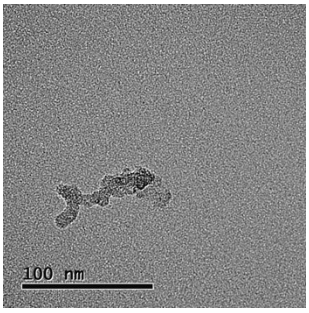

B5-12

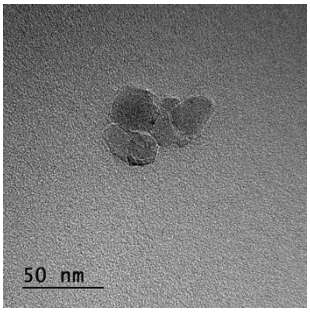

A1-1

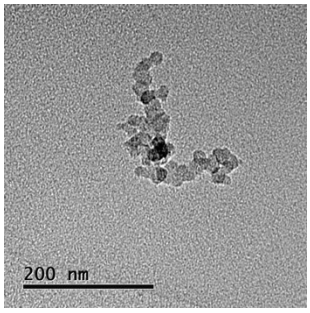

A6-1

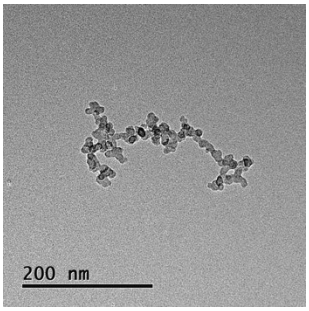

A6-2

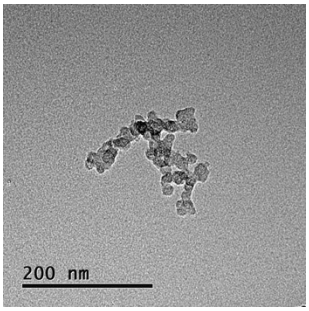

A6-3

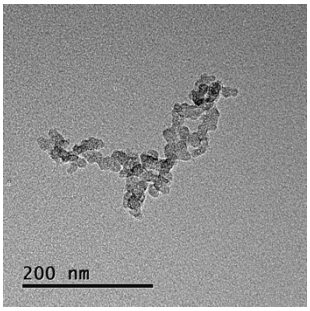

A6-4

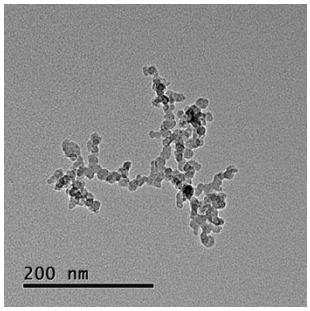

A6-5

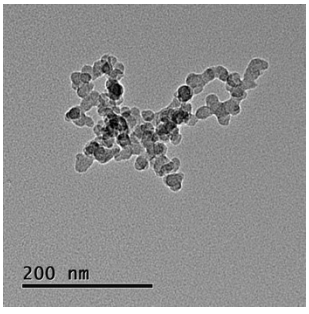

A6-6

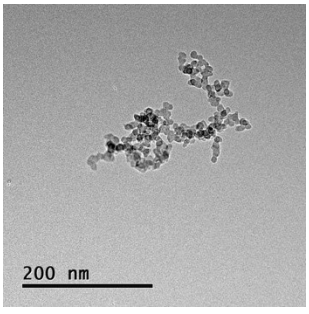

A6-7

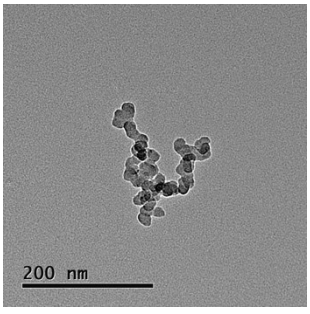

A6-8

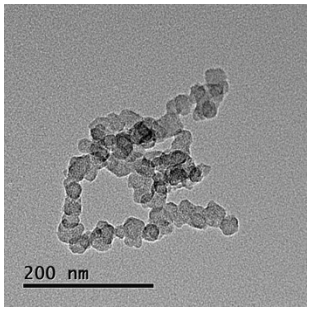

A6-9

Table B.4. TEM images of carbon particulates with 0.5 SLPM of decomposition methane and propane-air premixed flame (part 4).

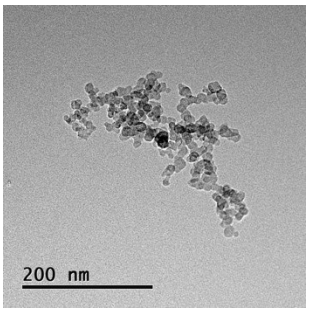	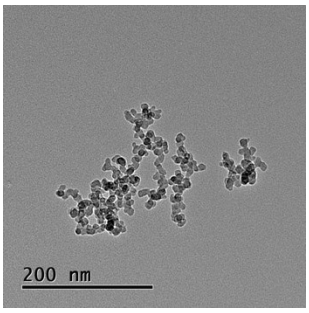	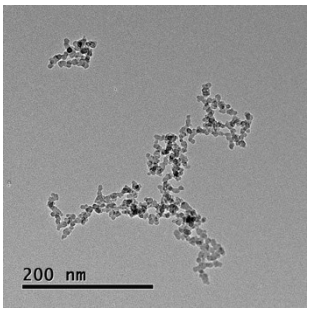	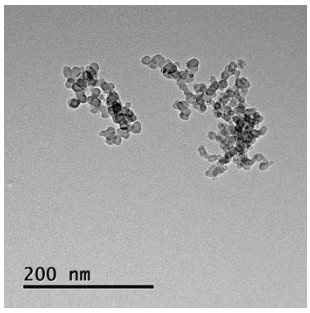
A6-10	A6-11	A6-12	A6-13
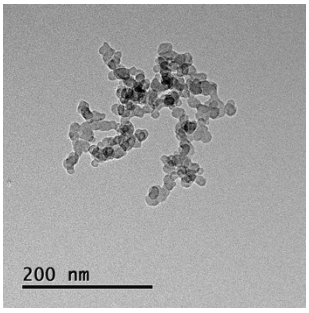	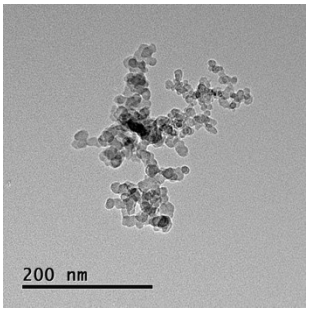	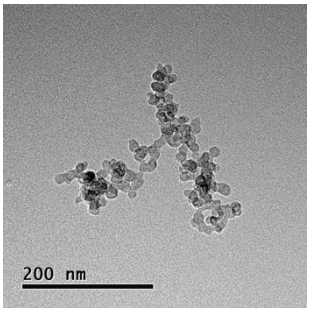	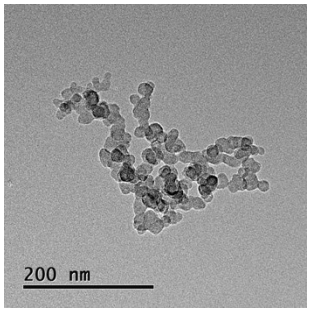
A6-14	A6-15	A6-16	A6-17
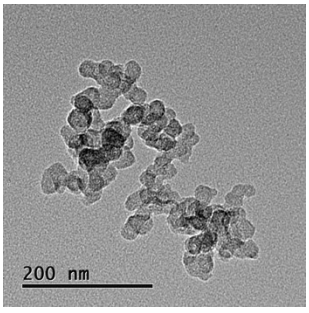	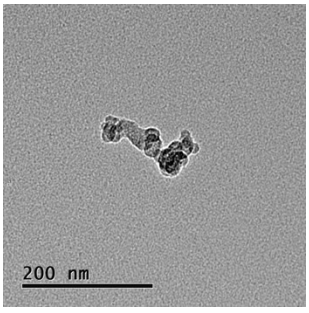	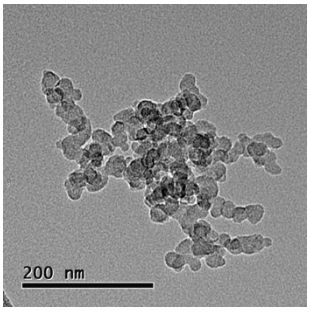	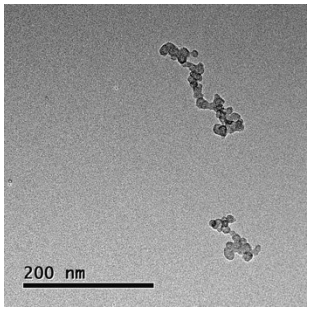
A6-18	A6-19	A6-20	A6-21
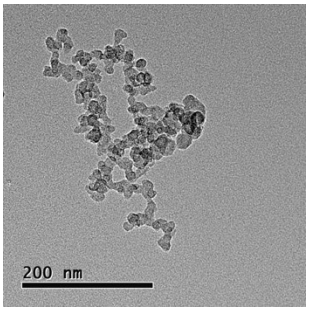	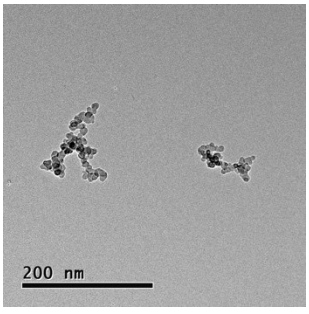	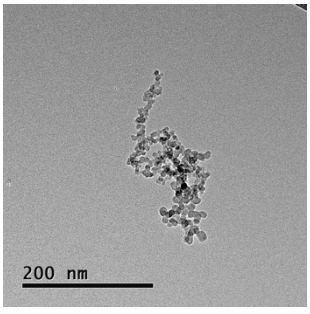	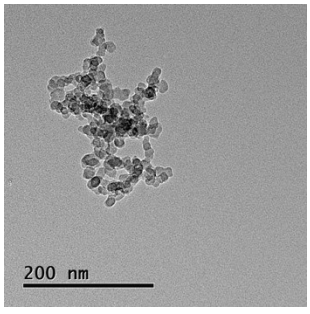
A6-22	A6-23	A6-24	A6-25

Table B.5. TEM images of carbon particulates with 1.0 SLPM of decomposition methane and propane-air premixed flame (part 1).

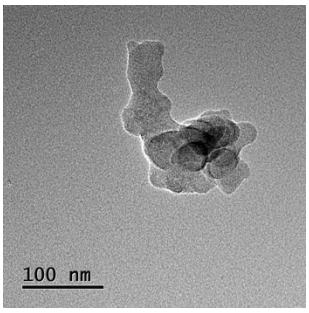

B6-1

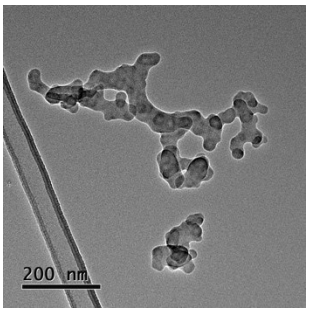

B6-2

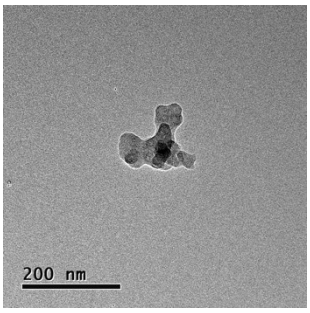

B6-3

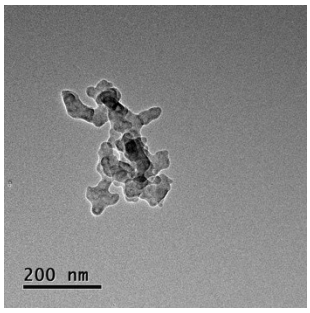

B6-4

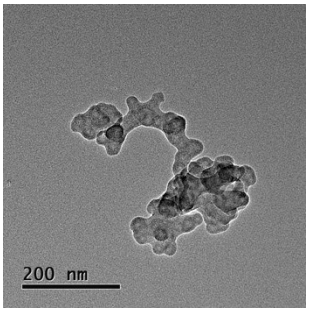

B6-5

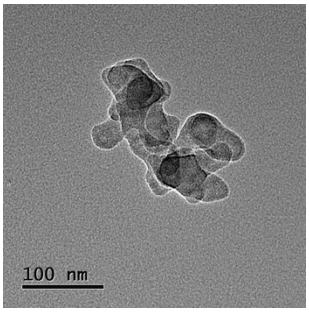

B6-6

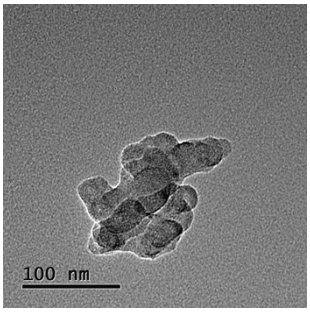

B6-7

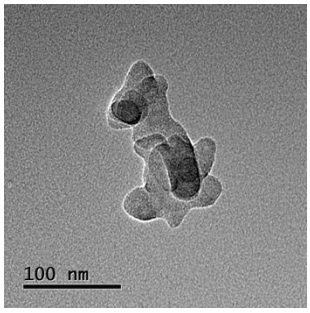

B6-8

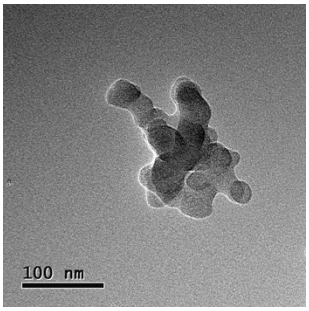

B6-9

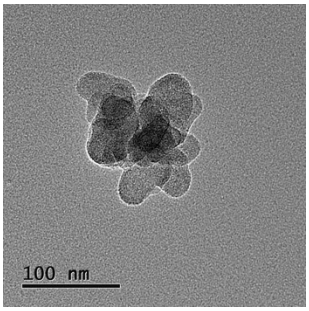

B6-10

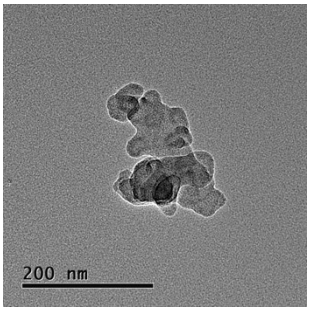

B6-11

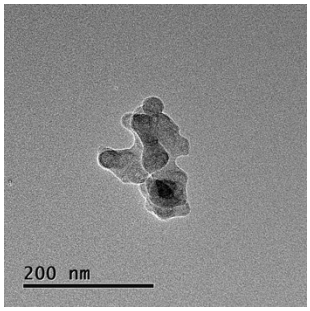

B6-12

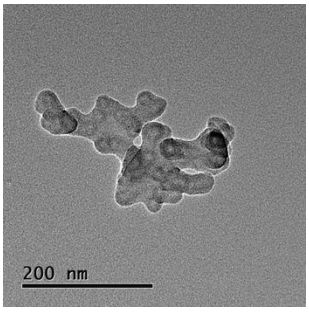

B6-13

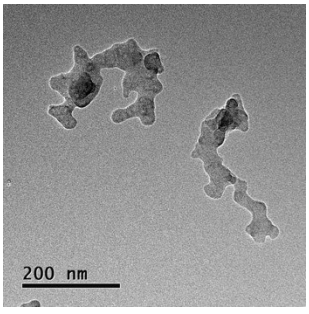

B6-14

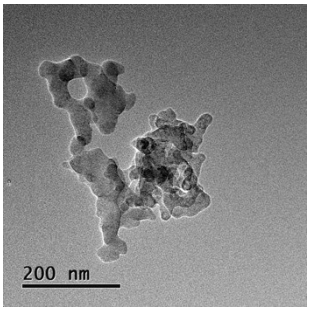

B6-15

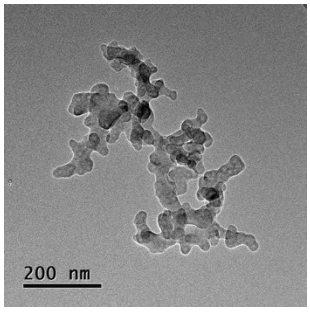

B6-16

Table B.6. TEM images of carbon particulates with 1.0 SLPM of decomposition methane and propane-air premixed flame (part 2).

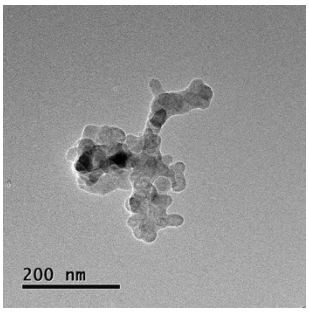

B6-17

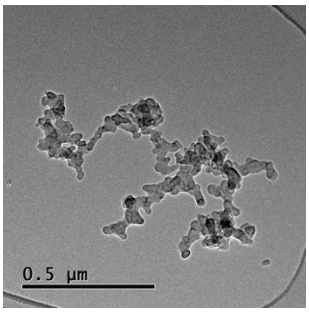

B6-18

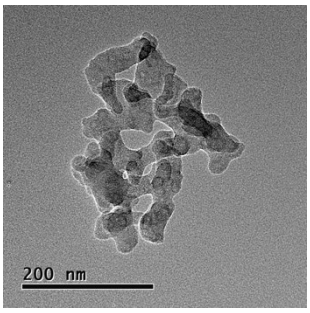

B6-19

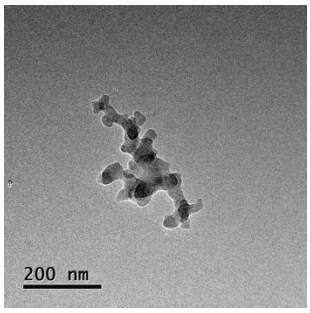

B6-20

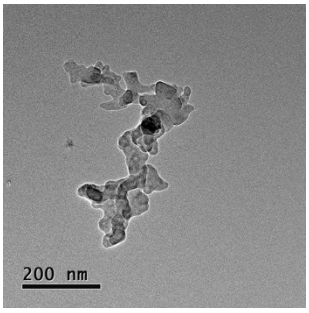

B6-21

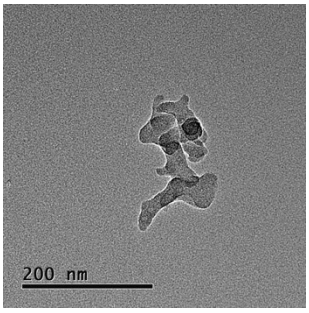

B6-22

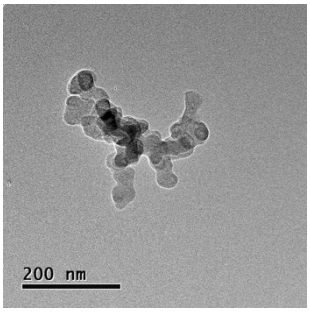

B6-23

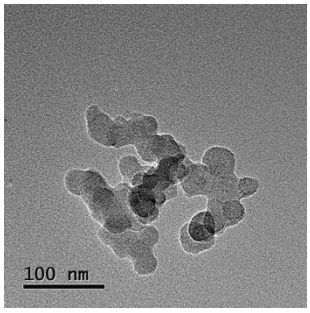

B6-24

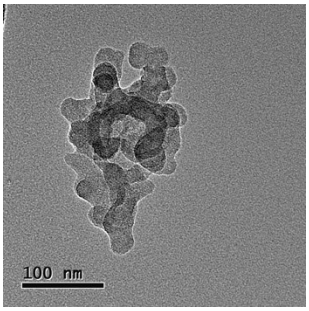

B6-25

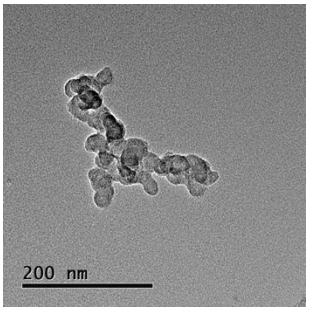

B6-26

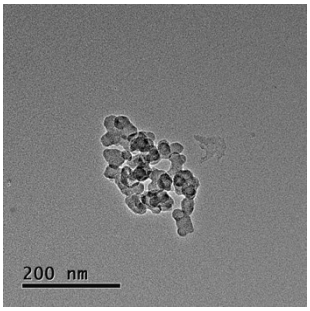

B6-27

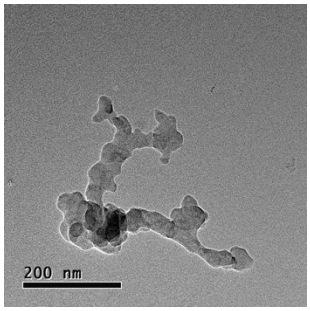

B6-28

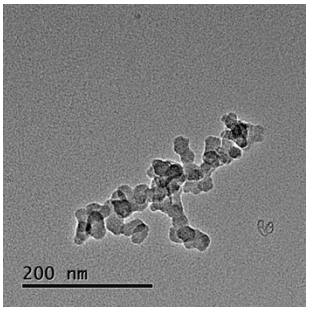

B6-29

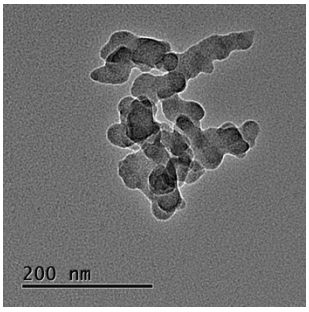

B6-30

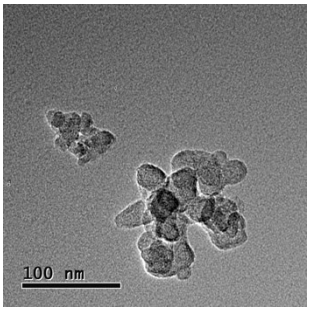

B6-31

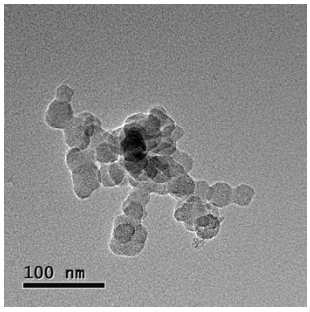

B6-32

Table B.7. TEM images of carbon particulates with 1.0 SLPM of decomposition methane and propane-air premixed flame (part 3).

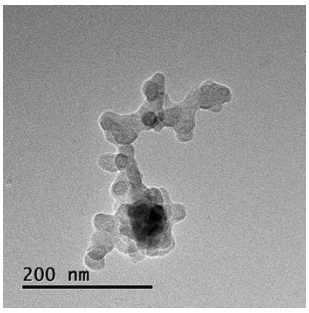

B6-33

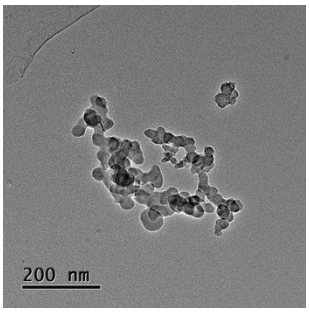

B6-34

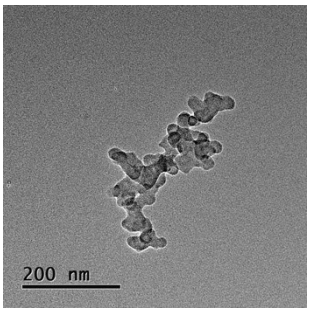

B6-35

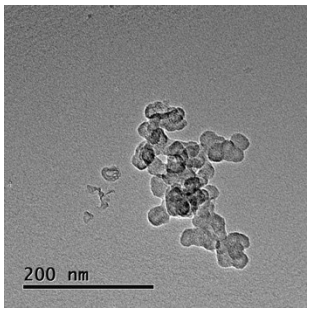

B6-36

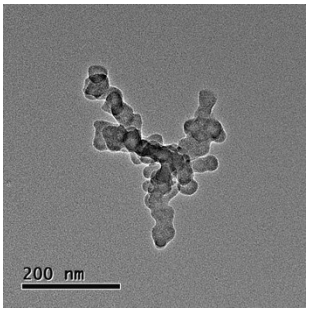

B6-37

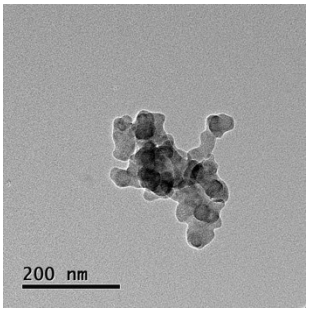

B6-38

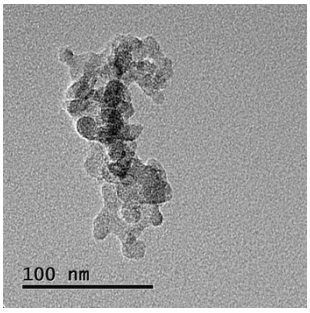

B6-39

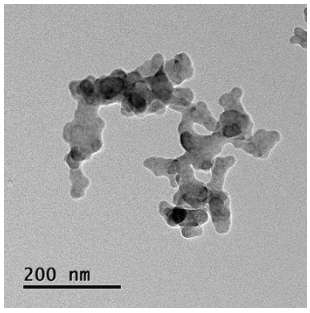

B6-40

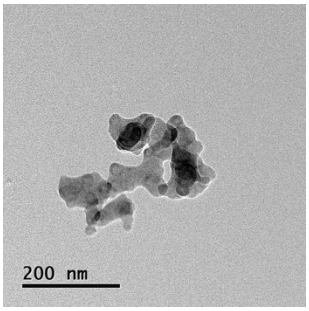

B6-41

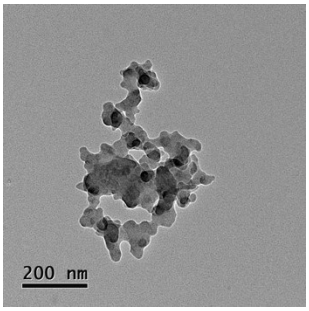

B6-42

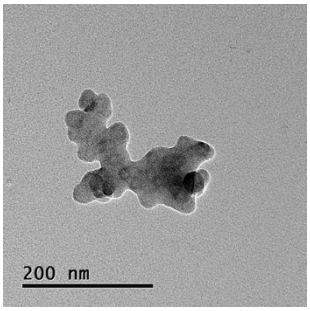

B6-43

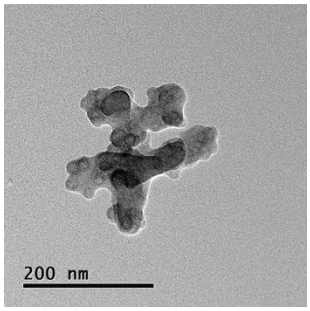

B6-44

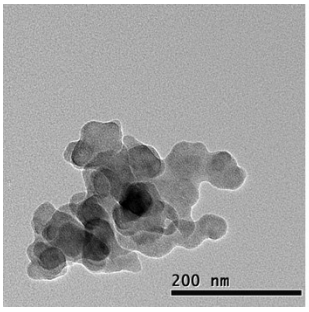

B6-45

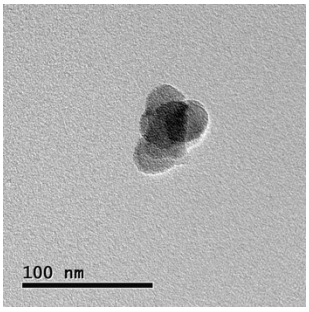

B6-46

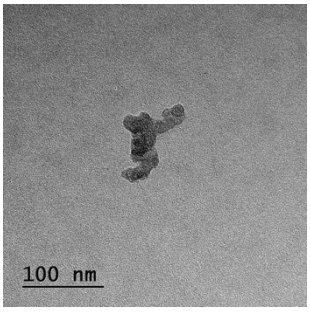

B2-1

Table B.8. TEM images of carbon particulates with 1.5 SLPM of decomposition methane and propane-air premixed flame (part 1).

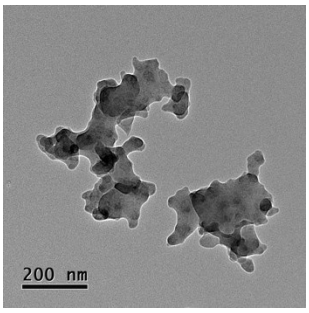

C6-1

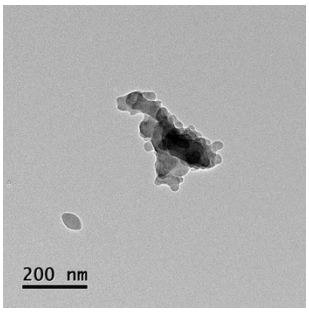

C6-2

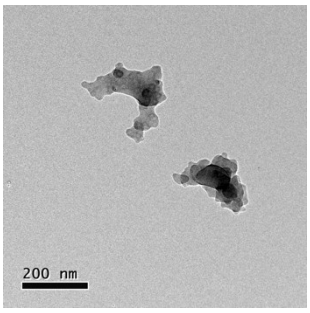

C6-3

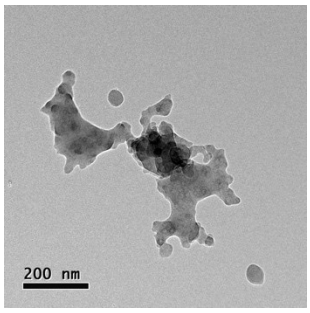

C6-4

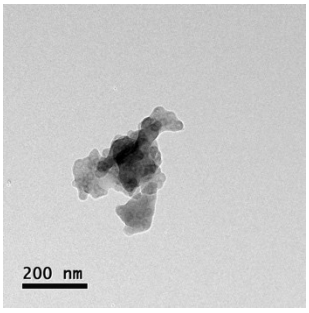

C6-5

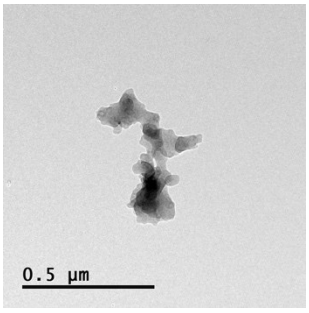

C6-6

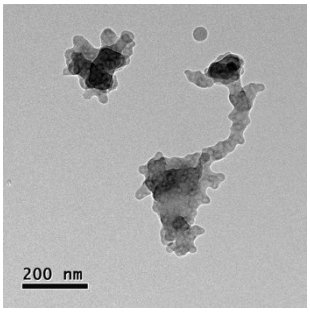

C6-7

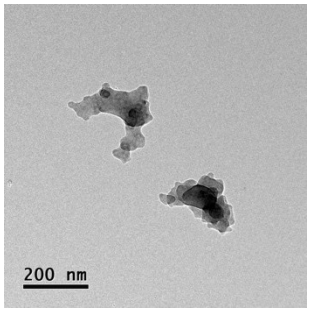

C6-8

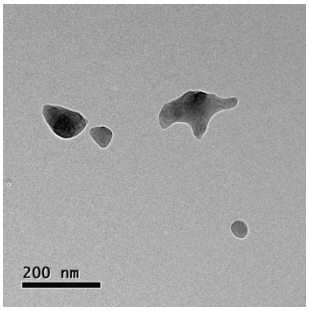

C6-9

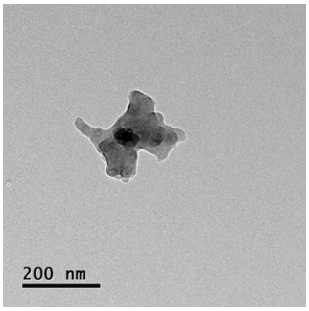

C6-10

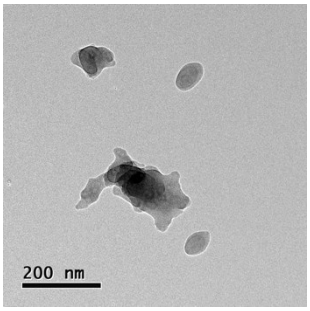

C6-11

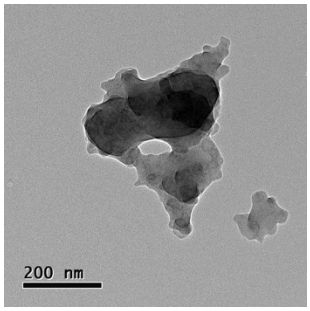

C6-12

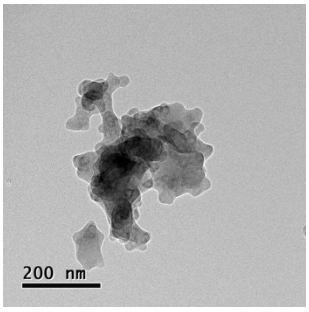

C6-13

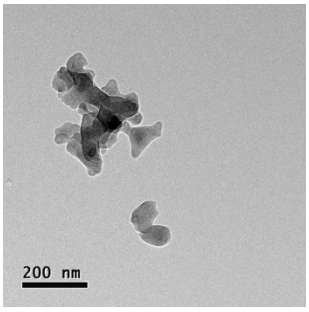

C6-14

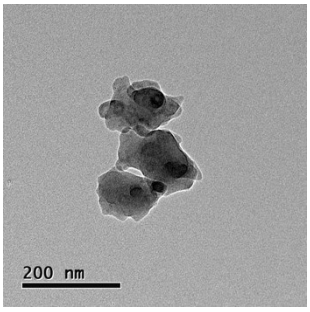

C6-15

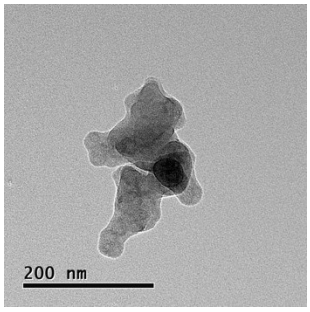

C6-16

Table B.9. TEM images of carbon particulates with 1.5 SLPM of decomposition methane and propane-air premixed flame (part 2).

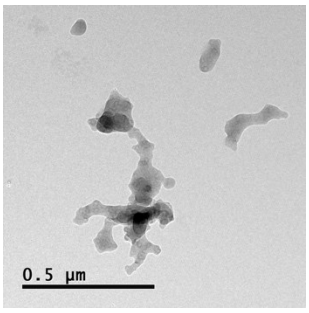

C6-17

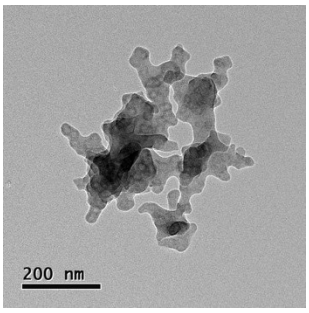

C6-18

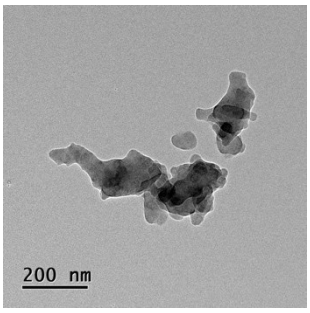

C6-19

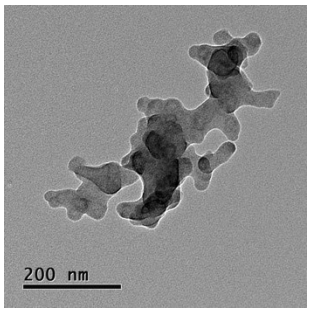

C6-20

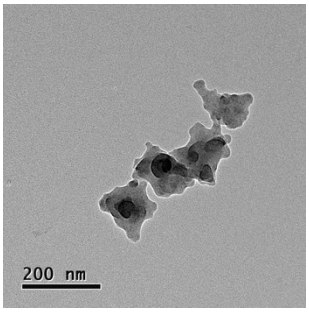

C6-21

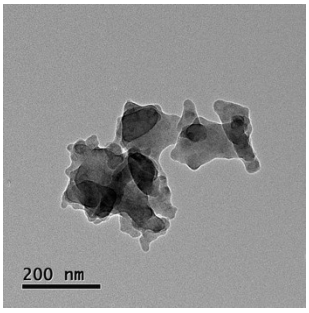

C6-22

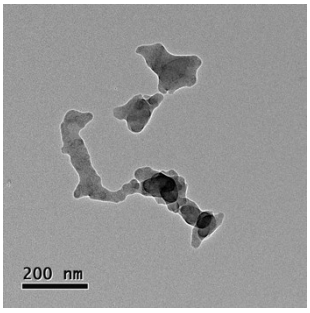

C6-23

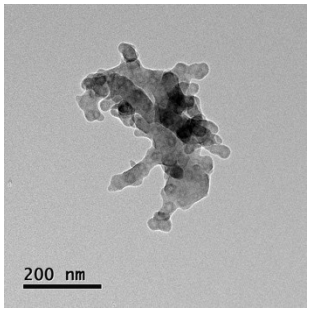

C6-24

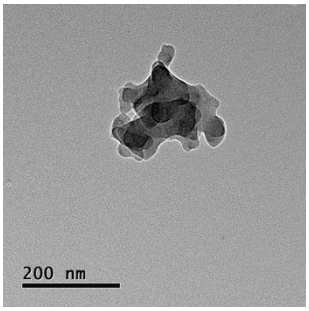

C6-25

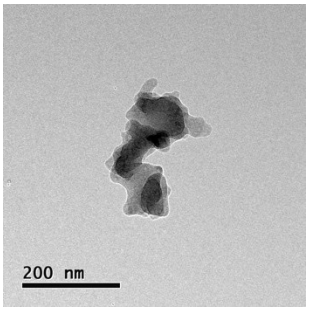

C6-26

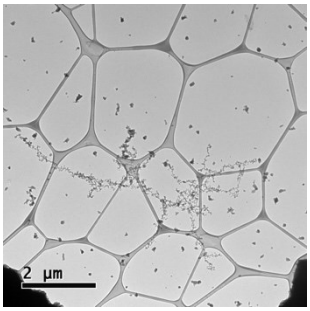

C6-27

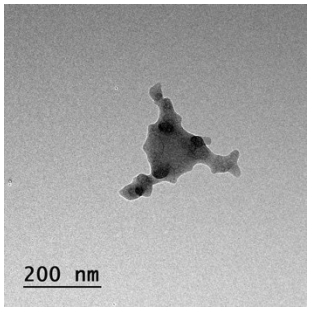

C6-28

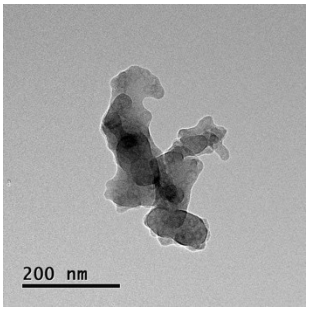

C6-29

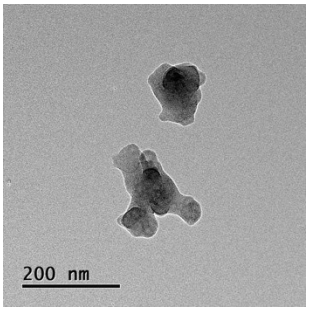

C6-30

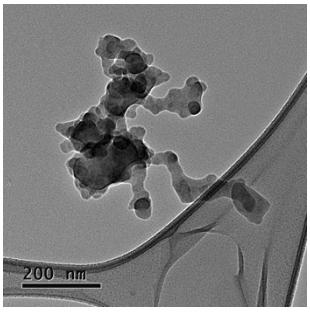

C6-31

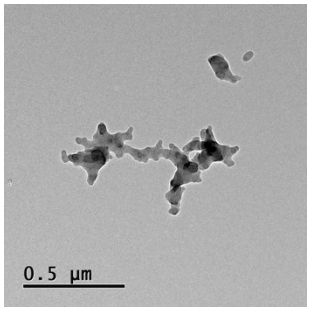

C6-32

Table B.10. TEM images of carbon particulates with 1.5 SLPM of decomposition methane and propane-air premixed flame (part 3).

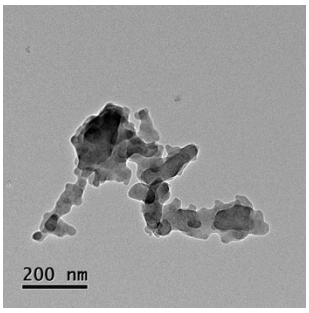

C6-33

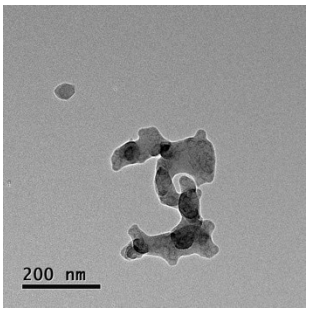

C6-34

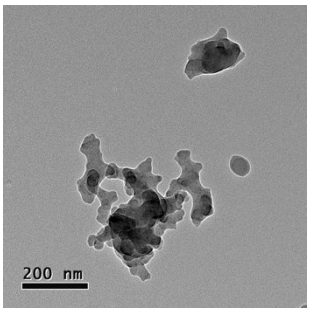

C6-35

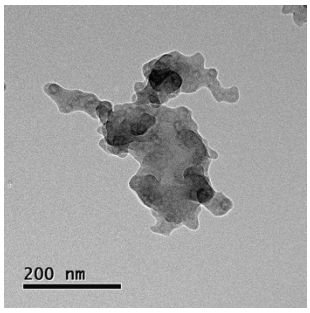

C6-36

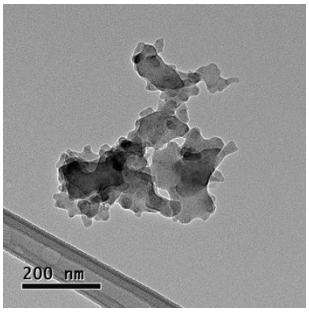

C6-37

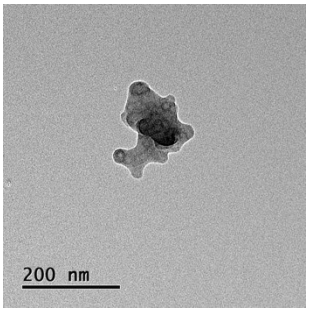

C6-38

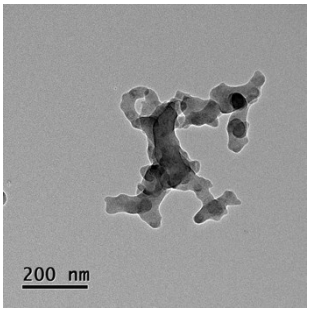

C6-39

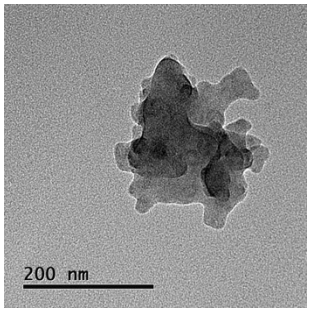

C6-40

Table B.11. TEM images of carbon particulates with 2.0 SLPM of decomposition methane and propane-air premixed flame (part 1).

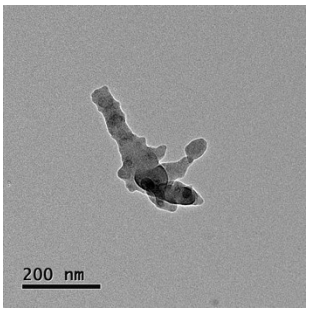

D6-1

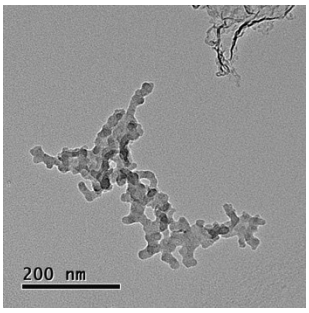

D6-2

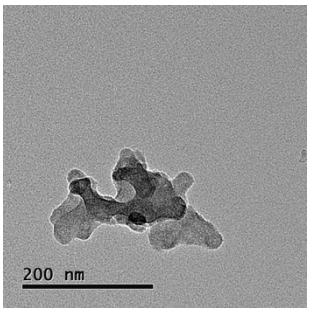

D6-3

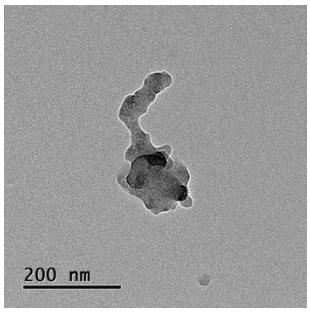

D6-4

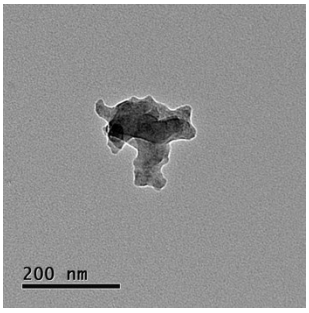

D6-5

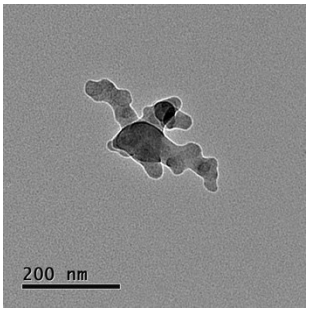

D6-6

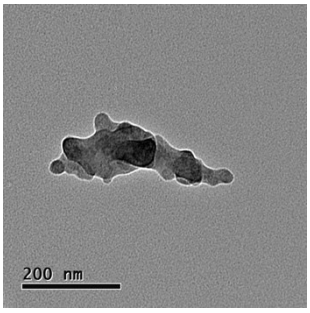

D6-7

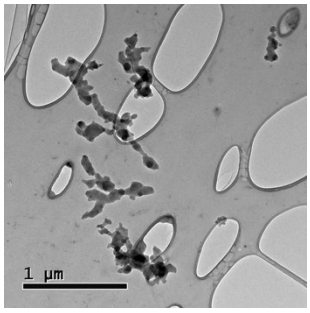

D6-8

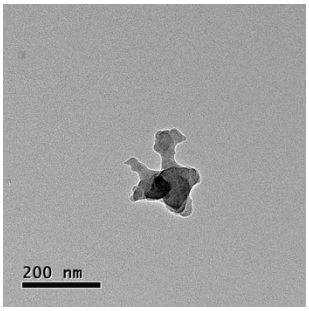

D6-9

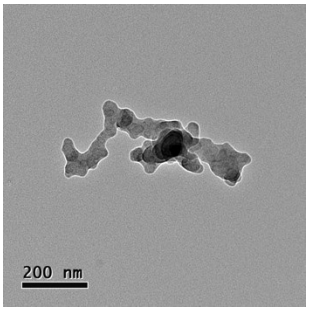

D6-10

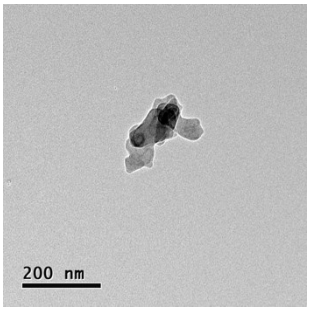

D6-11

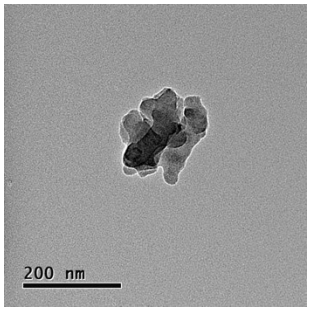

D6-12

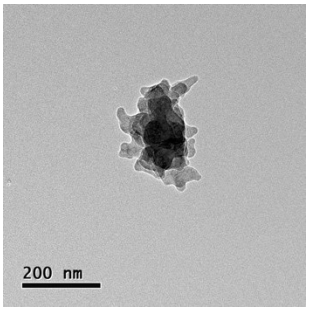

D6-13

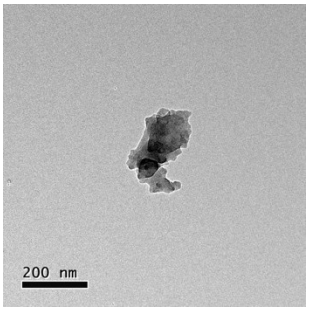

D6-14

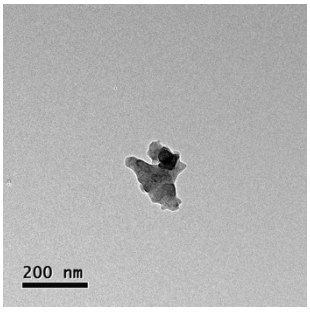

D6-15

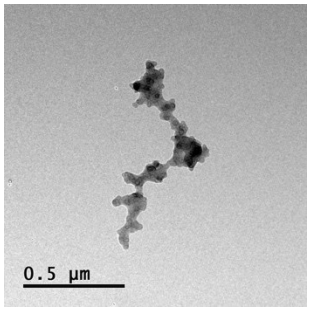

D6-16

Table B.12. TEM images of carbon particulates with 2.0 SLPM of decomposition methane and propane-air premixed flame (part 2).

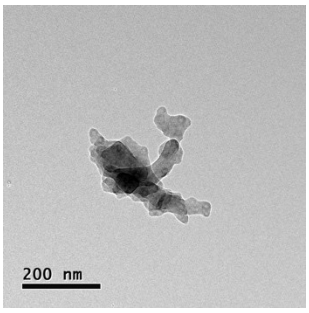

D6-17

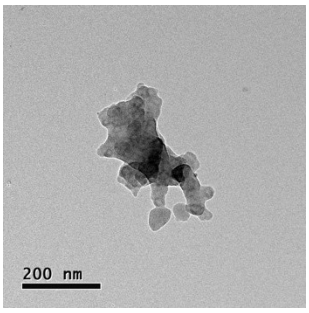

D6-18

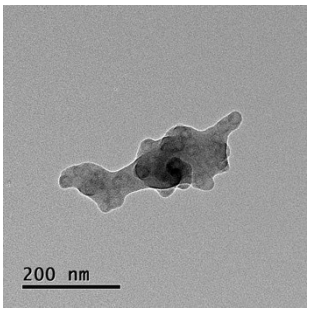

D6-19

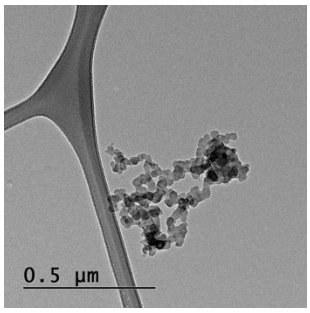

D6-20

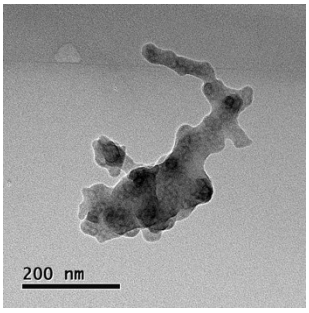

D6-21

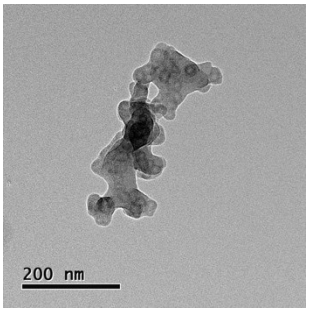

D6-22

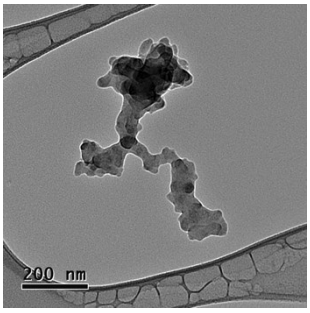

D6-23

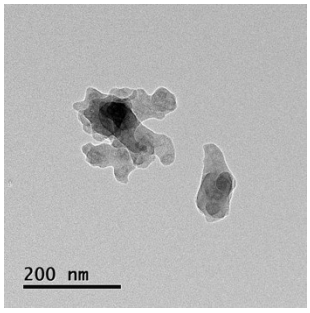

D6-24

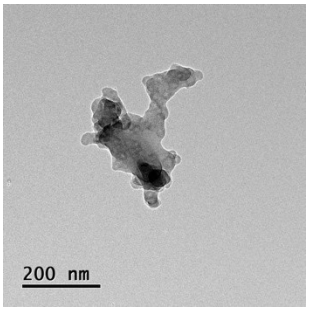

D6-25

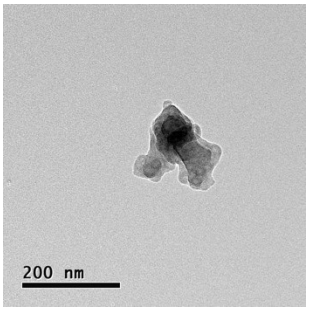

D6-26

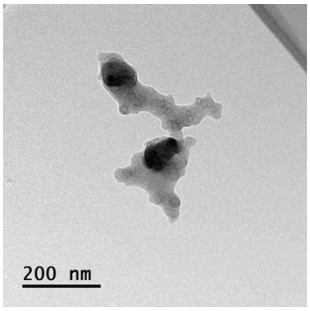

D6-27

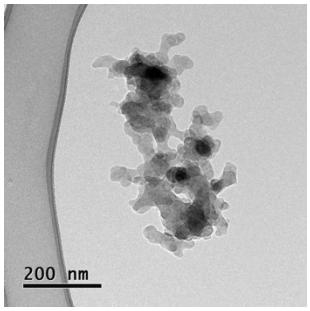

D6-28

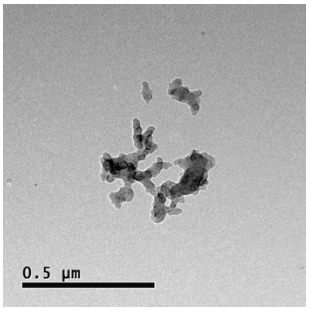

D6-29

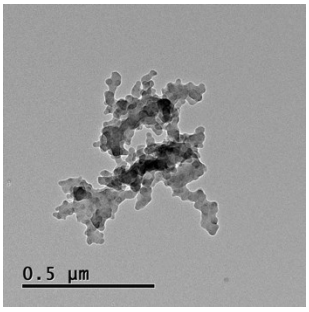

D6-30

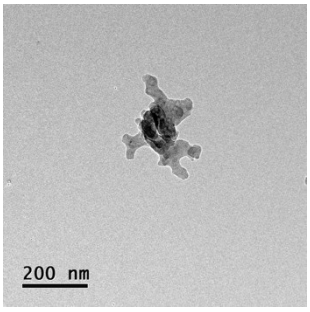

D6-31

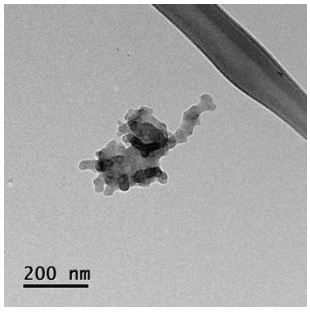

D6-32

Table B.13. TEM images of carbon particulates with 2.0 SLPM of decomposition methane and propane-air premixed flame (part 3).

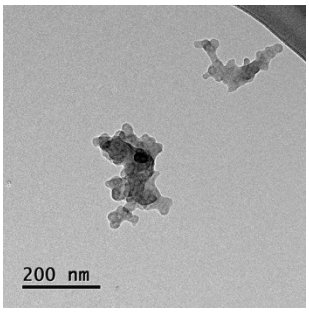	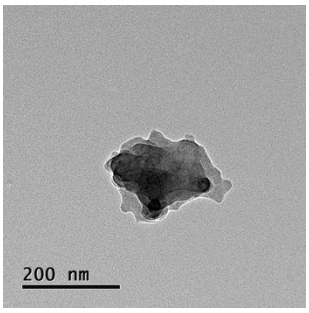	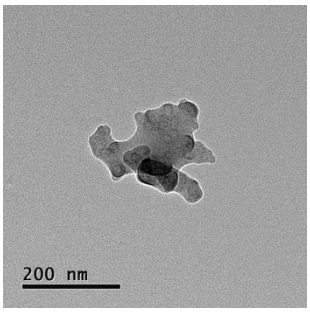	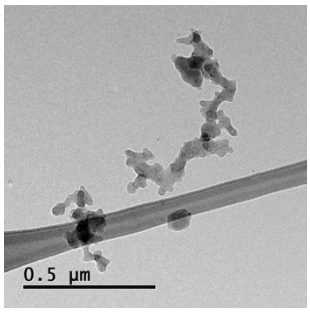
D6-33	D6-34	D6-35	D6-36
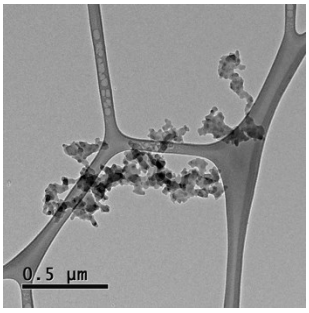	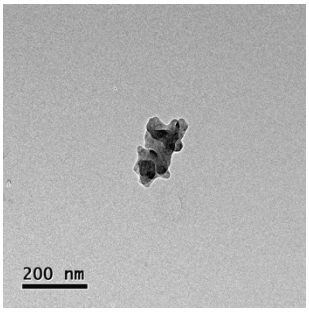	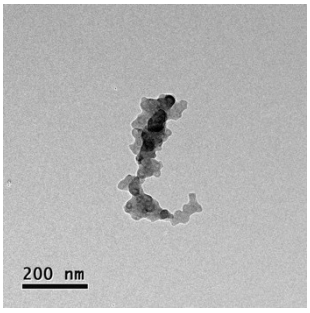	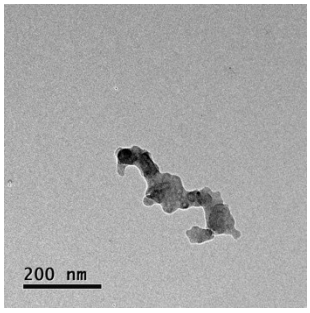
D6-37	D6-38	D6-39	D6-40
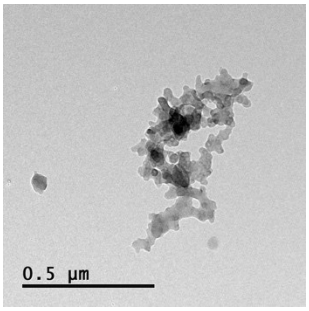	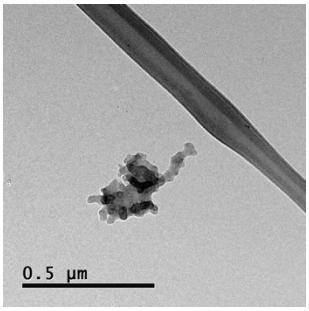	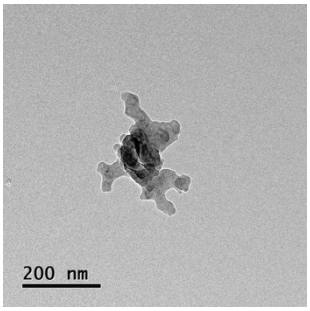	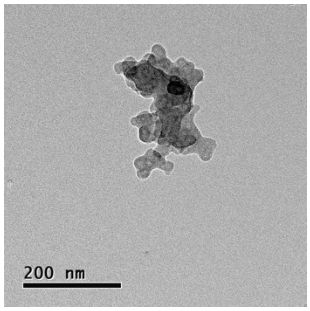
D6-41	D6-42	D6-43	D6-44
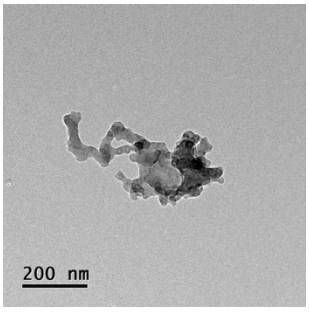	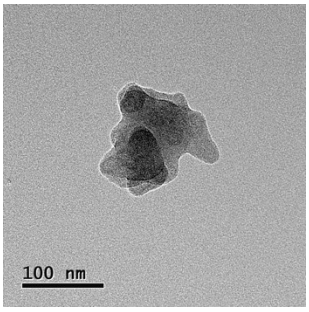	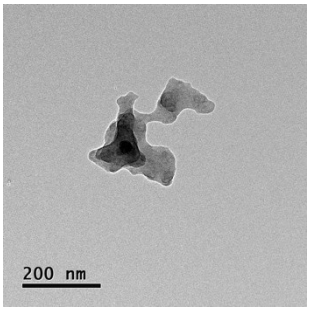	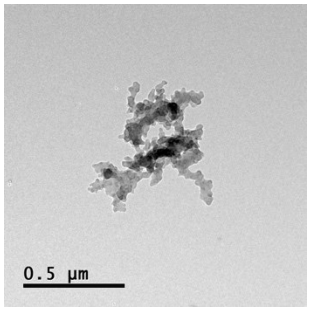
D6-45	D6-46	D6-47	D6-48

Table B.14. TEM images of carbon particulates with 5.0 SLPM of decomposition methane and propane-air premixed flame (part 1).

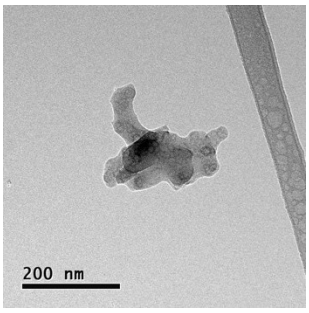

E6-1

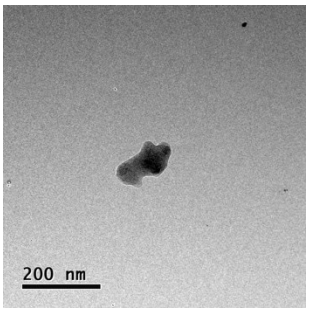

E6-2

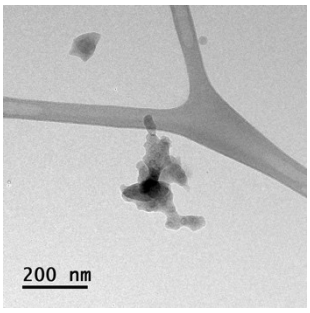

E6-3

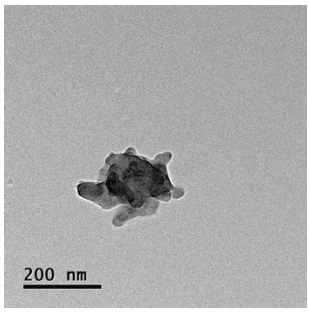

E6-4

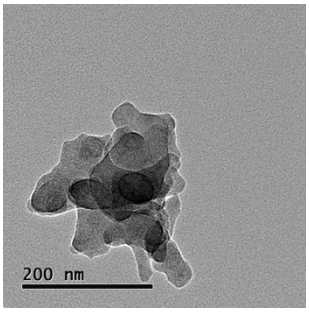

E6-5

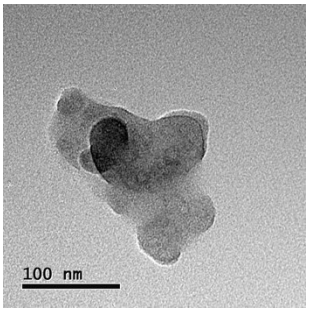

E6-6

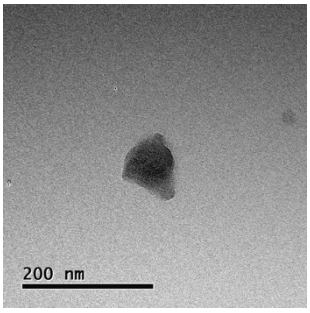

E6-7

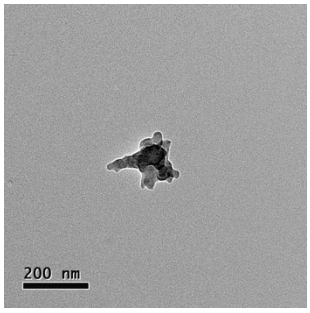

E6-8

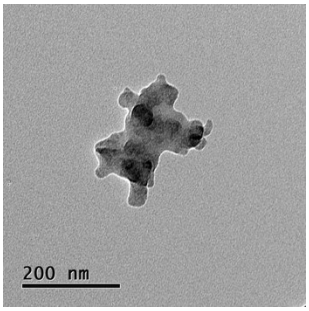

E6-9

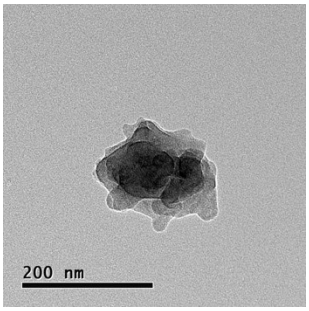

E6-10

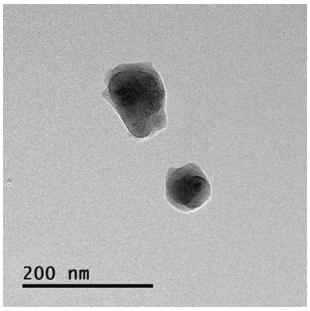

E6-11

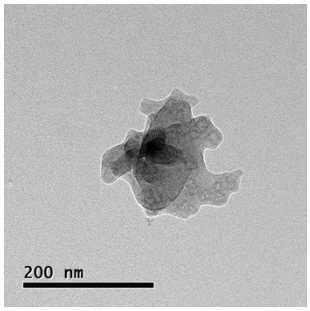

E6-12

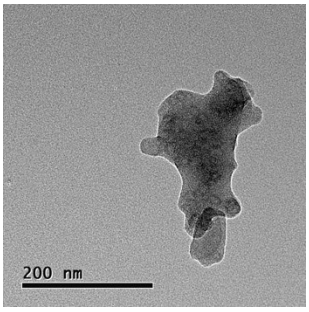

E6-13

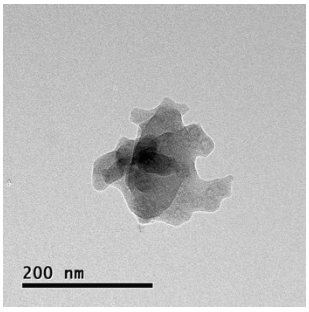

E6-14

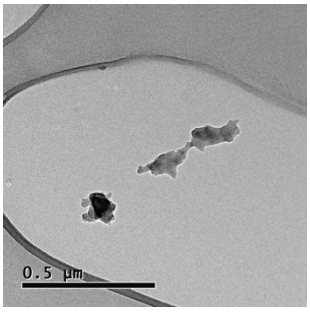

E6-15

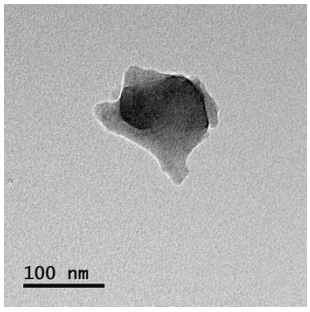

E6-16

Table B.15. TEM images of carbon particulates with 5.0 SLPM of decomposition methane and propane-air premixed flame (part 2).

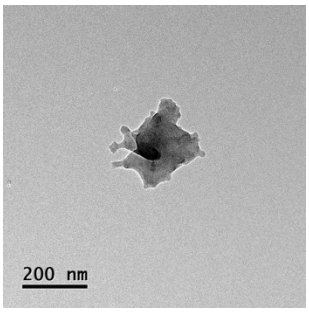

E6-17

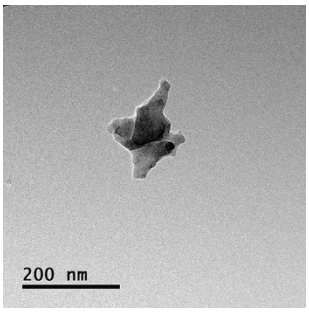

E6-18

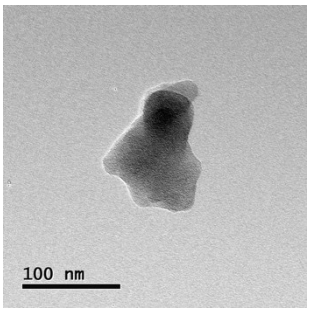

E6-19

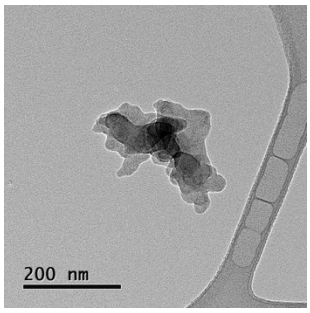

E6-20

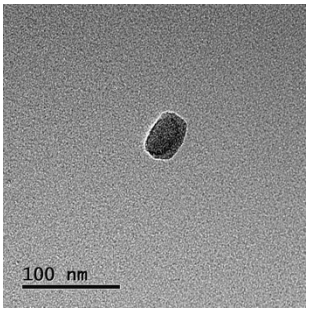

E6-21

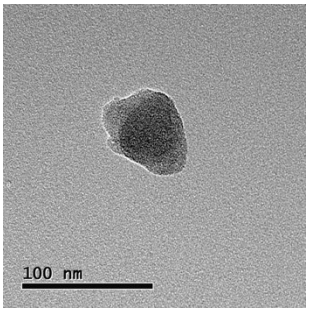

E6-22

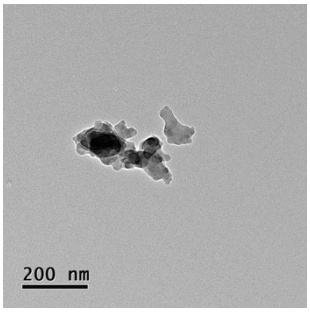

E6-23

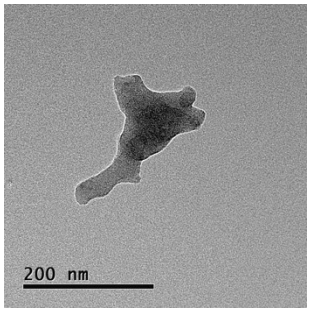

E6-24

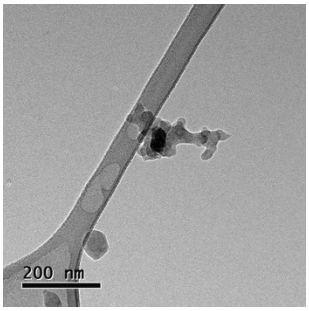

E6-25

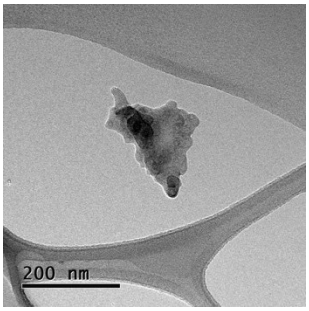

E6-26

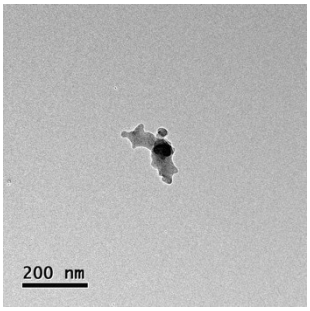

E6-27

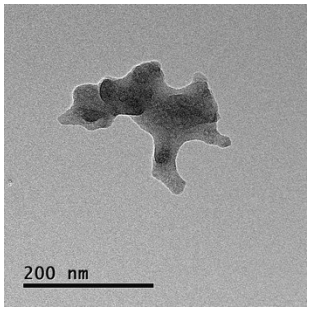

E6-28

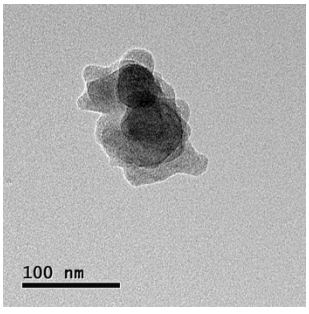

E6-29

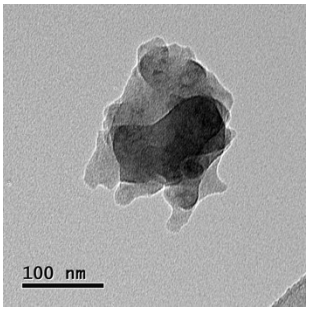

E6-30

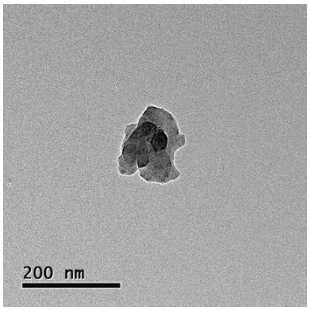

E6-31

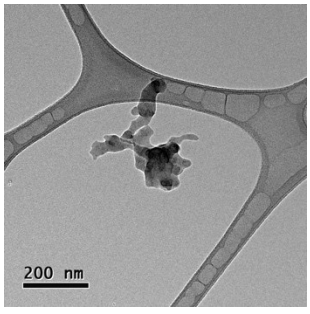

E6-32

Table B.16. TEM images of carbon particulates with 0.5 SLPM of decomposition methane and methane-air premixed flame (part 1).

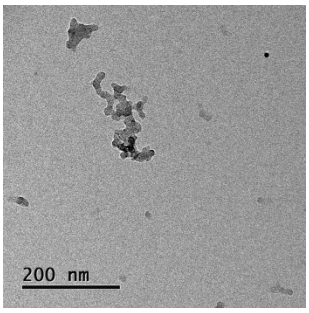

A8-1

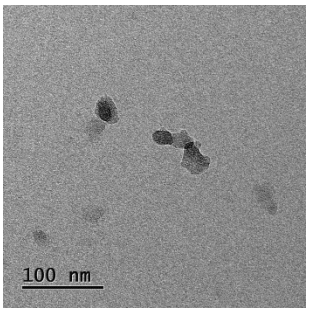

A8-2

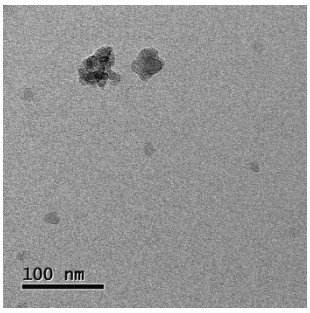

A8-3

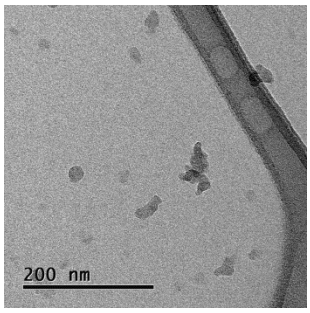

A8-4

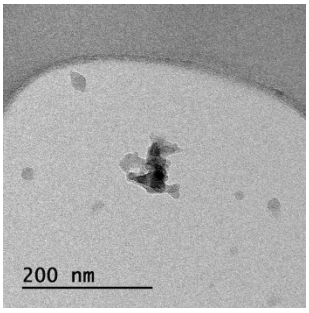

A8-5

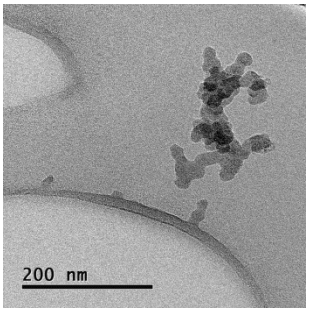

A8-6

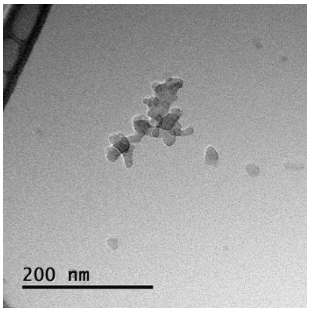

A8-7

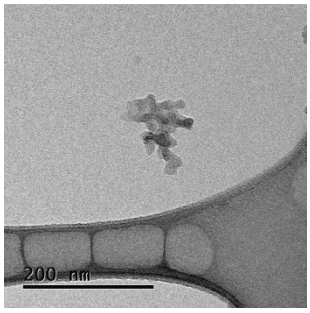

A8-8

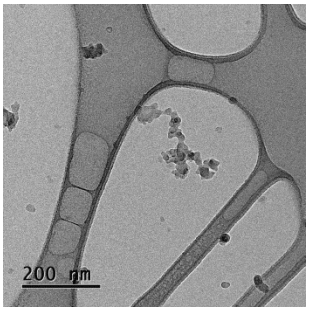

A8-9

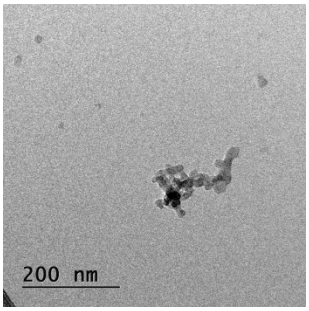

A8-10

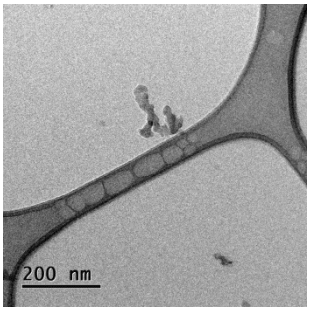

A8-11

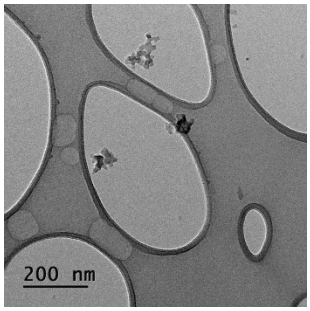

A8-12

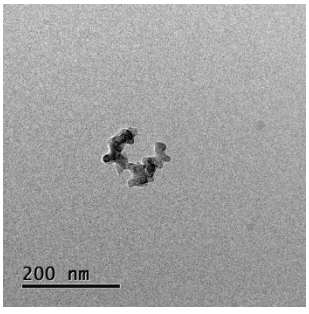

A8-13

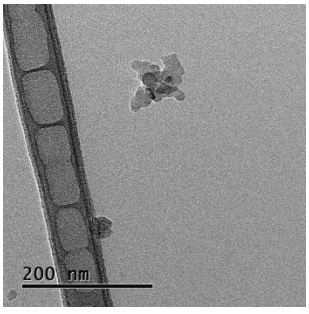

A8-14

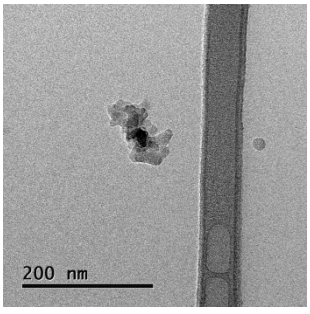

A8-15

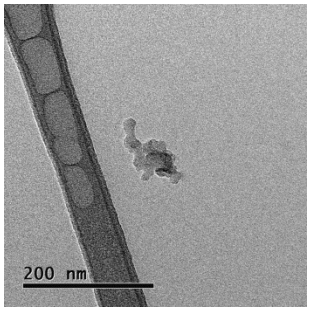

A8-16

Table B.17. TEM images of carbon particulates with 0.5 SLPM of decomposition methane and methane-air premixed flame (part 2).

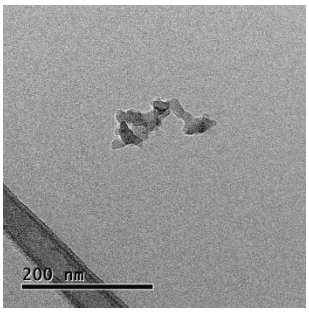

A8-17

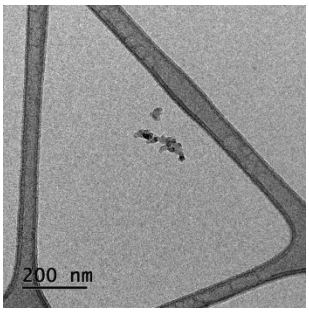

A8-18

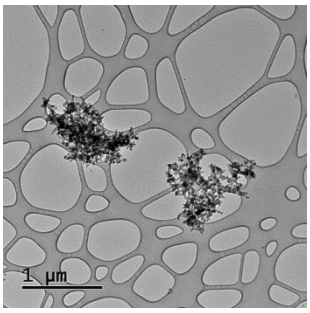

A8-19

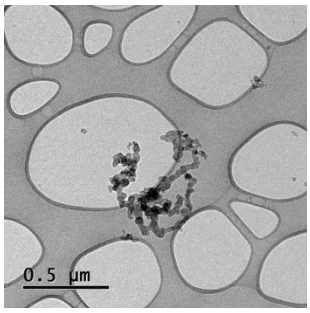

A8-20

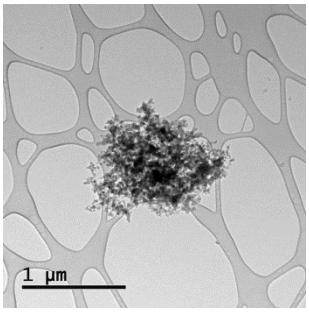

A8-21

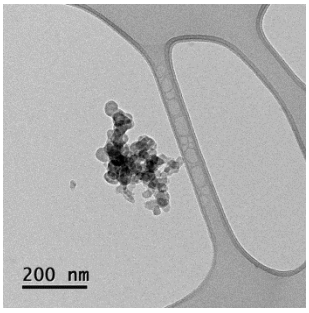

A8-22

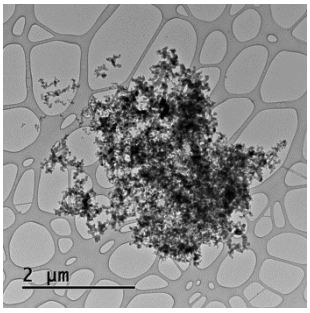

A8-23

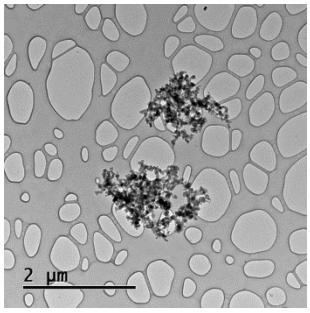

A8-24

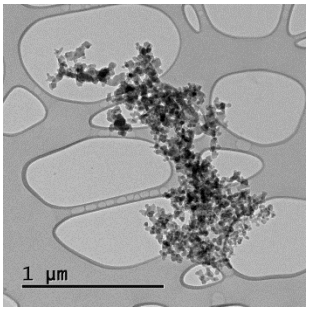

A8-25

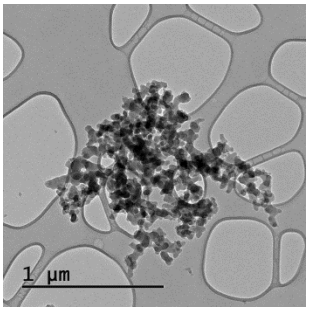

A8-26

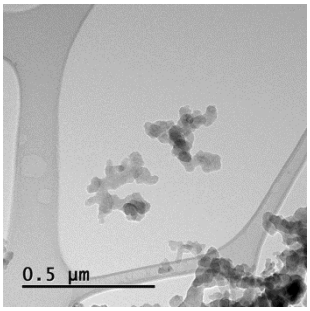

A8-27

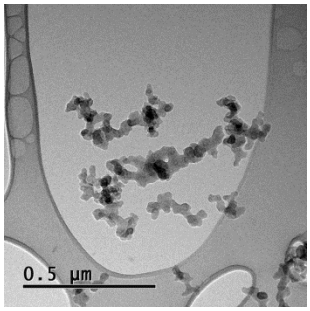

A8-28

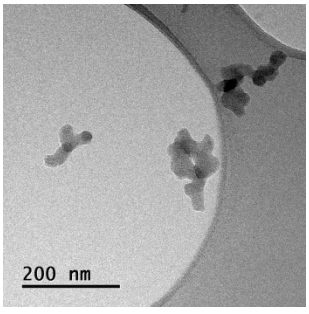

A8-29

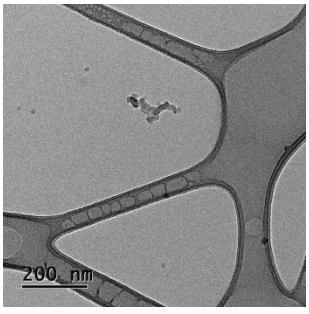

A8-30

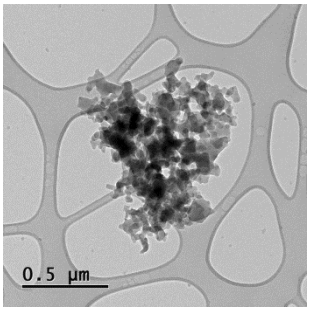

A8-31

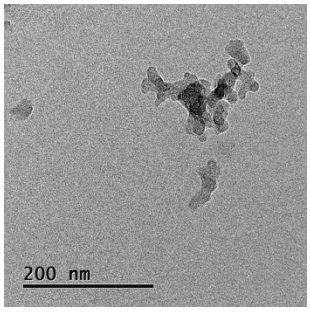

A8-32

Table B.18. TEM images of carbon particulates with 1.0 SLPM of decomposition methane and methane-air premixed flame (part 1).

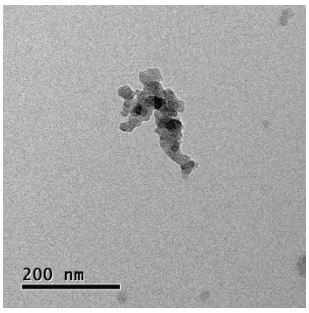

B8-1

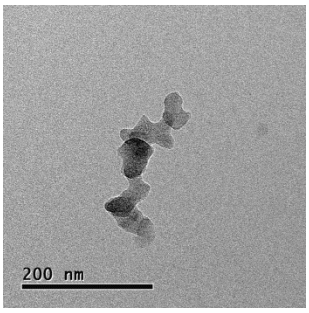

B8-2

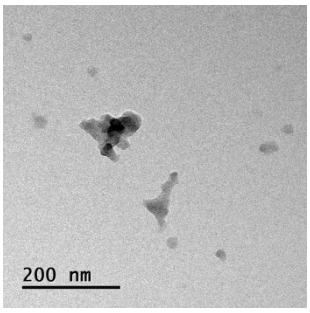

B8-3

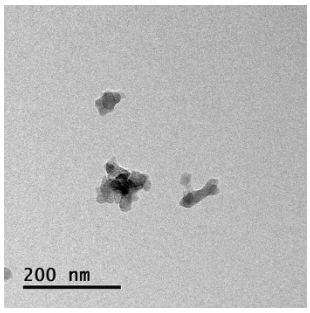

B8-4

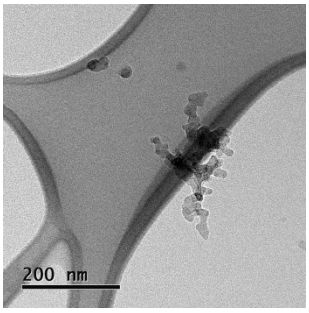

B8-5

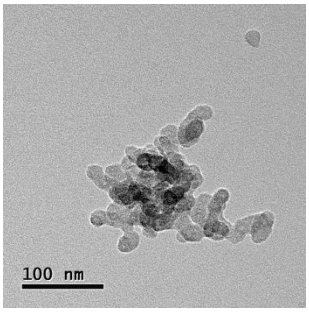

B8-6

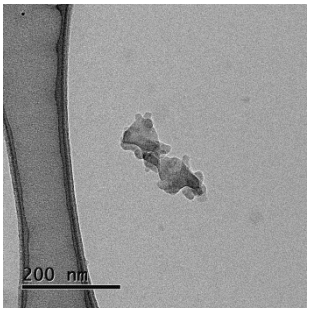

B8-7

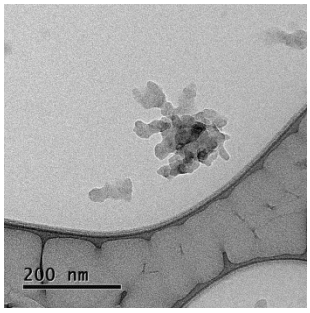

B8-8

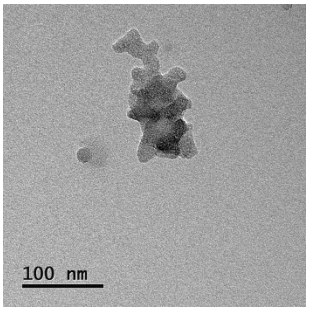

B8-9

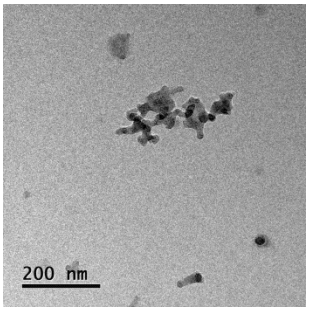

B8-10

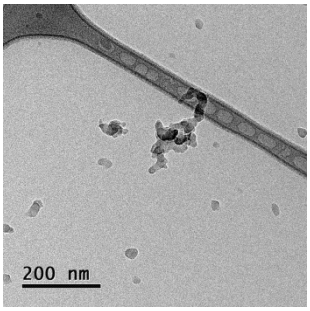

B8-11

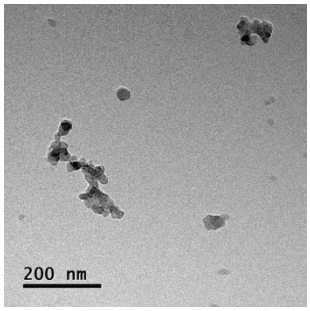

B8-12

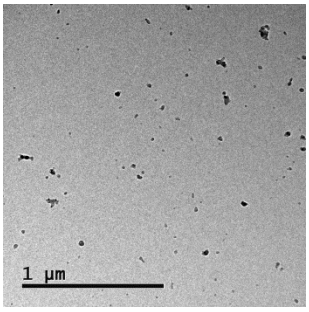

B8-13

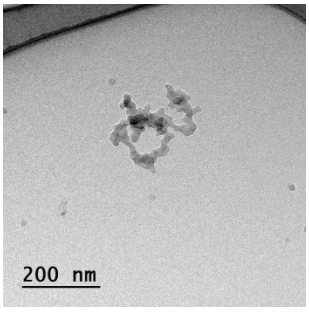

B8-14

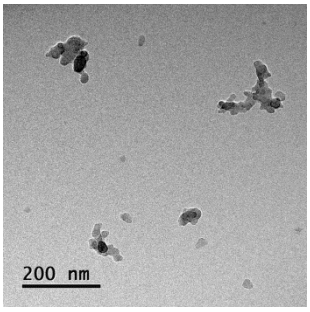

B8-15

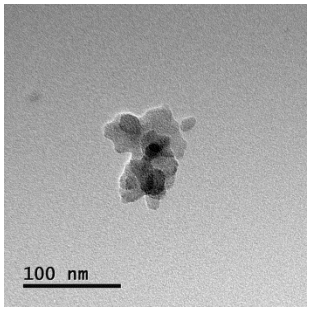

B8-16

Table B.19. TEM images of carbon particulates with 1.0 SLPM of decomposition methane and methane-air premixed flame (part 2).

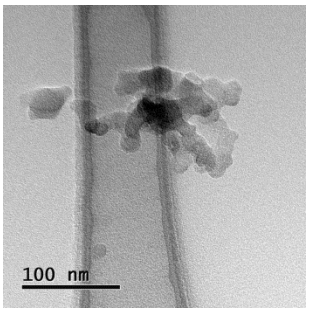

B8-17

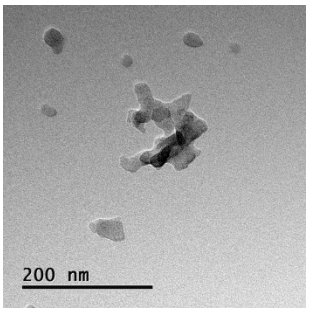

B8-18

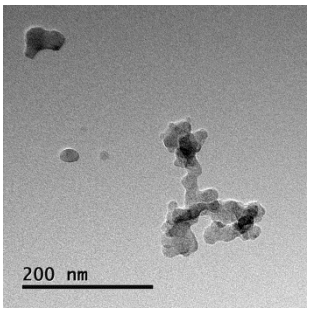

B8-19

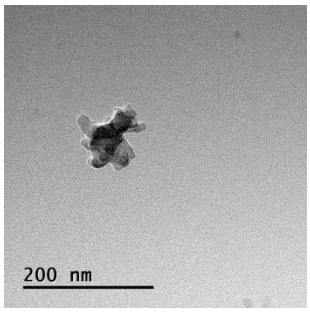

B8-20

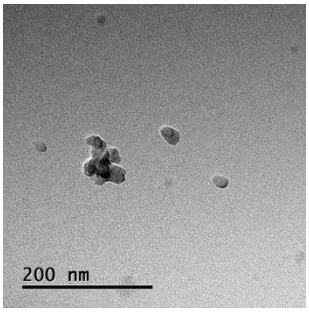

B8-21

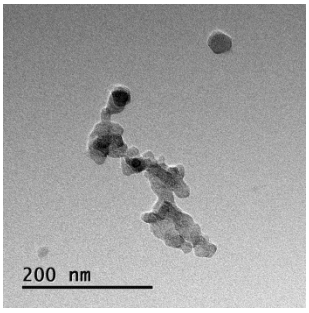

B8-22

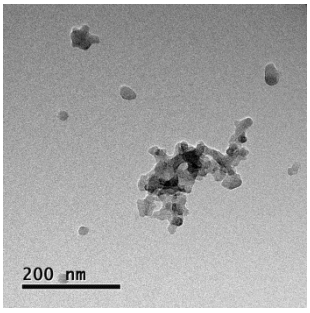

B8-23

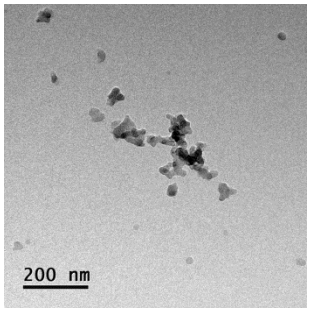

B8-24

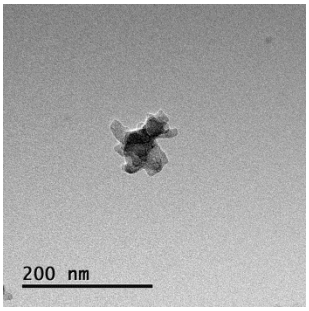

B8-25

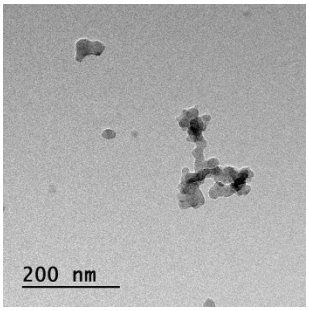

B8-26

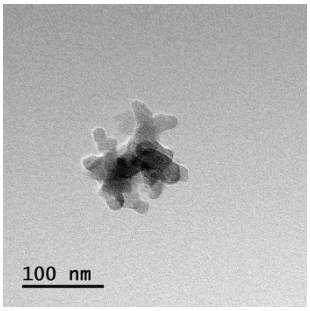

B8-27

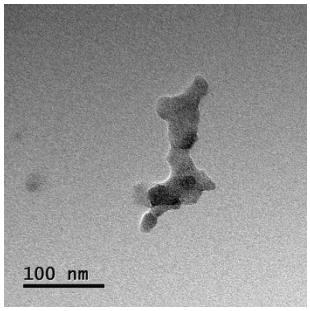

B8-28

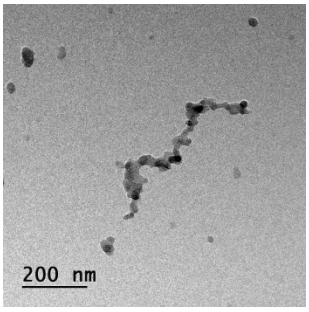

B8-29

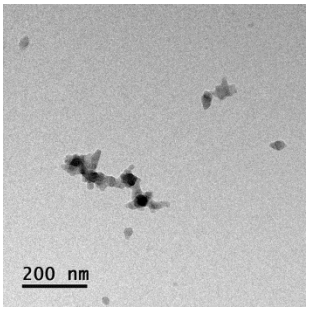

B8-30

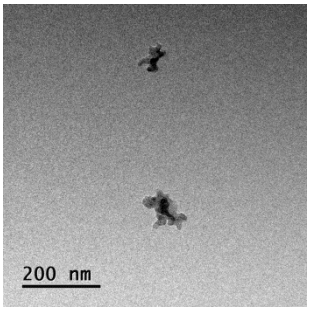

B8-31

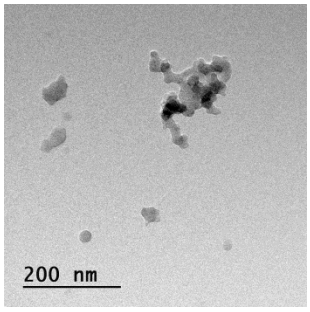

B8-32

Table B.20. TEM images of carbon particulates with 1.5 SLPM of decomposition methane and methane-air premixed flame (part 1).

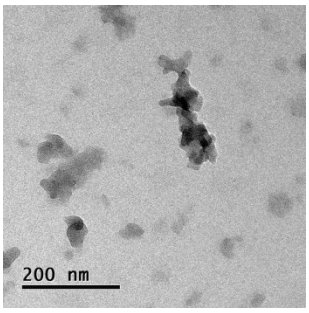

C8-1

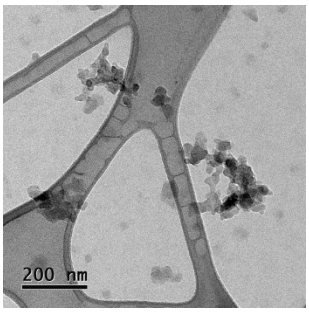

C8-2

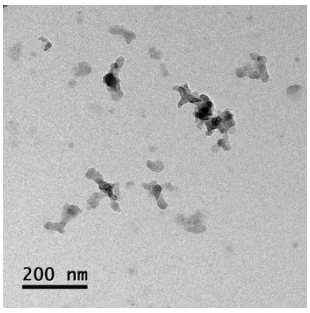

C8-3

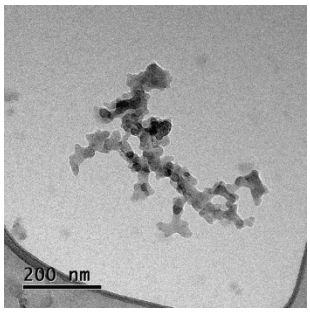

C8-4

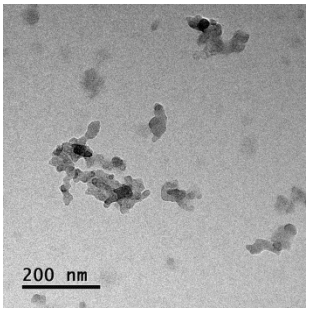

C8-5

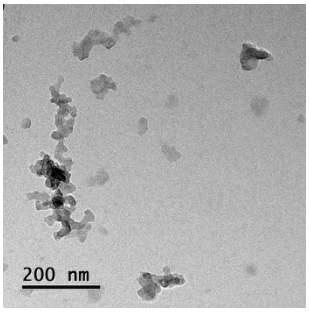

C8-6

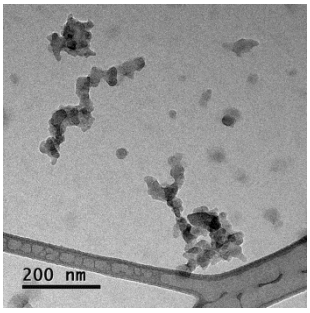

C8-7

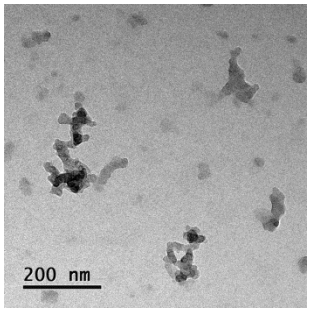

C8-8

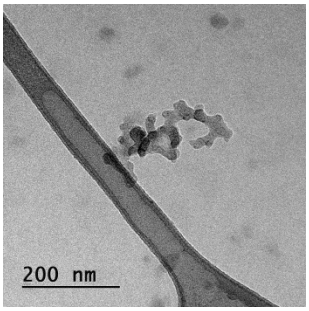

C8-9

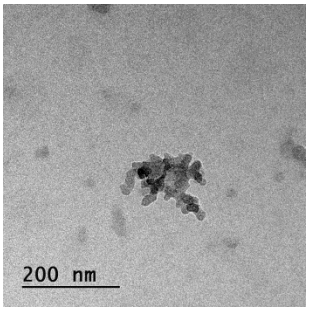

C8-10

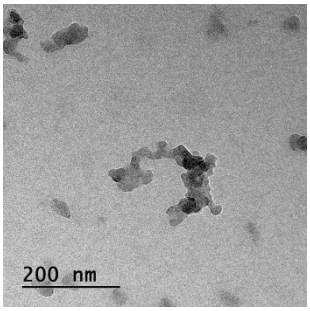

C8-11

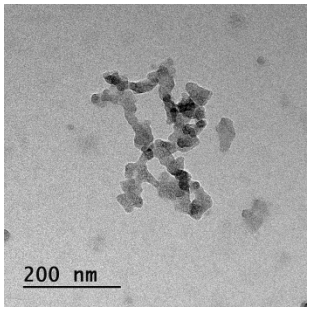

C8-12

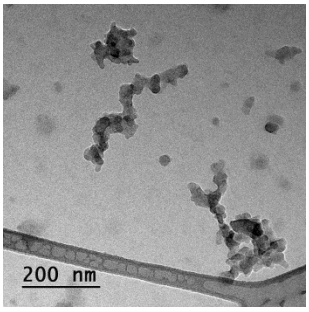

C8-13

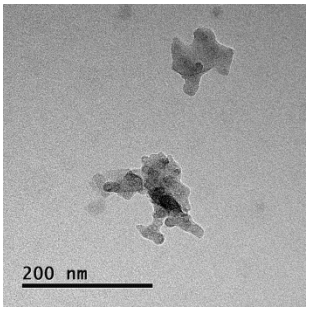

C8-14

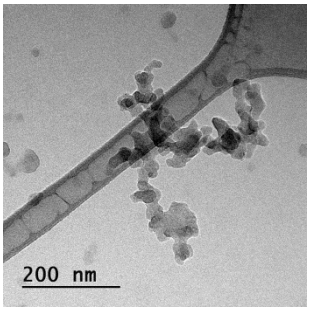

C8-15

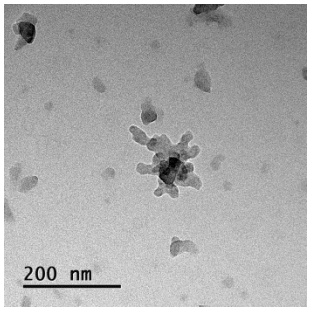

C8-16

Table B.21. TEM images of carbon particulates with 1.5 SLPM of decomposition methane and methane-air premixed flame (part 2).

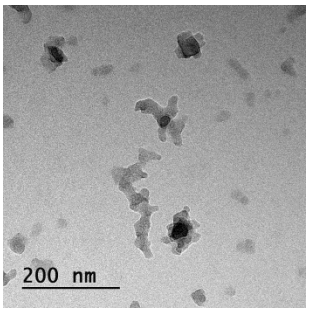

C8-17

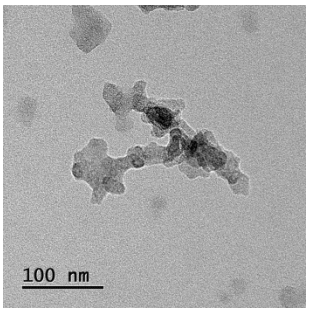

C8-18

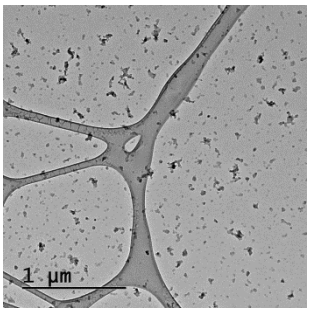

C8-19

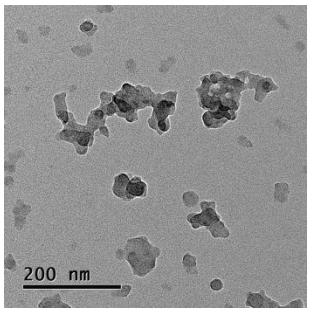

C8-20

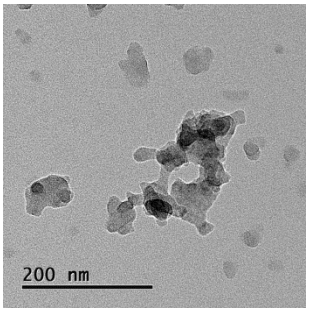

C8-21

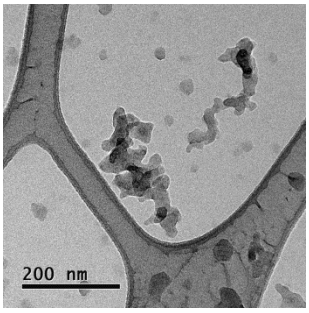

C8-22

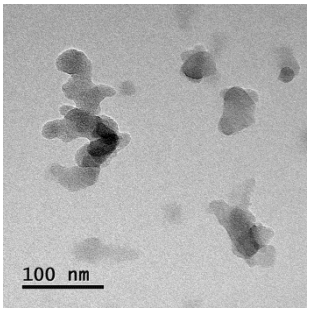

C8-23

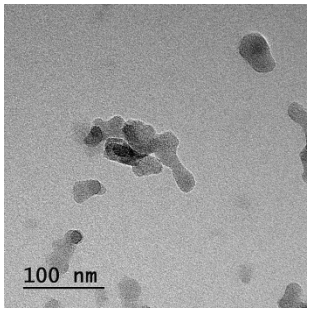

C8-24

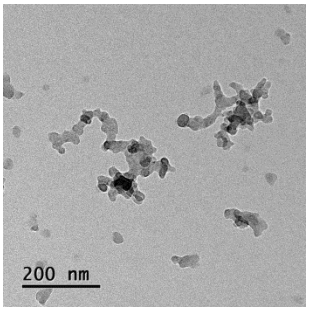

C8-25

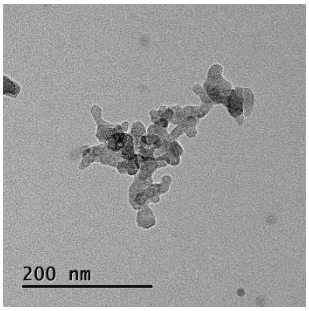

C8-26

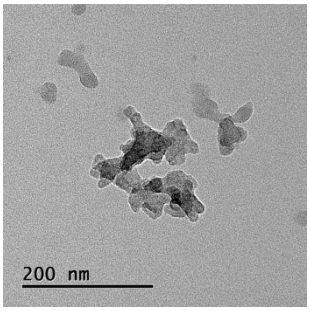

C8-27

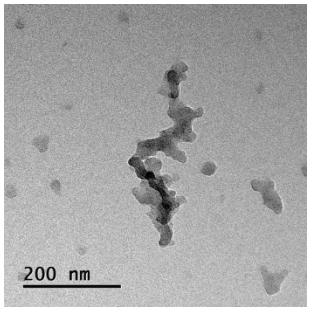

C8-28

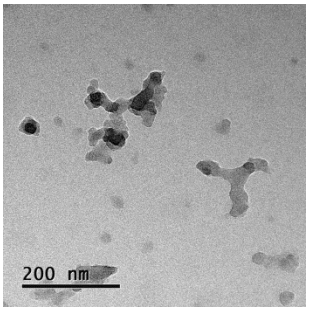

C8-29

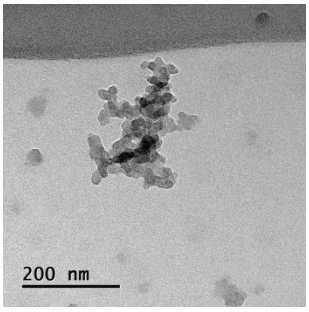

C8-30

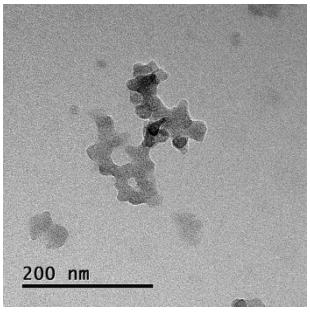

C8-31

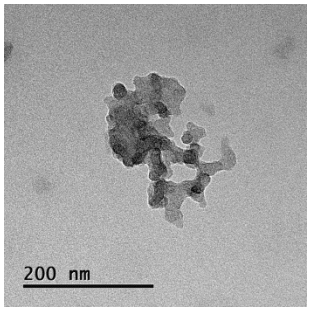

C8-32

Table B.22. TEM images of carbon particulates with 2.0 SLPM of decomposition methane and methane-air premixed flame (part 1).

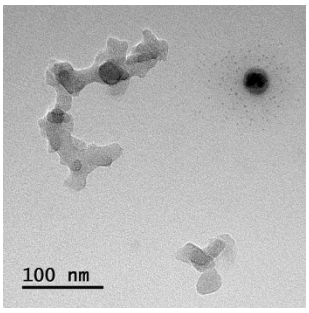

D8-1

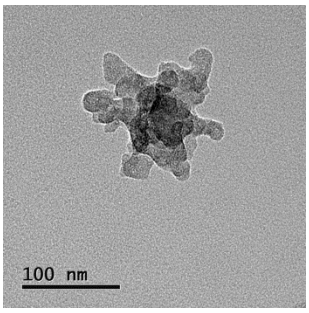

D8-2

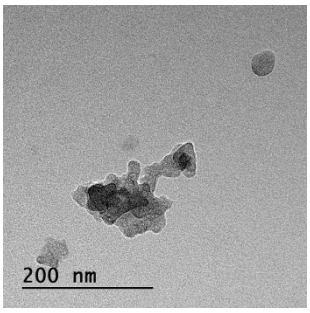

D8-3

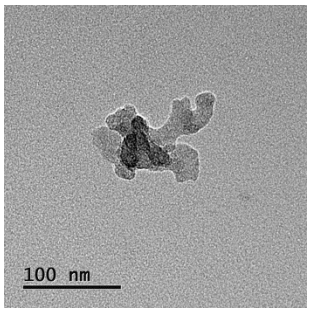

D8-4

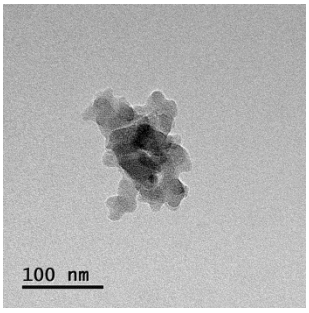

D8-5

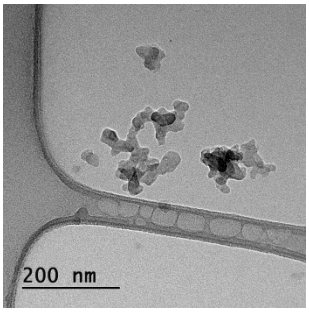

D8-6

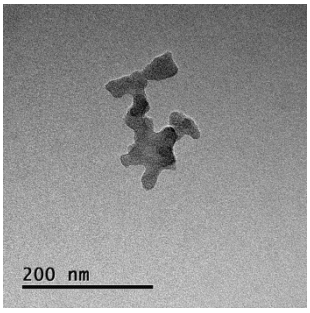

D8-7

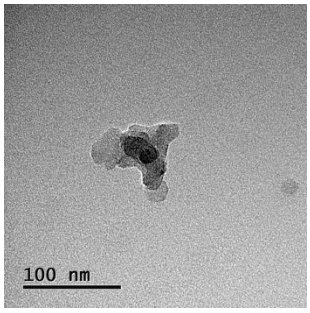

D8-8

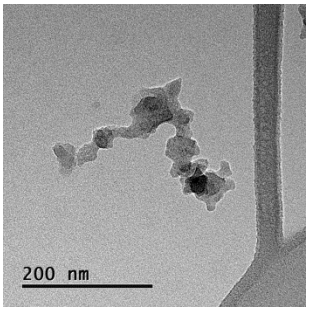

D8-9

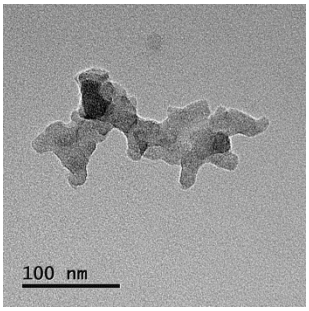

D8-10

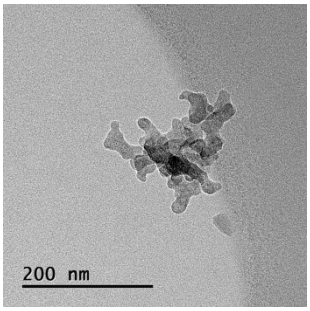

D8-11

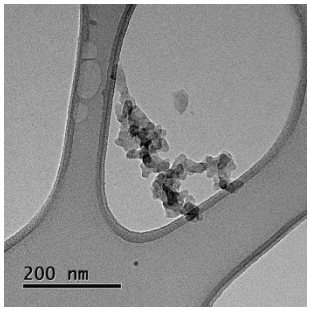

D8-12

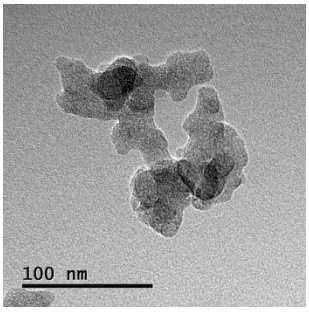

D8-13

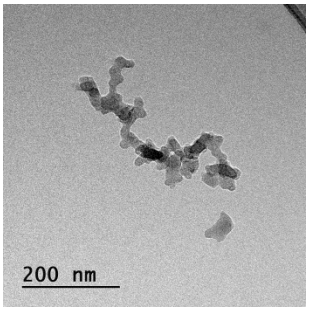

D8-14

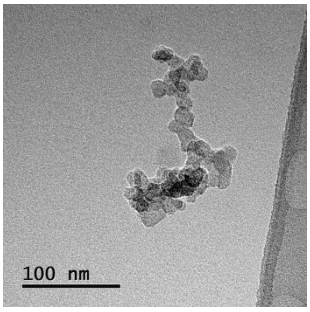

D8-15

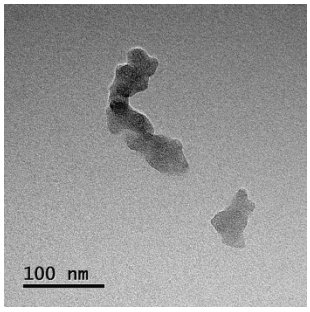

D8-16

Table B.23. TEM images of carbon particulates with 2.0 SLPM of decomposition methane and methane-air premixed flame (part 2).

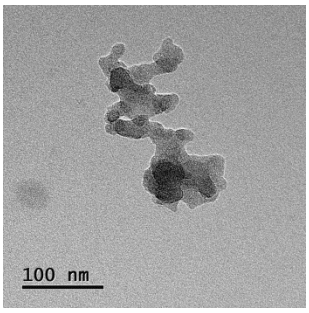

D8-17

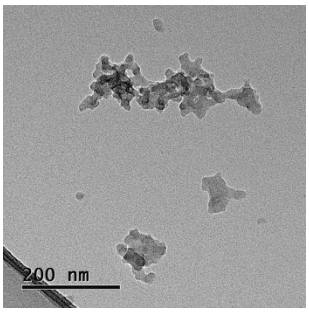

D8-18

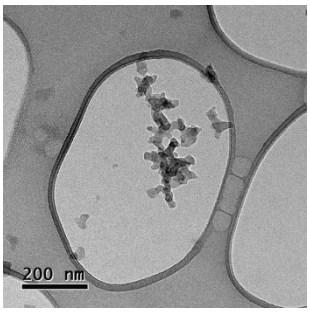

D8-19

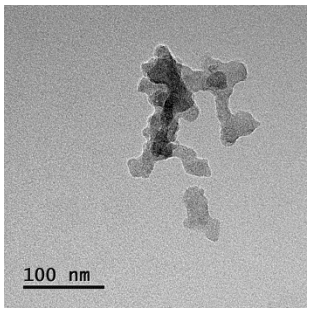

D8-20

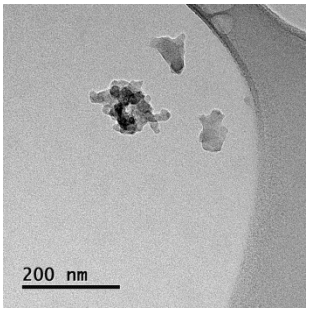

D8-21

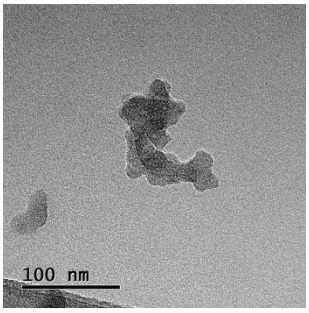

D8-22

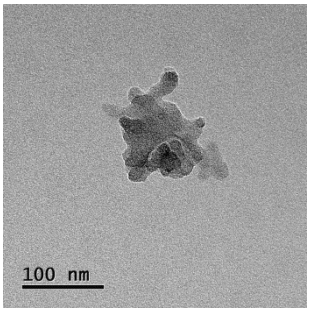

D8-23

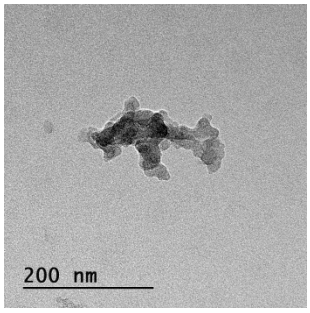

D8-24

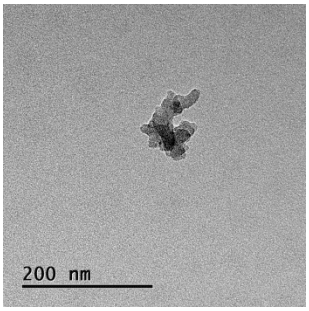

D8-25

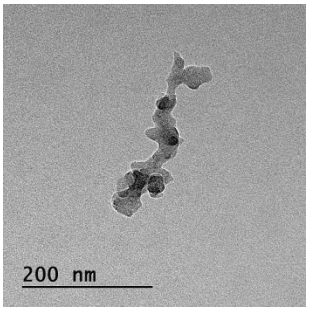

D8-26

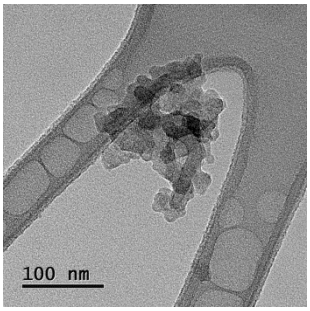

D8-27

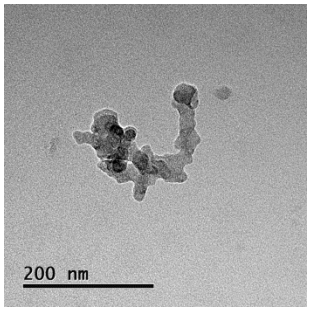

D8-28

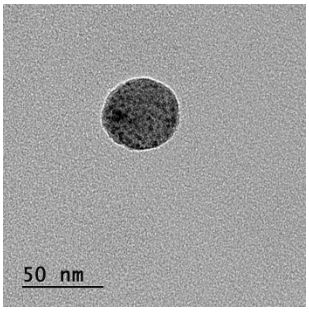

D8-29

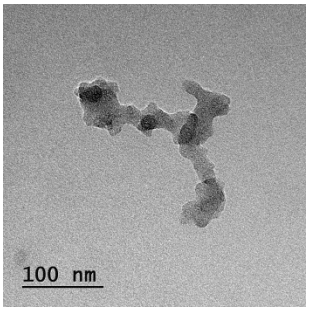

D8-30

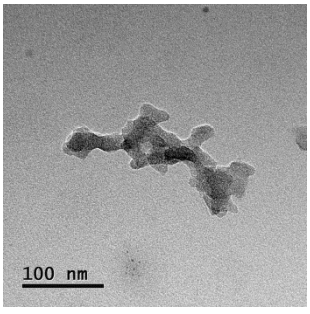

D8-31

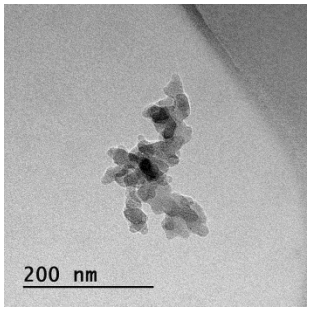

D8-32

Table B.24. TEM images of carbon particulates with 5.0 SLPM of decomposition methane and methane-air premixed flame (part 1).

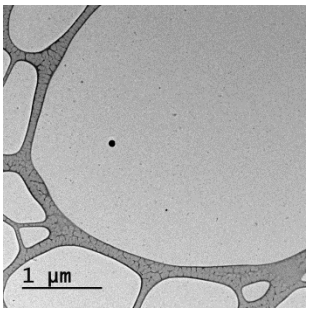

E8-1

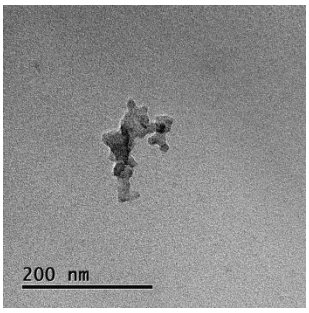

E8-2

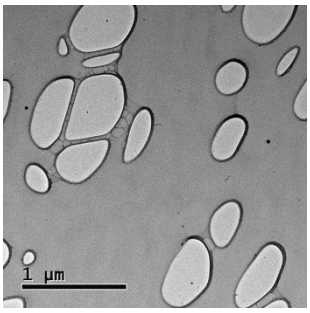

E8-3

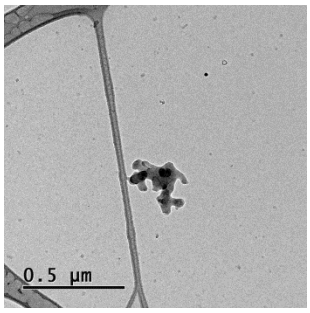

E8-4

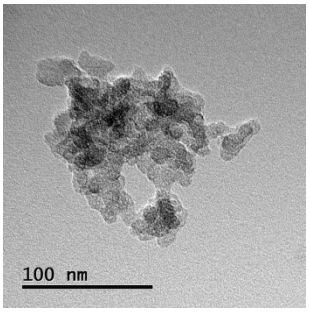

E8-5

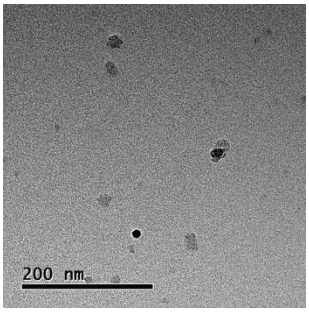

E8-6

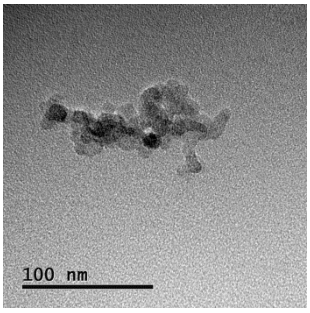

E8-7

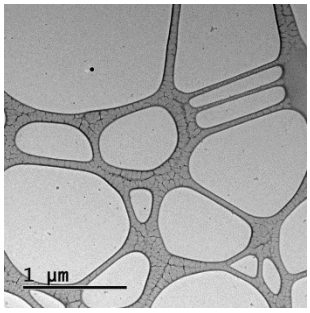

E8-8

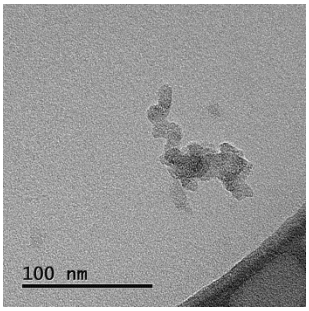

E8-9

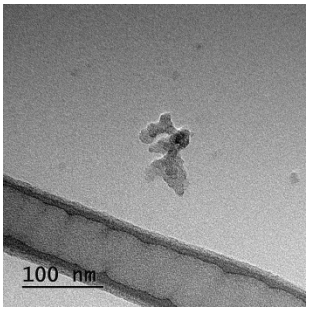

E8-10

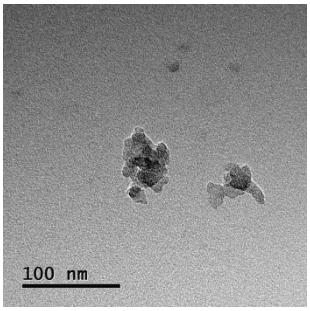

E8-11

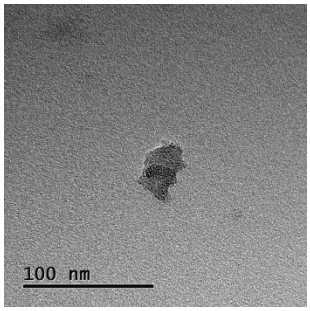

E8-12

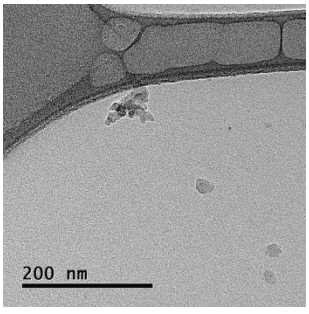

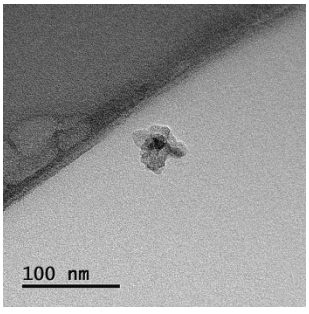

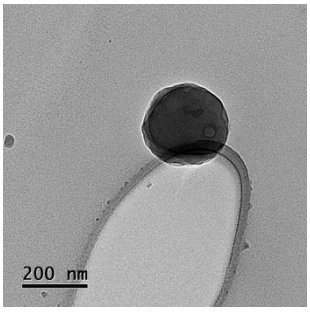

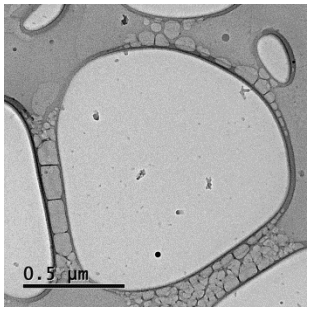

Appendix C Temperature Correction

The temperature read by the thermocouple in this study needs to be corrected to obtain the gas composition temperature of premixed flame. This was done through the energy balance for the thermocouple as Shaddix (1999) suggested:

$$\dot{Q}_{\mathrm{rad}} + \dot{Q}_{\mathrm{conv}} + \dot{Q}_{\mathrm{cond}} + \dot{Q}_{\mathrm{cat}} = \rho_{\mathrm{th}} c_{\mathrm{p,th}} V_{\mathrm{th}} \frac{\mathrm{d}T_{\mathrm{th}}}{\mathrm{d}t}, \tag{C.1}$$

where $\dot{Q}_{\mathrm{rad}}$ is the radiation heat transfer, $\dot{Q}_{\mathrm{conv}}$ is the convective heat transfer, $\dot{Q}_{\mathrm{cond}}$ is the conductive heat transfer, and $\dot{Q}_{\mathrm{cat}}$ is the heat transfer due to catalytic reactions. T_{th} is the thermocouple temperature, $c_{p,\mathrm{th}}$ is the specific heat of thermocouple, ρ_{th} and V_{th} are the density and volume of the thermocouple, respectively. Since the measurements were conducted in steady-state condition, the right-hand-side term of equation (C.1) is zero. The catalytic effects on the surface of thermocouple was neglected due to use of k-type thermocouple with nickel-chromium/nickel-alumel coating of which material could be considered non-reactive at the working temperature of this study (Kasper et al. 1999). The conductive heat transfer, $\dot{Q}_{\mathrm{cond}}$, was considered insignificant as the conduction heat loss from the junction and other hot parts of the thermocouple wire to cooler regions could be neglected when the length to diameter ratio of thermocouple is more than 200 (Heitor & Moreira 1993), which was the case in this study. Therefore, equation (C.1) becomes

$$\dot{Q}_{\mathrm{rad}} + \dot{Q}_{\mathrm{conv}} = 0. \tag{C.2}$$

The radiation heat transfer between the gray-emitting thermocouple surface and a much larger, isothermal enclosing diffusive gray surface (insulating blocks in this study) is independent of the wall (insulation) emissivity (Shaddix 1999) and is given by

$$\dot{Q}_{\mathrm{rad}} = \varepsilon_{th}\sigma A_{th}(T_{\mathrm{th}}^4 - T_{\mathrm{ins}}^4), \tag{C.3}$$

where ε_{th} is the emissivity of thermocouple, σ is the Stefan-Boltzmann constant, A_{th} is thermocouple surface area, and T_{ins} is the insulation temperature. Also, the convection term in equation (C.2) could be written as

$$\dot{Q}_{\mathrm{conv}} = -A_{th}h\big(T_{\mathrm{g}} - T_{\mathrm{th}}\big), \tag{C.4}$$

where h is the heat transfer coefficient, and T_{g} is the gas temperature (products of the premixed flame). Combining equations (C.2) to (C.4) and solving for gas temperature:

$$T_{\mathrm{g}} = T_{\mathrm{th}} + \frac{\varepsilon_{th}\sigma}{h}(T_{\mathrm{th}}^4 - T_{\mathrm{ins}}^4). \tag{C.5}$$

Rewriting Equation (C.5) based on the Nusselt number, the gas temperature was driven as

$$T_{\mathrm{g}} = T_{\mathrm{th}} + \varepsilon_{th}\sigma(T_{\mathrm{th}}^4 - T_{\mathrm{ins}}^4)\frac{d_{th}}{k\,Nu}, \tag{C.6}$$

where d_{th} is the thermocouple junction diameter and k is the thermal conductivity, and Nusselet number is defined as

$$Nu \equiv \frac{h\, d_{th}}{k}. \tag{C.7}$$

The most commonly used correlation for Nusselt number applicable to low-Re forced convection over a sphere (thermocouple junction in this study) when $0.71 < Pr < 380$ and $3.5 < Re < 76{,}000$ is that given by Whitaker (1972),

$$Nu = 2 + (0.4\, Re^{\frac{1}{2}} + 0.06\, Re^{\frac{2}{3}})\, Pr^{0.4}\, (\frac{\mu_{\mathrm{g}}}{\mu_{\mathrm{th}}})^{\frac{1}{4}}, \tag{C.8}$$

where Re is the Reynolds Number, Pr is the Prandtl number, and μ_g and μ_{th} are the viscosity of gas at the gas temperature and at the thermocouple junction temperature, respectively. Substituting equation (C.8) into equation (C.6), the gas temperature could be obtained based on thermocouple and insulation temperatures as

$$T_{\mathrm{g}} = T_{\mathrm{th}} + \frac{\varepsilon_{th}\sigma}{2+(0.4\, Re^{\frac{1}{2}}+0.06\, Re^{\frac{2}{3}})\, Pr^{0.4}\, (\frac{\mu_{\mathrm{g}}}{\mu_{\mathrm{th}}})^{\frac{1}{4}}} (T_{\mathrm{th}}^4 - T_{\mathrm{ins}}^4) \frac{d_{th}}{k}, \tag{C.9}$$

where thermocouple junction diameter, d_{th}, was measured 0.635 mm, and thermocouple emissivity, ε_{th}, was considered 0.1 based on the junction material. Thermal conductivity, Reynolds number, Prandtl number, and viscosity are a function of gas composition, temperature and pressure. Assuming the steady-state pressure of reaction chamber was 1.05 atm ($1 < P < 1.1$ atm), those quantities could be defined for the specific gas composition of premixed flame products at the gas temperature, T_{g}, which is unknown.

The propane- or methane-air premixed flame are assumed to have the following reaction (with an equivalence ratio of 1.05):

$$n_1 C_x H_y(\text{fuel}) + n_2(O_2 + 3.76N_2) \rightarrow n_3 CO_2 + n_4 CO + n_5 H_2O + n_6 N_2 + n_7 HC + n_8 H_2 + n_9 O_2, \quad \text{(C.10)}$$

where C_xH_y is either methane or propane depending on which fuel was used for combustion, and CH_4, C_2H_6 and C_3H_8 are unburnt hydrocarbons (HC) observed by the GC in the products, while n_i are coefficients determined either by inflow mass flow controllers or GC measurements of the products. Similar to Chapter 2, by assuming $\dot{n}_{N_2,in} = \dot{n}_{N_2,out}$, the total molar rate of gaseous components (excluding water vapor) could be obtained based on the molar flow rate of N_2 in the inlet ($\dot{n}_{N_2,in}$):

$$\dot{n}_{total,out} = \frac{\dot{n}_{N_2,out}}{y_{N_2,GC}} = \frac{\dot{n}_{N_2,in}}{y_{N_2,GC}} = \frac{0.78\,\dot{n}_{air,in}}{y_{N_2,GC}} = \frac{0.78}{y_{N_2,GC}}\left(\frac{\dot{V}_{air,in}\,\rho_{air}}{\mathcal{M}_{air}}\right), \quad \text{(C.11)}$$

where 0.78 is the mole fraction of N_2 (O_2 at 21% and Ar at 1%), $y_{N_2,GC}$ is the mole fraction of N_2 in the products measured by the GC, $\dot{V}_{air,in}$ is the standard flow rate of air mixed with the fuel and set by a mass flow controller (35 SLPM for propane-air and 34.8 for methane-air premixed flame), ρ_{air} is the density of air at standard conditions, and $\mathcal{M}_{air}$ is the molar mass of air. $\dot{n}_{total,out}$ later was used for finding molar rate of gaseous products (except water vapor) in the exhaust:

$$\dot{n}_{i,out} = y_{i,GC}\,\dot{n}_{total,out}, \quad \text{(C.12)}$$

where $y_{i,GC}$ is the molar fraction of gas *i* measured by the GC. The molar rate of fuel in the inlet could be obtained based on the following equation and used for calculating the water vapor molar rate through balancing the hydrogen atom molar rates in the inlet and outlet:

$$\dot{n}_{\text{fuel,in}} = \frac{\dot{V}_{\text{fuel,in}}\,\rho_{\text{fuel}}}{\mathcal{M}_{\text{fuel}}}, \tag{C.13}$$

where $\dot{V}_{\text{fuel,in}}$ is the standard flow rate of fuel and set by a mass flow controller (1.43 SLPM for propane and 1.62 SLPM for methane as fuel), ρ_{fuel} is the density of fuel at standard conditions, and $\mathcal{M}_{\text{fuel}}$ is the molar mass of fuel. Based on the calculated molar rates, the molar fraction of propane-air or methane-air premixed flame products were obtained:

Table C.1. Molar fraction of propane-air or methane-air premixed flame products under the equivalence ratio of 1.05.

	Products Molar fraction								
Fuel	CH_4	C_2H_6	C_3H_8	CO_2	O_2	N_2	CO	H_2	$H_2O_{(g)}$
Propane	0	0	0	0.112	0.012	0.714	0.010	0.007	0.145
Methane	0	0	0	0.103	0.012	0.783	0.009	0.008	0.085

Having the product gas composition, thermal conductivity, Reynolds number, Prandtl number, and viscosity could be found for the reactor pressure of 1.05 atm and the product gas temperature. Also, gas viscosity at the thermocouple temperature, μ_{th}, could be obtained for premixed flame products using CHEMKIN software. μ_{th} was $5.29 \times 10^{-5}\ \frac{\text{kg}}{\text{m s}}$ for propane-air premixed flame at 1170 ℃, and $5.19 \times 10^{-5}\ \frac{\text{kg}}{\text{m s}}$ for methane-air premixed flame at 1130 ℃.

Reynolds number associated with premixed flame products in this study is similar to Reynolds number in a pipe because of similar geometries (see Figure C.1). Thus, Reynolds number could be defined as

$$Re = \frac{\rho_g \, u_g \, D_h}{\mu_g}, \tag{C.14}$$

where D_h is hydraulic diameter and equal to 26.9 mm, ρ_g and u_g are density and velocity of product gas composition, respectively.

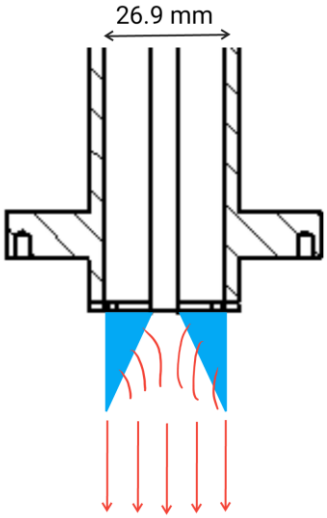

Figure C.1. Flow of product gas composition from the premixed flame.

Based on continuity of mass:

$$\rho_g \, u_g = \rho_{mixture} \, u_{mixture}, \tag{C.15}$$

where $\rho_{mixture}$ and $u_{mixture}$ are the density and velocity of unburnt fuel-air mixture at standard condition (0 ℃ and 1 atm), respectively, and were defined based on the following equations:

$$\rho_{mixture} = \frac{\dot{V}_{fuel,in} \, \rho_{fuel} + \dot{V}_{air,in} \, \rho_{air}}{\dot{V}_{fuel,in} + \dot{V}_{air,in}}, \tag{C.16}$$

$$u_{\text{mixture}} = \frac{\dot{V}_{\text{fuel,in}} + \dot{V}_{\text{air,in}}}{A_{burner}}. \quad \text{(C.17)}$$

Combining equations (C.14) and (C.15), Reynolds number could be rewritten as

$$Re = \frac{\rho_{\text{mixture}}\, u_{\text{mixture}}\, D_{\text{h}}}{\mu_{\text{g}}}, \quad \text{(C.18)}$$

where viscosity of product gas composition is dependent to the gas temperature. *Re* for product gas composition of propane-air premixed flame was simplified as

$$Re_{\text{p}} = \frac{0.011}{\mu_{\text{g,p}}}, \quad \text{(C.19)}$$

and for methane-air premixed flame was recalculated as

$$Re_{\text{m}} = \frac{0.017}{\mu_{\text{g,m}}}. \quad \text{(C.20)}$$

Furthermore, Prandtl number is defined as

$$Pr = \frac{\nu_{\text{g}}}{\alpha_{\text{g}}}, \quad \text{(C.20)}$$

where ν_{g} and α_{g} are kinematic viscosity and thermal diffusivity of product gas composition, respectively, and are a function of gas temperature.

Looking back at equation (C.9), gas temperature, T_{g}, could be obtained based on the insulation temperature, T_{ins}, and other properties of product gas flow, such as *Re*, *Pr, k,* and μ_{g}. These properties are a function of T_{g} and could be defined by CHEMKIN software for the specific gas composition at the chamber pressure. As such, for each insulation temperature of

T_{ins}, gas temperature was calculated through trial and error iterations. The results of this process are presented in Figure C.2.

As shown in Figure C.2, the radiation correction for product gas temperature only accounts for 17 ℃ for propane-air and 13 ℃ for methane-air premixed flame at the lowest temperature of insulation. Therefore, it could be concluded that thermocouple measurements of gas temperature were sufficiently accurate in this study.

(a)

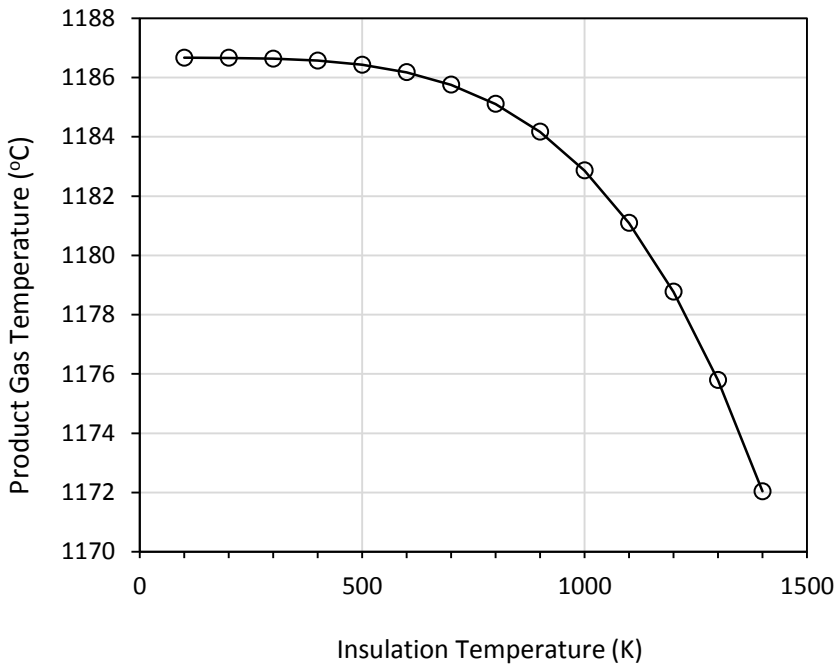

(b)

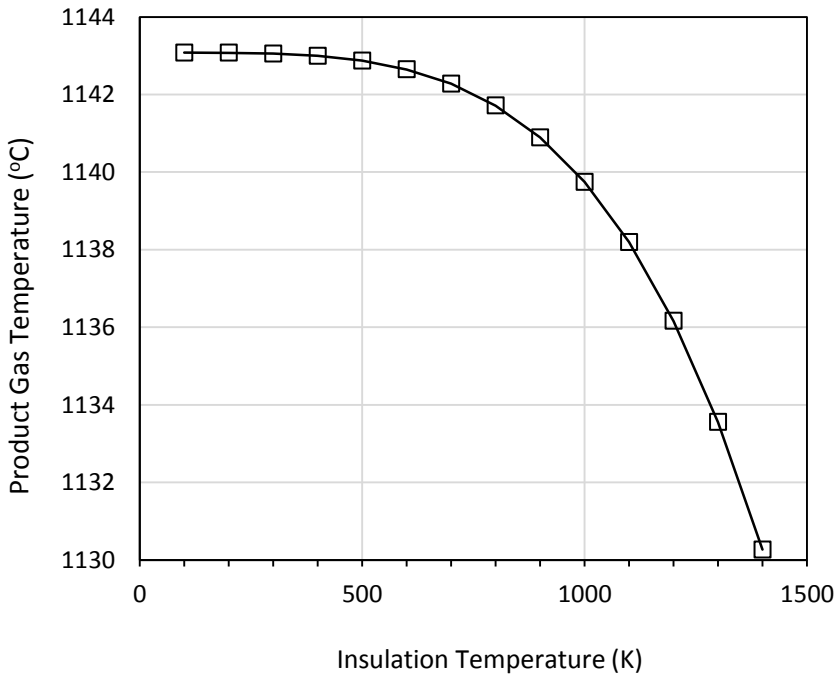

Figure C.2. Corrected product gas temperature as a function of insulation temperature for (a) propane-air and (b) methane-air premixed flame. Gas temperature measured by thermocouple was 1170 ℃ and 1130 ℃ at the tip of propane-air and methane-air premixed flame, respectively.